Alma Mater Studiorum · Università di Bologna

Scuola di Scienze
Corso di Laurea Magistrale in Fisica

An fMRI study of brain functional connectivity in Parkinson's disease patients

Relatore:
Dott.ssa Claudia Testa

Presentata da:
Stefania Evangelisti

Sessione II
Anno Accademico 2012/2013

Abstract

Argomento del presente lavoro è l'analisi di dati fMRI (functional Magnetic Resonance Imaging) nell'ambito di uno studio EEG-fMRI su pazienti affetti da malattia di Parkinson idiopatica.

L'EEG-fMRI combina due diverse tecniche per lo studio *in vivo* dell'attività cerebrale: l'elettroencefalografia (EEG) e la risonanza magnetica funzionale. La prima registra l'attività elettrica dei neuroni corticali con ottima risoluzione temporale; la seconda misura indirettamente l'attività neuronale registrando gli effetti metabolici ad essa correlati, con buona risoluzione spaziale. L'acquisizione simultanea e la combinazione dei due tipi di dati permettono di sfruttare i vantaggi di ciascuna tecnica.

Scopo dello studio è l'indagine della connettività funzionale cerebrale in condizioni di riposo in pazienti con malattia di Parkinson idiopatica ad uno stadio precoce. In particolare, l'interesse è focalizzato sulle variazioni della connettività con aree motorie primarie e supplementari in seguito alla somministrazione della terapia dopaminergica.

Le quattro fasi principali dell'analisi dei dati sono la correzione del rumore fisiologico, il pre-processing usuale dei dati fMRI, l'analisi di connettività "seed-based " e la combinazione dei dati relativi ad ogni paziente in un'analisi statistica di gruppo. Usando l'elettrocardiogramma misurato contestualmente all'EEG ed una stima dell'attività respiratoria, è stata effettuata la correzione del rumore fisiologico, ottenendo risultati consistenti con la letteratura. L'analisi di connettività fMRI ha mostrato un aumento significativo della connettività dopo la somministrazione della terapia: in particolare, si è riscontrato che le aree cerebrali maggiormente connesse alle aree motorie sono quelle coinvolte nel network sensorimotorio, nel network attentivo e nel default mode network. Questi risultati suggeriscono che la terapia dopaminergica, oltre ad avere un effetto positivo sulle performance motorie durante l'esecuzione del movimento, inizia ad agire anche in condizioni di riposo, migliorando le funzioni attentive ed esecutive, componenti integranti della fase preparatoria del movimento.

Nel prossimo futuro questi risultati verranno combinati con quelli ottenuti dall'analisi dei dati EEG.

Contents

Introduction

Parkinson's disease (PD) is a neurodegenerative disorder that occurs when neurons located in a specific brain area (called substantia nigra) die or become impaired. This area has a key role in brain function, especially as far as the release of dopamine, an important neurotransmitter, is concerned. This neurotransmitter is mainly involved in the control of movements and coordination, and also in information processing, therefore its loss negatively affects these functions. Therapies for Parkinson's disease are just symptomatic and the principal drug therapies are dopaminergic therapies (such as Levodopa, or L-dopa), that mimic dopamine to stimulate the dopamine system in the brain.

When symptoms of PD appear, there are relatively limited changes in brain structure, while there are substantial effects on functional brain circuitry, therefore techniques that provide information about functional brain organization may give further insights into the pathophysiology of the disorder. The human brain is organized into interacting systems that, according to various brain functions, are made of different brain areas that can be defined as connected. The operative definition of functional connectivity is of temporally-correlated remote neurophysiological events.

Different techniques exist to measure functional connectivity, that are invasive to a grater or lesser extent and have different temporal and spatial resolutions. Recently, the combination of two of these has become a key method in neuroscientific research. One is the electroencephalography (EEG), a non-invasive *in vivo* electrophysiological technique that measures electrical activity of neurons in the brain cortex with great temporal resolution but relatively poor spatial resolution. The other is fMRI (functional Magnetic Resonance Imaging), a non-invasive *in vivo* imaging technique that provides an indirect measure of brain activity, by measuring physiological metabolic changes linked to brain activation. It allows the mapping of neuronal activation deep in the brain, but temporal resolution is quite limited. Their simultaneous acquisition, known as EEG-fMRI, leads to combine EEG high temporal resolution with fMRI spatial resolution and information from the whole brain, and provides in addition information about the link between electrical activity and metabolic changes. Anyhow, combining them has not been straightforward, due to electromagnetic interactions that create potential hazard for patient's safety and various artefacts in the acquired data. The first application of EEG-fMRI was in studying epilepsy, as it can provide reliable information for the localization of the regions that generate interictal epileptiform activity: in EEG electrical spikes are visible, while fMRI shows brain areas that are more active when the spikes occurred.

The present study adopts a novel approach, as EEG-fMRI is used to investigate brain functional connectivity in PD patients. The study has been developed thanks to the collaboration of the IRCSS (Istituto delle Scienze Neurologiche di Bologna) and the U.O. RM funzionale, DIBINEM (Dipartimento di Scienze Biomediche e Neuromotorie). Its goal is to study possible variations in brain functional connectivity with motor areas related to dopaminergic therapies in early-stage PD patients, both in fMRI and EEG data. Brain connections with the primary motor area and the supplementary motor area are compared before and after the intake of L-dopa.

Specifically, the present thesis work deals with the analysis of fMRI data, as pre-processing and statistical analysis are necessary in order to identify small changes in images intensity in the corresponding areas of brain activation. The first pre-processing step deals with the removal of signal fluctuations that physiological processes, such as cardiac pulsation and respiration, can cause in fMRI measurements. A robust method of regression is applied, using the electrocardiogram measured with the EEG and an estimate of respiratory activity. Then the other usual fMRI pre-processing steps are applied, namely slice timing correction, motion correction, spatial and temporal filtering. For the connectivity analysis, a seed-based method is used: four seeds are drawn in specific areas of interest (right and left precentral gyrus, right and left supplementary motor area), the average time-course inside these regions is extracted, and then used to compute correlation with the time-courses from all the brain voxels. For the statistical analysis of each subject data, the model-based, univariate approach of General Linear Model is used. Finally, to combine the different subjects' data, the brain images are registered to a common space, and the group statistic is estimated with a mixed-effects clustering analysis.

This thesis is organized as follows. The first chapter goes into fMRI, describing brain metabolism, what is measured with fMRI, how fMRI data are generally analysed and resting state fMRI that, in particular, allows functional connectivity to be measured. The second chapter reports a brief outline of main EEG principles (physiology and measurement), together with a description of the essential issues arising from the combination of EEG and fMRI. The third chapter briefly describes Parkinson's disease and how functional connectivity may be related to PD. The materials and the methods we specifically used are described in the fourth chapter, while the fifth shows the results of our analysis. Finally, our conclusions and future research developments are outlined in the sixth chapter.

Chapter 1

Functional Magnetic Resonance Imaging

fMRI provides an indirect measure of brain activity: it doesn't measure directly the neural-electric activity, but consequences of this activity in the energy metabolism of the brain; more precisely it is related to the level of oxygenation within the corresponding vasculature ([1], [2]). Brain activation is known to lead to enhanced perfusion which together with other physiological changes (blood volume, oxygen consumption) results in a decreased deoxyhaemoglobin concentration in regions of neuronal activity. This effect is referred to as BOLD (Blood Oxygen Level Dependant) effect, that is by far the most commonly used method for fMRI studies and manifests itself as a slight increase in the T_2^* (or T_2) weighted MR images used for fMRI studies. Usually fMRI acquisition are performed while the subject undergoes an alternation of task and rest periods, to activate specific areas of the brain, or while particular isolated events take place. In the last decade also fMRI resting state has been developed and finds its application in mapping human brain functional connectivity. A rich statistical analysis is necessary on fMRI data in order to identify small changes in images intensity in the areas corresponding to brain activated areas.

fMRI is a non-invasive technique and thus safe for use across all age groups; it is potentially the most powerful tool available today for studying the neural underpinnings of the vast cognitive and social developments that occurs in humans.

For detailed information about basic principles of nuclear magnetic resonance and magnetic resonance imaging, we refer you to books [3] and [4].

1.1 Principles of fMRI

1.1.1 Brain energy metabolism

BOLD signal changes depend on physiological changes (local changes in oxygen consumption and blood supply) accompanying brain activation.

Under normal conditions the brain derives almost all of its energy from the oxidation of glucose, that's why it is nearly under constant supply of glucose and oxygen, delivered by the blood supply through a rich network of vessels. The vascular system that supplies blood to the brain is organized on spatial scales that span a size range of four orders of magnitude, from the diameter of a capillary (about 10μ) to the size of a distribution volume of a major artery (about $10cm^3$), [2]. Although the brain accounts for only about 2% of the total body mass, it consumes 20% of the total body's glucose and oxygen, and receives 20% of its blood supply.

A remarkable feature of brain metabolism is that blood flow and energy metabolism are tightly linked to local neuronal activity, therefore maps of local glucose consumption, local oxygen consumption or local blood flow may provide information on neuronal activity. The general principles of brain metabolism and of the haemodynamic response to neuronal activity are known, but the precise mechanism responsible for the links between brain energy metabolism and brain work are not well defined yet.

In 1890 the physiologist Charles Sherrington demonstrated that stimulation of the brain caused a local increase in blood flow. He also observed that the relative proportion of oxygen extracted from this blood was reduced: the increase in total oxygen delivery exceeded the increase in oxygen utilization and this has the potential physiological significance that rates of oxygen diffusion from capillaries may limit its utilization rate. By increasing the relative proportion of oxygenated haemoglobin in blood, the oxygen gradient between capillaries and cell mitochondria is increased, helping to match diffusion-limited transport to the rate of utilization. Accompanying the increase in blood flow is a small increase in local blood volume. Locally increased blood flow in regions of the brain that become active appears to be a consequence of increased energy utilization at the synapses, [1].

In the brain, energy is used primarily for electrochemical work. Major work of the brain is the transfer and processing of information and there are two ways in which information are transferred: propagation of an altered membrane potential and through the release of chemical neurotransmitters.

Increased neural activity requires energy: pumping out from neurons ions which enter to generate synaptic, or action, potentials and metabolic changes in neurones and glia that accompany neurotransmitter release are energy-requiring, and most of this energy is used at or around synapses, [5]. Neural activity is therefore accompanied by ATP (Adenosine Tri-Phosphate) expenditure and by a consequently increased ATP production via glucose consumption (combination of glucose and oxygen are necessary to produce ATP through glycolysis and transcarboxylic acid cycle). Normal brain energy production depends ultimately on oxidative metabolism, therefore there is greater local demand for delivery of oxygen with increased synaptic activity. To meet this increased metabolic demand, neuronal activation is accompanied by increased local blood flow.

The haemodynamic response (HR) in the context of neurobiology consists of the rapid delivery of oxygen, through blood, to active neuronal tissues. Various cell types play a role in HR, including astrocytes (a sub-type of glial cells in the central nervous system, their many processes envelope synapses made by neurons) smooth muscle cells, endothelial cells of blood vessels and pericytes. These cells control whether the vessels are constricted or dilated, which dictates the amount of oxygen and glucose that is able to reach the neuronal tissue. Indeed the supply of oxygen and glucose to neurons mainly occurs across the walls of capillaries in the brain parenchyma (but with some oxygen passing across arteriolar walls). The amount of blood flow providing these nutrients is determined by the contractile tone of smooth muscle cells around pre-capillary arterioles, which controls the diameter of the vessels and hence the resistance to blood flow. Neurovascular coupling is supposed to occur via neuronal nitric oxide (NO) and via astrocytes: the release of neurotransmitters from active neurons generates neuron- and astrocyte- derived messengers which either modulate ion channel activity in the smooth muscle, leading to a change of intracellular calcium concentration ([Ca2+]), or change the calcium-sensitivity of the contractile apparatus, both of which lead to altered contraction. The exact signalling mechanism remains an area of intense research. Also relevant (as yet undetermined) are the contributions of neuronal versus astrocyte signalling, the contributions of excitatory versus inhibitatory neurotransmission, and the spatial extent and dynamic properties of neural versus vascular responses. More work needs to be done to clarify the interpretation and mechanism of coupling the haemodynamic response to neuronal activity.

BOLD signal changes depends on the combined changes in CBF (Cerebral Blood Flow), CMRO$_2$ (Cerebral Metabolic Rate of Oxygen) and CBV (Cerebral Blood Volume); this complicates the interpretation of BOLD signal in terms of physiological variables. There are also changes in the local oxygen concentration which initially falls due to consumption, and then rises above its baseline value when the increased blood flow brings in more oxygen and, concomitantly, there are changes in the levels of oxygenated and deoxygenated haemoglobin. The different magnetic properties of these molecules provide the basis of the BOLD signal (see 1.1.2.1). A focal increase in CBF can be considered to directly relate to neuronal activity because glucose metabolism and CBF changes are closely coupled. However, based on the positron emission tomographic measurements of CBF and (CMRO$_2$) utilization in humans during somatosensory and visual stimulation, the increase in CBF surpasses the increase in CMRO$_2$ resulting in an increase in capillary and venous oxygenation levels. Regardless of the exact signalling mechanisms for this CBF response, the BOLD signal is related to a mismatch between CBF increase and $CMRO_2$ change, as this imbalance results in a drop in oxygen extraction and a corresponding drop in the deoxyhemoglobin content of the venous blood, [6].

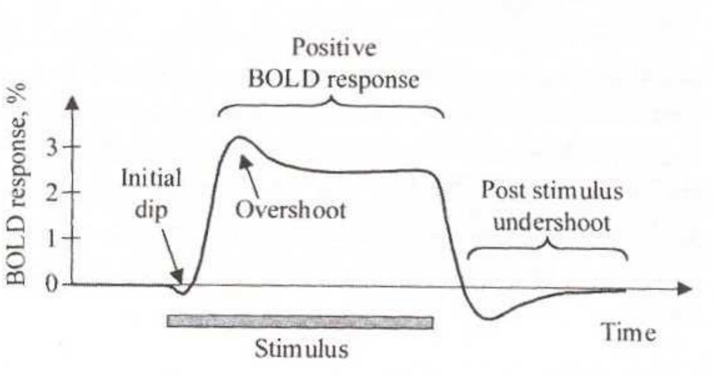

Figure 1.1: Scheme of the typical fMRI BOLD response, [2].

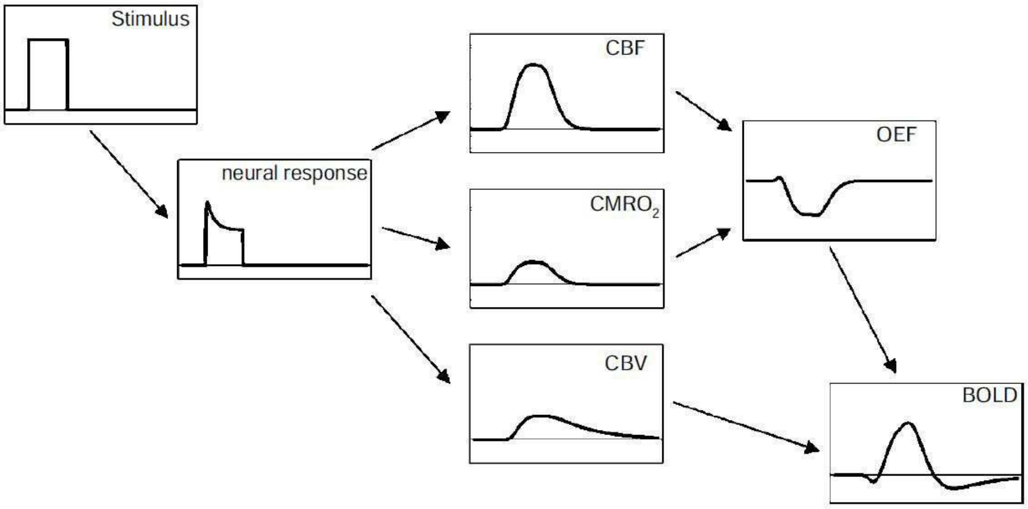

Figure 1.2: Schematic representation of the chain of events leading to the BOLD signal. A stimulus triggers local neural activity, which in turns triggers metabolic activity in the form of a large increase of cerebral blood flow (CBF), a small increase of cerebral metabolic rate of O_2 ($CMRO_2$), and a moderate increase of cerebral blood volume (CBV). OEF is O_2 extraction function. A key aspect of this chain of events is that CBF and $CMRO_2$ are driven in parallel, rather than in series, and potentially be somewhat different aspects of neural activity, [2].

The typical fMRI BOLD response can be schematically divided in three epochs (see Figure 1.1). Immediately after electrical activity starts there may be a brief period of approximately $0.5 - 1s$ during which MRI signal decreases slightly, about 0.5% below baseline. This is a very subtle effect, known as the "initial dip" and is often not seen at conventional $1.5T$ magnetic field strength. Then the BOLD response increases, yielding a robust "positive BOLD response" which peaks $5 - 8s$ after the stimulus commences. An other common feature observed in fMRI experiments is an "overshoot" period during the early positive BOLD response. It is this positive BOLD response ($2 - 3\%$ signal change at $1.5T$) that is used in most fMRI experiments. Finally, upon cessation of stimulus, there is a return of the BOLD response to baseline, often accompanied by a "post-stimulus undershoot", during which the response passes through baseline and remains negative for several tens of seconds. Eventually, the response returns to baseline.

1.1.2 Measurement of brain activation: the BOLD signal

1.1.2.1 Generating the contrast

BOLD fMRI image contrast arises from changes in the local magnetic susceptibility. One mechanism depends upon the fact that the microvascular MR signal in T_2 and T_2^* weighted images is strongly influenced by the oxygenation state of the blood. The rate of loss of proton spin phase coherence is a measure of T_2 and local magnetic field homogeneity (T_2^*); this can be modulated by the presence of intravoxel deoxyhaemoglobin. This BOLD effect can be observed by non-invasive MR imaging at high magnetic fields (the BOLD effect has a maximum amplitude of only 2 or 3% at $1.5T$). The BOLD imaging technique does not measure tissue perfusion or flow directly, however, because over 70% of the brain's blood lies within the microvascular capillaries and venules, the measurement of the magnetic susceptibility-induced T_2^* signal loss is thought to most reflect the regional deoxyenation state of the venous system. In addition, proton perfusion and diffusion through changing local gradients modulated by changing oxy-/deoxyhaemoglobin levels has a direct impact on the observed T_2 relaxation times, which is another mechanism of tissue contrast generation. Amongst these mechanisms, the T_2^* effect is larger by factors of 3 to 10 and is the dominant and most widely-studied mechanism employed in fMRI, [1].

In short, the response to a local increase in metabolic rate is an increased delivery of blood to the activated region. Such a change in haemodynamics produces small alterations in T_2 or T_2^*, which can be visualized as changes in MR image intensity (approx. $1 - 10\%$).

Normal blood can be considered simply as a solution of haemoglobin ($10 - 15mg$ haemoglobin/$100cm^3$). When bound to oxygen, haemoglobin is diamagnetic, while deoxygenated haemoglobin is paramagnetic. Magnetic flux is reduced in diamagnetic materials while paramagnetic materials have an increased magnetic flux: a change in haemoglobin oxygenation therefore leads to changes in the local distortions of a magnetic field applied to it. During the initial increase in oxygen consumption, oxygen is taken from diamagnetic oxyhaemoglobin, leaving behind paramagnetic deoxyhaemoglobin, which makes the magnetic field experienced by protons in surrounding water molecules less homogenous and decreases the magnetic resonance signal from these protons. During the subsequent increase of blood flow (which in fact partly overlaps with the increase of O_2 consumption), the initial tendency to an increase in deoxyhaemoglobin level is converted to a decrease, by the delivery of fresh oxygenated blood, thus increasing the magnetic resonance signal. It is this delayed decrease of deoxyhaemoglobin level, reflecting a local increase in blood flow, that dominates the (positive) fMRI signal detected in most BOLD imaging experiments. Thus, the size of the BOLD fMRI signal is determined by the difference between the amount of blood flow increase, which increases the signal, and the use of O_2 by neurons, which reduces the signal.

The rate of signal decay is faster if there are local field gradients that the molecules can diffuse through over the time course of a single TE. As molecules move into regions of different local fields, their resonance frequencies change slightly, lowering the coherence of the nuclear spins. This leads to more rapid decay of the net signal. In the presence of local magnetic field inhomogeneities the rate of signal decay is expressed by the T_2^* relaxation time. In regions of rapidly changing local magnetic field (e.g. in tissue adjacent to a blood vessel filled predominantly with paramagnetic deoxyhaemoglobin) the T_2^* can be substantially shorter than the T_2. This provide the mechanism for generating contrast that is used in functional magnetic resonance imaging. The presence of any substance in a magnetic field alters that field to some extent. Certain metal elements such as gadolinium and dysprosium have an inherently high magnetic moment relative to water or air, and experience pronounced polarization when placed in a magnetic field. The degree of this effect is referred to as the "magnetic susceptibility". The iron in blood haemoglobin is a superb inherent magnetic susceptibility-induced T_2^*-shortening intravascular contrast agent found in every tissue. It is therefore used as a local indicator of functional activation because oxygenated arterial blood contains oxygenated haemoglobin, which is diamagnetic and has a small magnetic susceptibility effect. It does not, therefore, significantly alter the regional magnetic field and does not greatly affect tissue T_2^*. Deoxygenation of haemoglobin produces deoxyhaemoglobin, with a significantly more paramagnetic species of iron due to the four unpaired electrons, and this species disturbs the local magnetic field, B_0, in a region of tissue leading to the large observed magnetic susceptibility effect. The balance of spatial and temporal alterations in local concentrations of deoxygenated to oxygenated iron affects the local observed T_2^* by causing fluctuations in magnetic susceptibility. Arterially delivered blood consists mostly of oxyhaemoglobin, however, as HbO_2 passes through the capillary bed, the local concentration of deoxyhaemoglobin (Hb) increases and often predominates. Therefore, a T_2^* gradient can exist across the vascular tree from a diamagnetic HbO_2-rich environment (with a longer relative T_2^*) to a more “paramagnetic” Hb environment with a shorter T_2^*. The local T_2^* critical in fMRI contrast is thus determined by the balance of deoxygenated to oxygenated haemoglobin in blood within a voxel, which in turn is a function of local arterial autoregulation or vasodilation. By increasing the flow of oxygenated blood or reducing oxygen extraction to a region in the brain an increase in local, intravoxel increase in T_2^* occurs, which in turn leads to an increase in image intensity. An increase in oxygenated arterially delivered blood in response to local activation will result in more oxygenated iron in the capillary and venous vascular beds, thereby creating a relatively longer regional T_2^* and an image intensity increase.

Experiments by Thulborn et al., [7], characterizing T_2 changes, demonstrated that the T_2-relaxation rate of blood varies exponentially with the proportion of deoxygenated haemoglobin in a fashion precise enough to allow determination of blood oxygenation directly from the line width of the water proton MR resonance signal of blood. This effect increases with applied magnetic field strength (based on differences in magnetic susceptibility between blood cells and the surrounding medium).

Experiments by Ogawa et al., [8], characterizing T_2^* changes, described the first BOLD contrast imaging experiment: gradient echo MR images of a cat brain showed signal loss around blood vessels when the animal was made hypoxic and the effect reversed with normoxia. Blood deoxygenation increased the magnetic susceptibility of blood vessels relative to the surrounding brain tissue, which generated local field gradients and locally decreased T_2^* in tissue water around the blood vessels. Ogawa then had the insight to suggest that the effect could be used to image the small changes in the relative blood oxygenation that accompany neuronal activation in the brain.

Both T_2 and T_2^* changes contribute to BOLD contrast, as contrast in BOLD fMRI is determined by both intravascular and extravascular signal changes. With higher magnetic fields and longer TEs, the extravascular contribution increases and the intravascular contribution decreases. Increased oxygenation of blood gives rise to increased signal from water both in blood vessels and from the surrounding brain tissue, but with different mechanisms. Distinction is in the basis of methods to image activation-related changes selectively in tissue as opposed to the draining blood vessels.

As for the signal inside a vessel, considering that a vessel is a single compartment, water diffuses freely between red blood cells and serum, but cannot exchange across the vessel wall to a significant extent within a single TE. Water molecule's precise resonance frequency shifts because of the rapidly changing magnetic field immediately around each red blood cell and with the change in magnetic flux inside red blood cells relative to the surrounding serum. As the blood oxygen content decreases, the magnitude of these local magnetic field differences increases with the proportion of haemoglobin that changes from a diamagnetic to a paramagnetic state: this gives rise to apparent water MRI signal decreases from a T_2 effect.

As for the signal in the tissue immediately surrounding a vessel: with blood deoxygenation, extravascular water within a voxel located close to the vessel experiences a significant local field gradient across the voxel, the magnitude of which depends on the proximity and relative orientation of the vessel and the extent of the change in haemoglobin oxygenation. The variation in magnetic field across the voxel leads to signal dephasing and hence to T_2^* signal loss. Changes in both T_2 and T_2^* for inta- and extravascular water become greater with higher imaging magnetic field strength, but for intra-vascular water the increase is linear and for extravascular water the increase is exponential, [9]. Thus at higher magnetic fields the contribution of contrast change in the brain tissue should increase relative to that from blood in vessels.

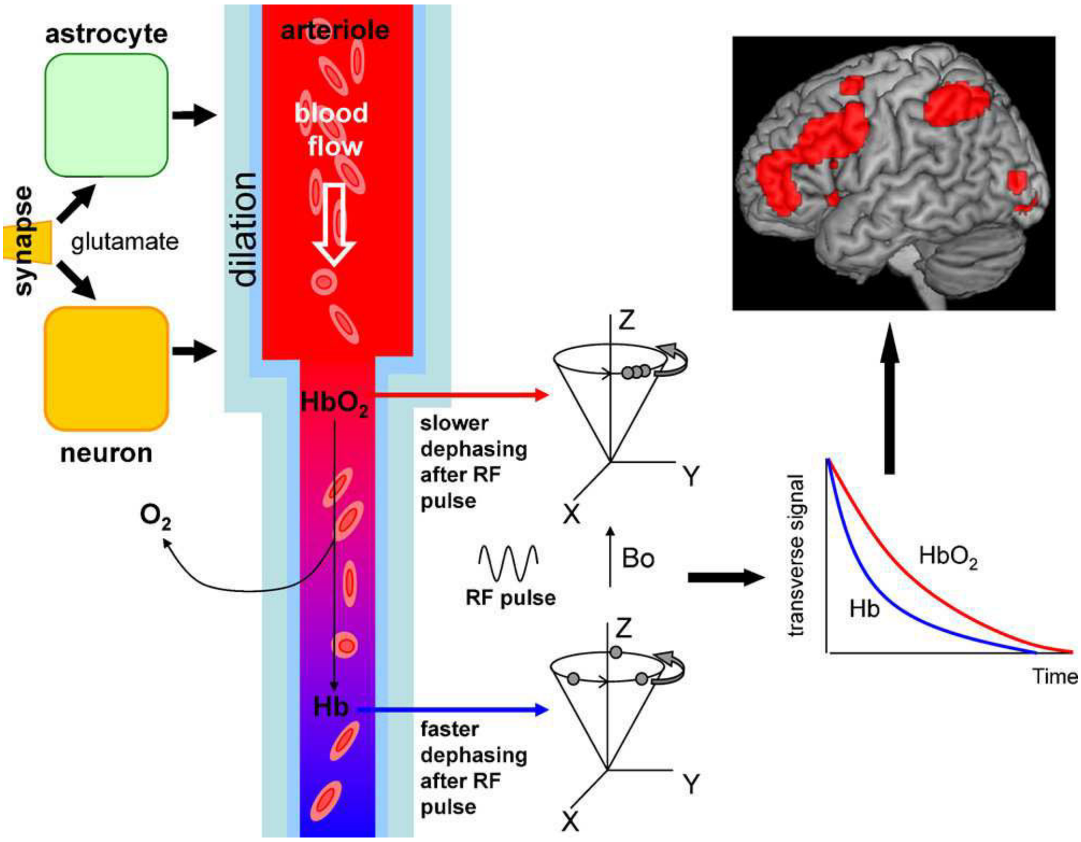

Figure 1.3: Schematic diagram showing the different stages of how BOLD signals are generated, from neurobiology through physics to data analysis, *[5]*. (RF: Radiofrequency Pulse, B_0: static uniform magnetic field, Hb: deoxyhaemoglobin, HbO$_2$: oxyhaemoglobin)

The reliability of the BOLD signal as an indirect measure of neuronal activity has received support from a number of empirical observation, [1], for example the finding that the response within a given subject and within a given region of cortex is extremely consistent from one set of measurements to the next. So, although the signal is temporally blurred, the lag of onset and time course of signal evolution are highly reproducible. Reliable maps of brain activity further suggest that similar levels of BOLD-contrast can be generated reliably across the cerebral cortex. Patterns of activity associated with speech production have been demonstrated reproducible in a comparison across studies employing both fMRI and PET. Several fMRI studies showed patterns of activity within striate and extrastriate cortex that could be predicted on the basis of the well-understood retinotopic organization of primary visual cortex. Such evidence build confidence that the BOLD response is tightly coupled to neuronal activity.

1.1.2.2 Pulse sequence

MR acquisition methods are designed to give both maximal signal-to-noise ratio and maximum BOLD contrast in conjunction with whole brain coverage. Apart from requirements of high SNR, high BOLD contrast and minimal artefacts, imaging speed is a key factor in fMRI. A temporal resolution of a few seconds is necessary to characterize the haemodynamic response. A temporal resolution well below 1s helps to suppress instabilities related to cardiac and respiratory cycles, but at the expense, at least presently, of whole brain coverage.

As for TE optimization, that means individuating the value at which the maximum BOLD effect occurs, it has been showed that BOLD sensitivity does not depend critically on the TE, and TE values in the range $40 - 90ms$ will produce acceptable results.

BOLD contrast arises from effects of field inhomogeneities, therefore it is important to use a sequence that is sensitive to them. We remind that T_2^* for a voxel is not only determined by the microscopic field heterogeneity due to the presence of deoxyhaemoglobin, but also by the macroscopic field homogeneity and the T_2 relaxation process.

$$\frac{1}{T_2^*} = R_2^d + R_2^{mi} + R_2^{ma} \tag{1.1}$$

where R_2^d is the T_2 decay rate (including diffusion effects through microscopic field gradient), R_2^{mi} is the de-phasing term due to microscopic susceptibility effects and R_2^{ma} is the de-phasing term due to macroscopic susceptibility effects. The BOLD effect is predominantly expressed as a change in R_2^{mi} accompanied by a smaller change in the R_2^d term.

An appropriate type of sequences for ultra-fast imaging needed in fMRI are the gradient echo sequences, that are also very sensitive to magnetic susceptibility effects. Gradient echo relies on designing an appropriate form for the gradient waveforms such that at the echo time (TE) all applied gradient effects are refocused and an attenuated echo of the signal is formed. It removes the effects of the imaging gradients, but does not affect chemical shift and de-phasing effects produced by microscopic and macroscopic susceptibility effects.

The FLASH sequence is a 2D-FT gradient echo sequence which uses low flip angle excitation pulses to improve the signal-to-noise ratio. A development of FLASH sequence is to extend the sequence to measure a series of gradient echoes. This is accomplished by reversing the polarity of the read gradient for alternate echoes, which leads to the formation of a train of gradient echoes, with each gradient echo representing a point where the net applied read gradient refocused. This process can be repeated as long as there is appreciable transverse magnetization present. For a train of n echoes each echo provides one line of k-space for each of n images, with each image having a different degree of T_2^* weighting. This multiple echo FLASH sequence increases the amount of information derived from each RF

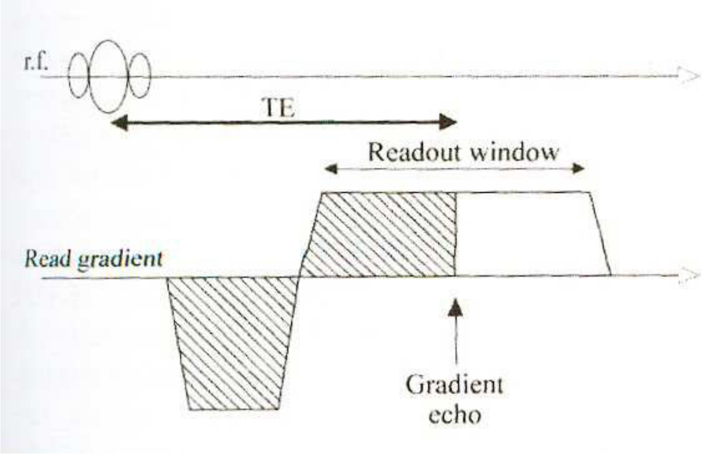

Figure 1.4: Diagram of the formation of a gradient echo, [1].

excitation pulse but reducing the acquisition time may still be necessary. To reduce the acquisition time per image one can retain the concept of deriving multiple echoes from a single excitation pulse, but rather than using each of n echoes to encode one line of k-space for each of n images, the pulse sequence can be altered such that the n echoes encode n lines of k-space in a single image, and this is the typical characteristic of echo planar imaging (EPI). For a low resolution ($64x64$) image 64 echoes can be acquired after an excitation pulse and the complete image can thus be derived from a single excitation pulse.

Today most part of echo planar imaging uses the sequence shown in Figure 1.5: it is a blipped EPI, which samples the whole k-space in a rectilinear fashion. Repeated reversal of the measurement (readout) gradient repeatedly refocuses the transverse magnetization to yield a train of gradient echoes. A large initial phase encode gradient is used to place the first echo at the periphery of k-space and the subsequent blips of the phase encode gradient serve to increment the acquired echoes through k-space. The blips serve to progressively reduce the net phase gradient to zero and then to increment the phase gradient until it reaches the opposite size of k-space. The effects of parameters such as field inhomogeneity, susceptibility effects and chemical shift (which influence the evolution of the phase during the echo train) will affect severely the resulting image.

Off-resonance artefacts of water spins are principally generated by inhomogeneities in the main magnetic field, resulting from poor shimming and susceptibility effects, that induce geometric distortion in the images. Characterizing the field inhomogeneities with a B_0 field map allows the use of post-processing techniques to correct for geometric distortion. An other type of artefact arises from the alternation in the polarity of the readout gradient between successive lines of k-space. This alternation of polarity produces an alternation in the direction of the shift in the echo position that will be induced by the presence of any small gradient imperfection or eddy currents between alternate lines. When the image is reconstructed, this leads to a lower intensity ghost of the image appearing, which is shifted by half of the field of view in the phase encode direction (also known as Nyquist ghost). This artefact can in theory be eliminated by a very precise adjustment of the system. The most widely used method is however to acquire a non-phase encoded data set (reference data) prior to acquiring the EPI images themselves, so that the shift in echo position can be measured from the reference data and the raw data can be corrected accordingly prior to reconstruction.

Moreover, resonance frequencies of the signal from ^{1}H protons in water and fat tissue are separated by $3.44ppm$, therefore signals from fatty tissues are displayed in the readout direction in all MRI sequences. The size of displacement depends on the sampling bandwidth in the readout direction: EPI sequences use a large readout bandwidth so chemical shift in this direction is negligible small. With EPI sequence a chemical shift accumulates also in the phase encode direction. In this direction imaging bandwidth is rather low therefore fat suppression techniques are necessary and have been developed to remove fat signal. They use a frequency selective RF pulse.

Multiple-slice EPI fMRI studies are generally run using a relatively long repetition time ($TR = 2 - 3s$) which allows a large number of slices to be collected (whole brain coverage).

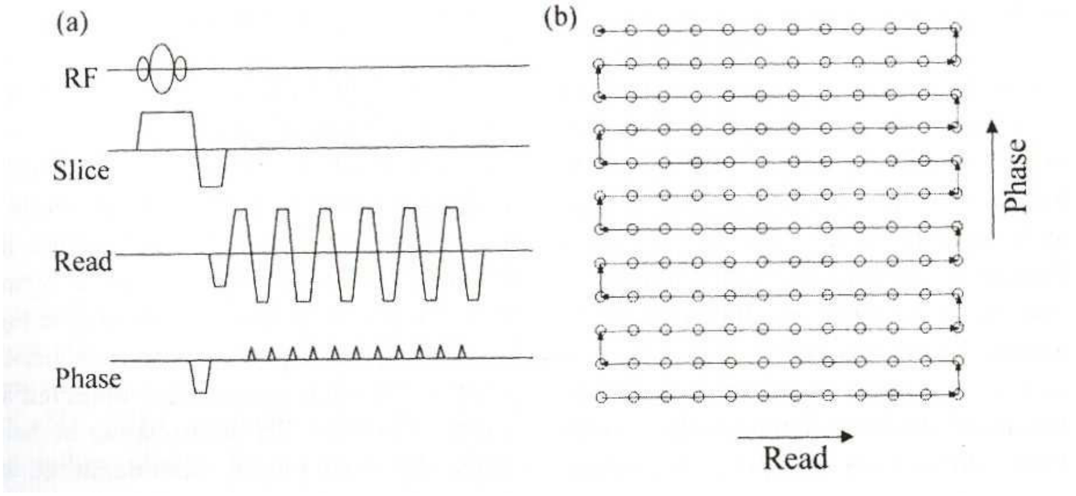

Figure 1.5: Diagram of a blipped EPI sequence (a) and k-space traversal diagram (b) for a $12x12$ point gradient echo image, [1].

Possible alternatives might be 3D gradient echo methods, spin echo methods or variation in how the k-space is traversed. While contiguous multi-slice methods can provide three-dimensional information too, pure 3D methods have some advantages: saturation of nuclear magnetization is spatially homogeneous and this avoid confounding inflow effects, images can be more easily corrected for small head motions and signal intensity can be optimized with higher signal per unit time; anyhow 3D imaging speed needs to be improved if this potential is to be realized. Spin echo methods use a second radiofrequency pulse in the pulse sequence, rather than relying solely on changing the polarity of the readout gradient to refocus the signal into an echo. The refocusing minimizes the effects of field inhomogeneity at time $t = T_E$: at the centre of the spin echo there are no additional phase shift due to macroscopic field inhomogeneities resulting in less signal loss in the image. But longer repetition times are necessary and the refocusing RF pulse also reduces the contribution of the R_2^{mi} term of the BOLD effect. These sequences may be useful in regions (or at field strengths) where T_2^* is short $(20 - 30ms)$. Instead of traversing k-space in a rectilinear fashion, alternative strategies have been proposed (e.g. spiral trajectories, projection reconstruction), as well as advanced methods with reduced k-space coverage (e.g. keyhole fMRI techniques, half-Fourier, sensitivity encoding, UNFOLD).

Anyhow, thanks to its short acquisition time (about $75ms$ per slice) and good sensitivity, multi-slice gradient echo EPI has a very good performance for BOLD imaging and it is the most widely used.

1.1.2.3 Experimental design

fMRI can be used only for determining relative signal intensity changes within a single imaging session; the magnitudes of signal differences between different cognitive or stimulus-induced states can be substantially lower than the reproducibility of signal intensities in independent serial examinations even in the same subject using MRI. This is a fundamental point that must be kept in mind when the fMRI experimental design is developed: the signal changes being measured are quite small. That's why in fMRI paradigm design a key characteristic is repetition.

The most time-efficient approach for comparing brain responses to different tasks during the imaging experiment is the block design. It uses relative long alternating periods (lasting typically about $30s$) during each of which a series of trials is presented. The simplest form is when there are two such states that are alternated through the experiment: an active state, during which the subject performs a specific task, and a rest, during which the subject is, indeed, at rest and doesn't perform any kind of task. In a single fMRI run (continuous period of data acquisition), multiple task and rest blocks are presented to allow the contrast of fMRI signals between task and rest. The signal acquired during one blocked condition is compared to other blocks involving different conditions: the time-averaged signal from one group of sequential trials is contrasted with the time-averaged signal from another group. This approach is straightforward and remains an ideal design for many experiments. However it creates a highly artificial psychological constraint, the task switching may pose specific psychological demands, it can become difficult to control a cognitive state precisely for the relative long periods of each block, many type of stimuli may also show rapid habituation and information regarding the time-course of an individual response is lost within a block.

An other kind of procedure is the so called event-related design, or single-event fMRI. In this case activation data are acquired serially after discrete stimuli or responses. The event-related paradigms differ from blocked paradigms in that individual trial events are measured, rather than a temporally-integrated signal, and they explore signal changes in relation to the onset of individual trials events, taking advantage of the fact that the BOLD haemodynamic response produces a transient response to isolated trial events.

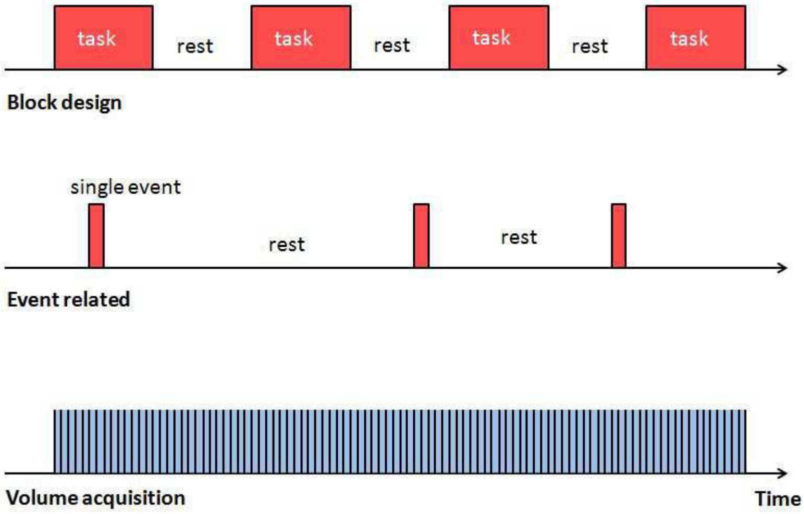

Figure 1.6: Schematic diagram showing the main different paradigm designs for fMRI experiments.

In the last decade, also acquisition in the so-called resting state has been developed, that means that fMRI data are acquired when the patient is at rest, without performing any task for the whole duration of the experiment. For more details, see 1.2.1.

A critical issue in fMRI is to ensure that the subject is performing the required task-behavioural monitoring. A series of devices can be used to submit stimuli and measure responses. For example motor responses can be measured using a variety of devices such as button press or joystic, or asking the subject to perform specific movements, such as finger tapping. Visual stimuli can be submitted with suitable optical devices, as well as auditory stimulation. Even somatosensory, olfactory, gustatory, pain and proprioceptive stimulations can be performed. Primary issues in the design of these devices are that they must be safe for use in the magnet, must not introduce radiofrequency noise and must not lead to head or proximal body movement sufficient to generate artefacts in the images.

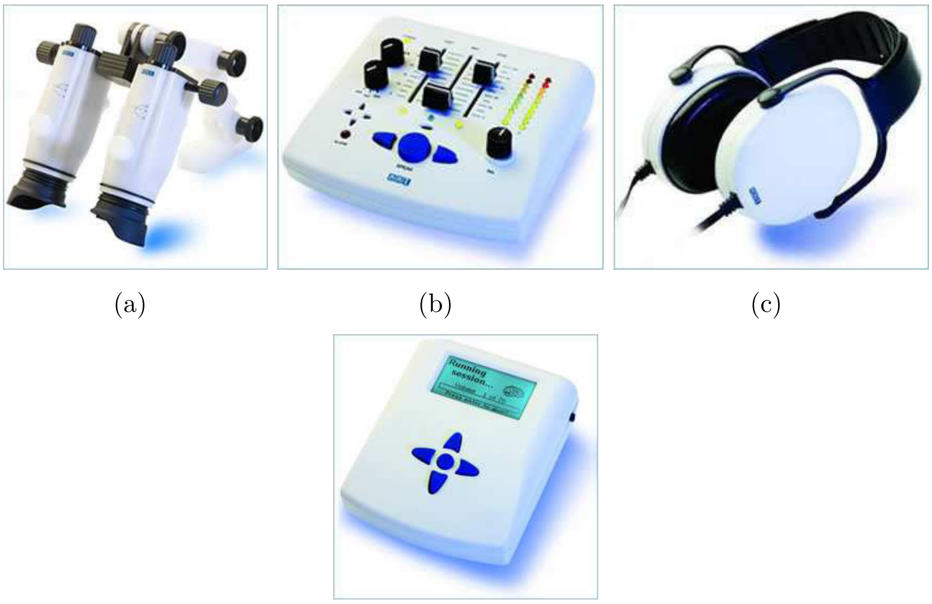

(a) (b) (c)

(d)

Figure 1.7: Examples of instruments to submit stimuli during an fMRI experiment - *source: http://www.nordicneurolab.com/Products_and _Solutions/fMRI_Hardware*

Sometimes it may be desirable or necessary to obtain more general physiologic activity measurements (such as breathing, oxygenation level of the blood, blood pressure, heart beat, carbon dioxide concentration of the blood etc.) for safety, clinical or scientific reasons. Recently instruments able to recording physiological responses also inside a MR scanner have been developed (e.g. pulse oximeter, respiration belt). In a normal psychophysical laboratory movements of subject's body or head are irrelevant, while controlling movements in the context of brain activation in MRI is fundamental: head movement continues to be the single most serious cause of unusable data in fMRI. The first point is to minimize head movements during the experiment. Devices that can be used are foam paddings (wrap back and sides of the head in a comfortable pillow), thermoplastic masks (can be moulded to the shape of the subject's face but the contact and some pressure over the face make them not so well tolerable) and bite bars (they are effective as coupling directly to the skull rather than the scalp, but they are not well tolerated and there is safety concern about choking hazard).

1.1.2.4 Temporal and spatial resolution

BOLD fMRI technique has a temporal resolution in the order of some seconds. Temporal resolution is determined by how often it is possible to take measurements, i.e. by the time needed to acquire a whole volume (repetition time, TR). This is limited by scanner gradient magnet speed, how large the volume one wants to measure over and signal-to-noise ratio of the image (particularly as one images faster). Typically, TR is between $1 - 3s$. Temporal resolution is also limited by the intrinsic temporal resolution of the blood flow response, that is by the underlying physiological signals through which neuronal activity is indirectly measured. Haemodynamic response exhibits considerable temporal blurring in relation to the underlying neuronal activity. Neuronal activity can occur very rapidly (in the order of milliseconds) in response to a sensory events while changes in the haemodynamic response occur much more slowly (in the order of seconds). Moreover, although the robust positive deflection of the haemodynamic response evolves over $10 - 12s$, there may be physiological effects that last longer. As for the temporal dynamics of human brain function, there is no particular temporal division for what is considered fast or slow in the brain. Many low level visions processes occur in the range $15 - 150ms$, while many higher order reasoning processes, or those that require action, take place over ranges that may extend from $250ms$ to many seconds.

Spatial resolution of BOLD fMRI techniques is in the order of a few mm. It depends first on the intrinsic resolution of the imaging experiment (i.e. voxels' dimensions), that usually is worse in the slice acquisition direction. High-field scanners ($7T$ and more) and special MRI techniques can allow better resolution. Spatial resolution also depends on the fact that the haemodynamic response is not spatially very specific to areas of neocortical activation (the following metaphor exists: the brain waters the whole garden for the sake of one thirsty flower). Blood flow changes are more widespread than the underlying neuronal activity (by a few mm) and the hemodynamics that give rise to observed fMRI signal changes originate from arterial and venous sources. The desired response is that of the capillaries embedded within the cortex which are well co-localized with the site of neural activity. As for the spatial scale of human brain function, human brain is segmented into many distinct areas that are functionally specialized; the spatial scale varies: some functions are distributed throughout an entire hemisphere (e.g. speech and language), while other functions have their cortical representations located within both hemispheres and are localized within gyri and sulci tens of millimetres in size.

1.1.3 Overview of fMRI data analysis

During a typical fMRI session a low-resolution volume image of the brain (made of a certain number of slices) is acquired every few seconds; over the course of the experiment 100 volumes or more are typically recorded. A single volume is made up of individual cuboid elements, called voxels. An fMRI data set can be thought of as t volumes, one taken every few seconds, but also as v voxels, each with an associated time series of t time points. Parts of the images taken during stimulation should show increased intensity, compared with those taken whilst at rest, and parts of these images which show increased intensity should correspond to the brain areas which are activated by the stimulation. The aim of fMRI data analysis is to identify, in a robust, sensitive and valid way, these small spatially-localized changes in images intensity that accompany the performance of some experimental task.

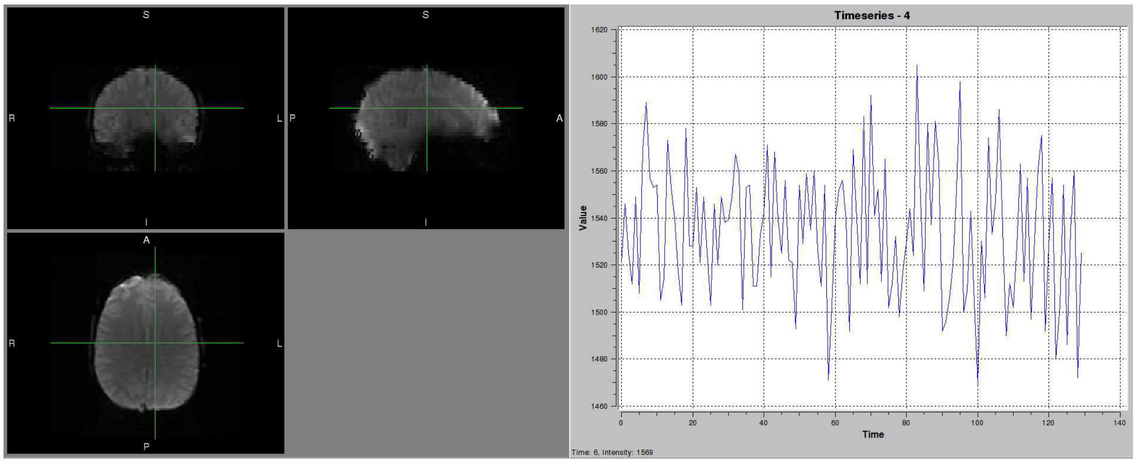

Figure 1.8: Example of a voxel's time-series: on the left brain EPI images, on the right the time-series of the voxel that is indicated with the green cursor in the images.

1.1.3.1 Pre-processing

The aim of data pre-processing is to prepare fMRI data for statistical analysis, for example by removing various kinds of artefacts or conditioning the data in order to maximize the sensitivity of latter analysis and also to increase the statistical validity.

- **Reconstruction from raw k-space data**

  Once data are acquired with the MR scanner, the first pre-processing step is reconstructing the raw k-space data into images that actually look like brains; usually this is done by a software included with the scanner and the output is an image in the DICOM (Digital Imaging and Comunication in Medicine) format. The raw MR signal is obtained digitalizing the demodulated RF signal detected by the receiver coil and it is a k-space data, a spatial frequency transformation of real-space. The reconstruction is usually done with a fourier transform, normally in 2D, and each slice is processed separately. In some cases, some additional phase information collected with the fMRI data enable the correction of the most significant artefact in EPI images, the nyquist ghost.

- **Slice timing correction**

  Each slice in each volume is acquired at slightly different times, as functional volumes are normally formed one slice at a time, so the acquisition of the slices is spread out in time over the few seconds that the total volume capture takes. It is important to adjust the data so that it appears that all voxels within one volume had been acquired at exactly the same time, as later analysis assumes that all slices were captured at the same time. Each voxel's time serie is adjusted so that it really does appear as if all voxels were scanned at the same time (the same correction is applied to each voxel within any slice) and this is achieved by phase shifting the time series of values at each voxel.

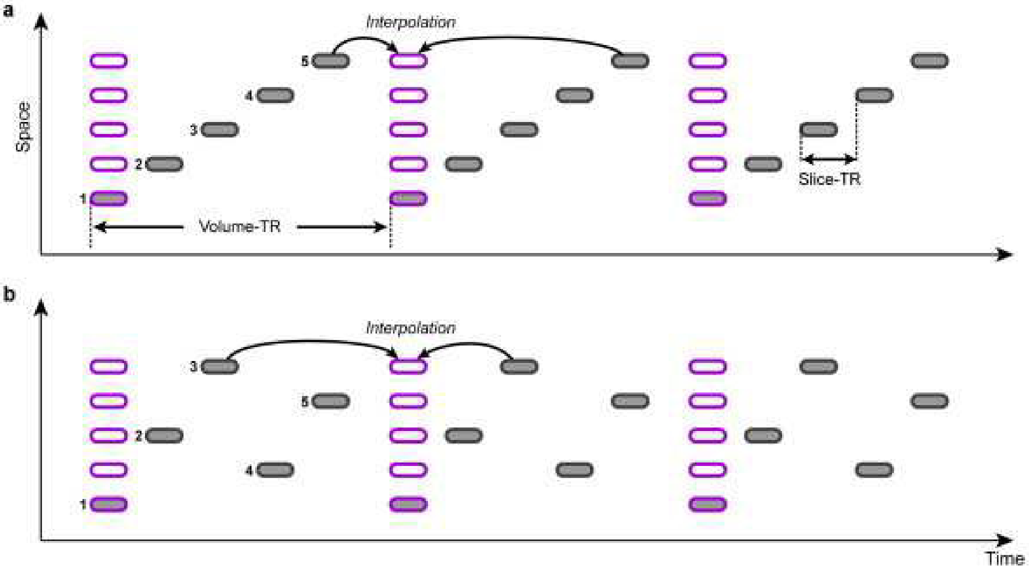

Figure 1.9: Schematic representation of the slice-timing correction process - *source: http://www.brainvoyager.com/bvqx/doc/UsersGuide/Preprocessing/SliceScanTimeCorrection.html*

- **Motion correction**

  Each volume is transformed (using rotation and translation) so that the image of the brain within each volume is aligned with that in every other volume. The assumption is often made that head motion is a rigid-body process (complicating factor is that head motion within the time taken to collect a single brain volume will lead to apparent shape changes in the MRI data). Motion correction consists of computing the image transformation (translations and rotations) that will match an image at time point t to some template or target image. The algorithm is based on automatically computed measures of image similarity and it attempts to minimize or maximize some merit functions used to assess similarity. The reference is commonly chosen to be the first image volume in the fMRI time series.

- **Spatial filtering: blurring**

  There are two main reasons for performing a blurring filter on fMRI images: blurring can increase signal-to-noise ratio in the data and certain latter statistical steps, in order to be valid, may require the functional images to be smoothed. The signal of interest in fMRI case is the change in image intensity which arises as a result of stimuli application (change in intensity due to stimulation is typically between 0.5% and 5%), while the noise is made up of the unavoidable random variations in image intensity which are present even when no stimulation is applied (noise level is typically between 0.5% and 1%). In order for the underlying signal not to be reduced along with the noise due to local averaging, it is required that the extent of the blurring is not larger than the size of the activated regions, therefore attention is needed if very small activation regions are expected. The commonest method is the convolution with a Gaussian profile, commonly with a FWHM between 3 and $10mm$.

- **Intensity normalization**

  Each volume's overall intensity level can be adjusted so that all volumes have the same mean intensity, this is achieved by rescaling of all intensities in an fMRI volume by the same amount (general change in overall brightness). It is applied separately to each volume. Anyhow, there is a widely recognized problem: if strong activation occurs then the activation itself will increase artificially the mean volume intensity. Thus after normalization non-activated parts of the volume will be negatively correlated with the stimulation, and will show up deactivation in the final statistical image. Possible solutions are either not to carry out intensity normalization (it is arguably unnecessary for normal fMRI data) or, if one believes intensity normalization to be necessary, to use a more robust estimation of global intensity, not sensitive to strong local activation.

- **Temporal filtering**

  This step works on each voxel's time series separately and its main point is to remove unwanted components of a time series without damaging the signal of interest. Typically a high-pass filter is performed, to remove all slowly varying unwanted signals (physiological effects or scanner related drifts). It should be remembered that temporal sampling can interact with the original frequency to give an apparent signal at much slower frequency (aliasing) that's why high-pass filter actually not so good at removing physiological effects. Also a low-pass filter may be performed to reduce high frequency noise.

1.1.3.2 Statistical analysis

Different statistical approaches to obtain activation maps exist. An univariate analysis is performed if each voxel's time series is analysed independently (the most common approach, the General Linear Model, is univariate, although cluster-based thresholding, used at the final inference stage, use spatial neighbourhood information and is therefore not univariate). Also multivariate analyses are possible, and in this case all the data are processed together, making more use of spatial relationships within the data than univariate analysis (most model-free methods are multivariate). An other distinction is between the model-based methods, in which a model of the expected response is generated and compared with the data, [10], and the model-free methods, in which the effects of the components of interest in the data are found on the basis of some specific criteria (e.g. Independent Component Analysis [11]).

- **General Linear Model**

  In this model-based method a model is setted up and then fitted to the data. If the model is derived, for example, from the timing of stimulation that was applied to the subject then a good fit between the model and the data means that the data was probably caused by the stimulation. It is normally used in an univariate way, therefore in the following a single voxel will only be considered.

  The linear modelling can be described as in equation 1.2

  $$y(t) = \beta x(t) + c + e(t) \tag{1.2}$$

  where $y(t)$ is the data, i.e. the timeseries of a single voxel, $x(t)$ is the model, c is a constant (for example the baseline -rest- intensity value in the data) and $e(t)$ is the error in the model fitting.

  If there are two, or more, types of stimulus it is assumed that the corresponding responses have different magnitudes, β_1, β_2, ..., β_i and that they add together to produce the final BOLD response (linear model), see equation 1.3.

  $$y(t) = \beta_1 x_1(t) + \beta_2 x_2(t) + ... + \beta_i x_i(t) + c + e(t) \tag{1.3}$$

  If a particular voxel responds strongly to model x_1 the model-fitting will find a large value for β_1. When the model is fitted separately to the data at each voxel, there will be found an estimate of the "goodness of fit" to that voxel's time-course. Different model waveforms within a complex model are often referred as explanatory variables (EVs) as they explain different processes in the data. $x(t)$ is the result of modelling the way in which the BOLD response depends on external stimulus. Let $s(t)$ be the external stimulus (which in block design is a sharp on/off function). The BOLD response at a particular voxel usually occurs between 3 and $10s$ after the stimulus, peaking at about $6s$. This delay and this blurring are modelled by a haemodynamic response function (HRF) $h(t)$. In order to get the best possible fit of the model to the data, the stimulus function is convolved with this haemodynamic response function that mimics the effect that brain's neuro-physiology has on the input function (equation 1.4).

  $$x(t) = \int_0^\infty h(u)s(t-u)\,du \tag{1.4}$$

  The HRF can be modelled as a simple gamma function, see equation 1.5 , but it was also proposed as a differences of two gamma functions that captures

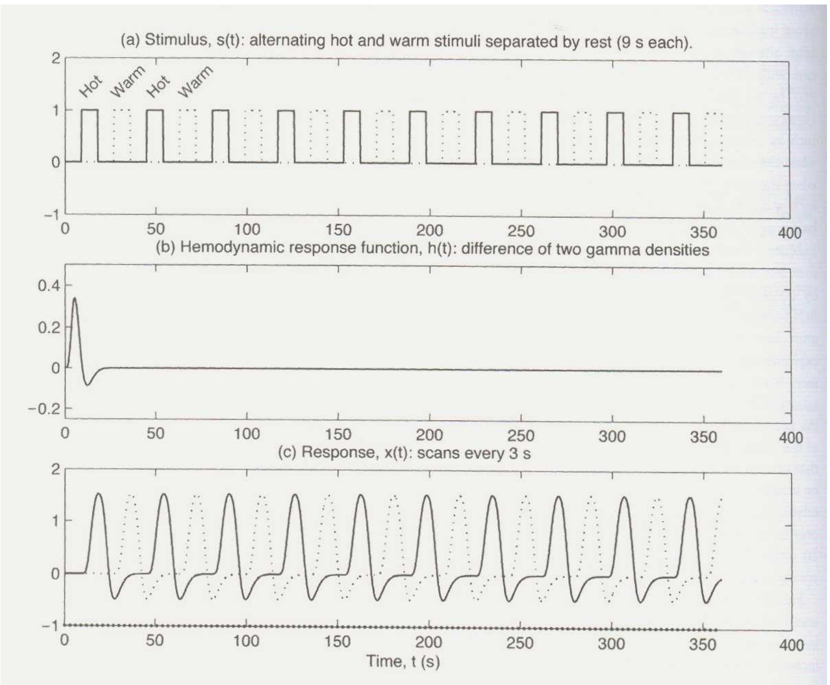

Figure 1.10: Example of the alternation of two different stimuli, separated by rest, (a), the haemodynamic response function, (b), and their convolution, (c), [1].

the fact that there is a small dip after the HRF has returned to zero, see equation 1.6.

$$h(t) = t^b e^{-\frac{t}{c}} \tag{1.5}$$

where $b = 8.6$ and $c = 0.547s$.

$$h(t) = \left(\frac{t}{d_1}\right)^{a_1} e^{\left(\frac{-(t-d_1)}{b_1}\right)} - c\left(\frac{t}{d_2}\right)^{a_2} e^{\left(\frac{-(t-d_2)}{b_2}\right)} \tag{1.6}$$

where $d_i = a_i b_i$ is the time to the peak, and $a_1 = 6$, $a_2 = 12$, $b_1 = b_2 = 0.9s$, and $c = 0.35$.

The resulting convolution is then sampled at the n fMRI volume acquisition times $t_1 ... t_n$ to give the response $x_i = x_i(t)$ at volume i.

The GLM is usually formulated in a matrix notation:

$$\mathbf{Y} = \mathbf{X}\boldsymbol{\beta} + \boldsymbol{\epsilon} \tag{1.7}$$

$\boldsymbol{\beta}$ is the vector into which all of the parameters are grouped into, $\mathbf{X}$ is the matrix into which all of the model time-courses are grouped together into and $\boldsymbol{\epsilon}$ is the vector of noise.

Then solving the problem of multiple linear regression means finding an estimate $\mathbf{b}$ of the unknown parameters vector $\boldsymbol{\beta}$. This is typically done with the method of the minimum SSE (error sum of squares), i.e. minimizing the difference between the measured data and their estimate.

To convert a parameter estimate (PE), in this case **b**, into a useful statistic that describes how significantly the data is related to a particular part of the model, its value is compared with the uncertainty in its estimation, so the t value (PE/standard error(PE)) is evaluated. If the PE is low relative to its estimated error, the fit is not significant. Thus t is a good measure of whether we can believe the estimate of the PE value; it has an approximate t distribution with n degrees of freedom when there is no effect. T statistic images are often converted into z statistic images, the theoretical t null distribution (given the relevant degrees-of-freedom) is converted into a unit-variance Gaussian distribution (which does not depend on degrees-of-freedom). Z is often referred to as a "Gaussianised t", which means that a z statistic of 2 is 2 standard deviations away from zero.

As well as producing images of z values which tell you how strongly each voxel is related to each EV (one image per EV), you can compare parameter estimates to see if one EV is more "relevant" to the data than another. This is known as contrasting EVs, or producing contrasts. To do this, one PE is subtracted from another, a combined standard error is calculated, and a new z image is created.

- **Thresholding**

  Finally, a threshold is applied to the statistic maps, to state at a given level of significance which parts of the brain are activated. The simplest way is to select a significance threshold and apply this to every voxel, but a problem arises: there are many tests being carried out (many voxels in the brain) so there is a multiple-comparison problem. It is not ideal to blindly accept all the voxels with values above the threshold as being activated. A correction to reduce the number of false positives is necessary. A typical correction is the Bonferroni correction, where the significance level at each voxel is divided by the number of voxels (corresponding to the number of comparison being made) and this leads to a very stringent thresholding. An alternative method to voxel-based correction is the clustering method, in which contiguous clusters are defined on the basis of a specified threshold and the z statistic image is thresholded to show which clusters of voxels are activated out a particular significance level: it is possible, indeed, using Gaussian random field theory, to take into account spatial extent of clusters of activations, before estimating significance. Thus instead of assigning a p-value to each voxel, clusters of voxels are created on the basis of an initial thresholding, and then each cluster is assigned a p-value, which may or may not pass the final significance test. Often this method is more sensitive to activation than the voxel-based methods.

1.1.3.3 Multi-subject statistics

It is common to run an fMRI experiment several times (on the same subject - on different subjects) in order to increase the sensitivity of the overall experiment and to allow the generalization of any conclusions to the wider population from which the subjects were selected. Therefore, after the single session analysis, multi-sessions or multi-subjects analysis are performed. The first necessary step is to align the brain images from all sessions into a common space, and this is done through registration (see 1.1.3.4), either on the raw data or on the statistic maps created in the single session analysis; then a variety of statistical methods for combining results across sessions or subjects, or to compare different group of subjects, exist. The main distinction is between the fixed-effects model, that assumes that all subjects within a group activate equally, and is only interested in within-session errors, and the random-effects (or mixed-effects) model, in which the analysis additionally takes into account between-session errors, making less assumption about the data and its results may be valid for the whole population from which the group is drawn.

1.1.3.4 Registration and brain atlases

Registration's basic task is essentially to align two images: it moves or reshapes one image to match the other by finding a relation between the voxels' coordinates of one image and the other and it allows different source of information to be combined. For examples the location of an activation can be compared to the anatomy by registering the functional volume to an anatomical scan of that individual (as well as relative low resolution images, an fMRI experiment will also normally include a single high resolution structural MR scan) or registering the fMRI results from various subjects to a common space allows inter-subject statistical analysis.

The basic concept of a registration is essentially a spatial transformation, that changes the position, the orientation or the shape of structures in the images. The two most common classes of transformations are linear and non-linear. Linear transformations are classified according to their number of degrees of freedom (DOF): 6 DOF rigid body (translation and rotation), 7 DOF similarity (translation, rotation and single global scaling), 12 DOF affine (translation, rotation, scaling and skews). When registering an image of a particular subject's brain with another image of the same brain, a rigid transformation may be suitable; when registering one subject's brain to that of a different subject or to an atlas, it is not expected to achieve good results with only a rigid body, at least a full linear transformation is necessary. In a non-linear transformation, the equations relating the coordinates of the images are non-linear. Many types of non-linear transformation exist, from the most simple, with few DOF, to the more general, with over a million of DOF. They perform well mainly for high-resolution or high-contrast images, when internal detail is indistinct or significantly intensity changes are induced for other reason (BOLD) it is often more appropriate to use linear transformations or, however, low-order warps (i.e. non-linear transformations with few DOF). An important concept in registering images is the interpolation: in order to carry out the image transformation the intensity at positions between grid points (images are acquired and stored as collection of discrete points set on a spatial grid) needs to be calculated. Some of the most common methods are nearest neighbour (takes the value of the nearest original neighbour), tri-linear (three-dimensional extension of linear interpolation), sinc and spline approximation to sinc. As manual registration requires considerable amounts of the user's time and gives somewhat subjective less repeatable results, automatic registration methods are widespread. The most popular approach is to define, for a given transformation, some global measure of similarity between the images, a function which will quantify how similar the images are after a hypothesized transformation has been applied.

As for common space, templates and atlases are commonly used. A template is the average of many brains all registered into any given common co-ordinate system (example: MNI, Montreal Neurological Institute, 305 average). Atlases are also based on a common co-ordinate system, but contain more sophisticated information about tissue types, local brain structures or functional areas. Two basic tasks for which an atlas is helpful are to specify the location of a place in a common reference framework and to find other information, like histological or functional data, about some locations of interest. Their utility exists once the images have being registered to the atlas itself. A significant variability in normal brain anatomy exists and it can be incorporated in atlases by making them probabilistic: two or more tissue type at each location are indicated, each with a probability of occurrence, which reflect how likely a voxel at this location is to contain a particular tissue type.

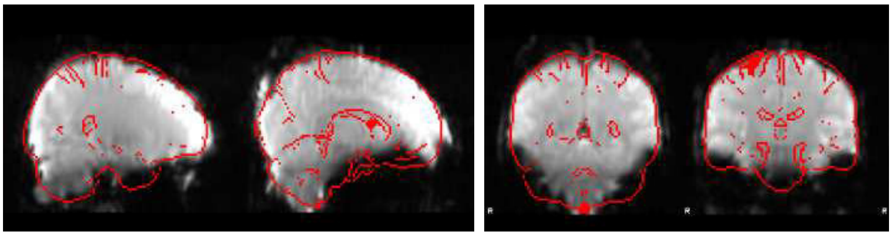

(a) (b)

Figure 1.11: Example of registration of brain functional EPI images (on the background) to a standard template (red line): two sagittal, (a), and coronal (b) views as reported by Feat. It is possible to notice the low contrast in EPI images and some areas on the edge of the brain in which the signal is poor, or almost absent, due to field inhomogeneities in those areas, to which the EPI sequences are sensitive.

1.2 Functional connectivity

The human brain is organized into parallel, interacting systems of anatomically connected areas and in order to understand the functions of these systems measuring connectivity is necessary, [12].

Functional connectivity is operationally defined as temporally correlated remote neurophysiological events and it does not explicitly require that one event is influencing the other (events may be correlated because triggered by common stimulus or neuromodulatory events); the term effective connectivity is sometime used when correlated events can be demonstrated to arise from a direct influence, [13].

There is a strong interest in developing techniques to measure it in the human brain and to link the measured connectivity patterns to information about cytoarchitectonic boundaries and functional response properties, the ultimate goal nowadays seems to be to measure the complete connectional architecture of the human brain, referred as "connectome".

One of such technique is functional connectivity MRI, that provides *in vivo* and non-invasive indirect information about connectivity patterns that define brain systems. Functional connectivity describes the relationship between functionally related brain regions and is a measurement of the spatio-temporal synchrony of the blood oxygenation level-dependent BOLD fMRI signal between anatomically distinct brain regions of the cerebral cortex, [14], [15]. Its bright sides are the flexibility and the range of potential applications for magnetic resonance methods, as well as safety and widespread availability of MR scanners. In contrast to many *in vitro* methods used to define brain functions (such as single unit or patch clamp), methods used *in vivo* generally are concerned not with the behaviours of single neurones but with the activities of large populations of neurones, and this is highly informative, as single neurones do not work independently. fMRI is not the unique, nor the first, technique for functional brain mapping.
In Figure 1.12 different functional brain imaging methods are compared in terms of both their temporal and spatial resolution.

Electrophysiological methods, based on direct mapping of transient brain electrical dipoles generated by neuronal depolarization (EEG) or the associated magnetic dipoles (MEG), define the underlying cortical neuronal events in real time (10-100ms) but provide relatively poor spatial resolution (mm-cm). In contrast, fMRI and PET give information on the increases blood flow accompanying neuronal activation with relatively high spatial resolution (1-10mm) and allowing mapping of neuronal activation deep in the brain, but temporal resolution is limited at best by the rate of the much slower haemodynamic changes that accompany neuronal depolarization. Optical imaging methods (e.g. near infrared spectroscopy) also measure changes in cortical blood flow but because of light scattering by the skull have poor spatial resolution unless the cortical surface is exposed. Metabolic imaging (MRSI or PET) is also possible but has lower spatial resolution and rather poor

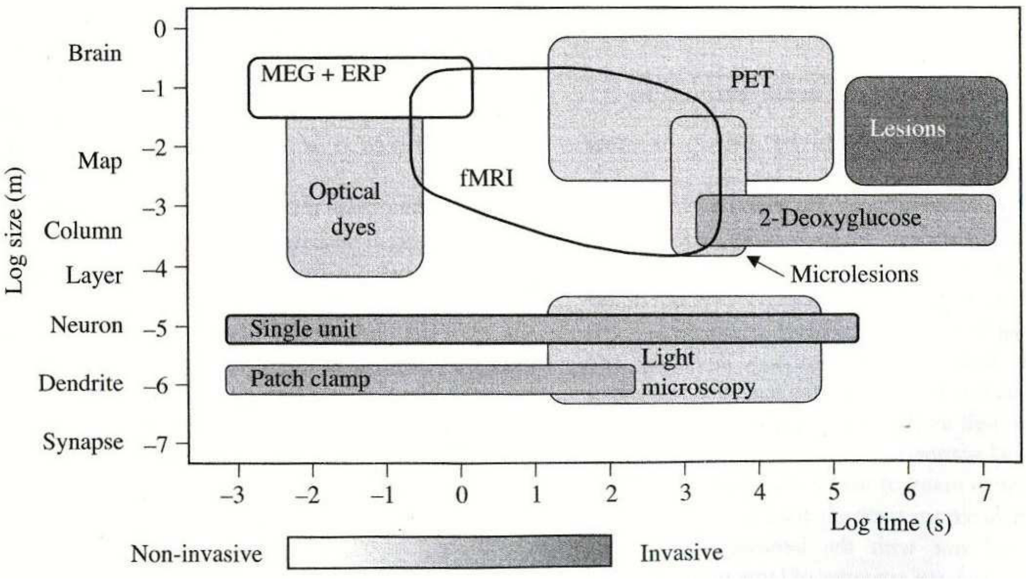

Figure 1.12: Illustration of the relative spatial and temporal sensitivities of different functional brain mapping techniques, [1].

temporal resolution (30s or minutes), even if specificity of the information that they can provide is high. Direct imaging of the blood flow response using perfusion MRI has been used less widely probably due to its much lower sensitivity. Recently, ways in which BOLD fMRI can be integrated with electrophysiological methods are becoming increasingly important.

Until recently majority of information about anatomic connectivity of the human brain comes from studies of non-human primates using invasive tracing techniques ([16], [17], [18]) or from inferences from human brain lesions [19]. Postmortem tracing techniques in human are feasible but of limited success because only able to trace connections spanning short distances [20]. Expanding on related approaches, such as positron tomography ([21], [14]), extracellular recordings [22] or EEG coherence studies [21] , MRI functional connectivity is based on the observation that brain regions show slow, spontaneous fluctuations when measured using BOLD imaging methods.

Another set of MRI techniques that can be used to investigate functional brain connectivity is that based on the diffusion-based methods, i.e. diffusion tensor imaging (DTI) and high angular resolution diffusion imaging (HARDI). They exploit the property that water molecules move along white-matter bundles faster that against them, therefore measuring water diffusion in multiple directions can provide information about the location and the trajectories of axonal bundles. Their main strength is that they directly measure anatomic structures; their main limitation is the inability to resolve complex fiber organization, it was partially overcome by advances in HARDI and advanced algorithms but nonetheless currently applied diffusion techniques sometimes fail to detect known pathways, [12].

In 1995 Biswal et al. [15] first demonstrated the potential of fMRI to investigate functional connectivity by using intrinsic activity correlations: the BOLD signal time course from a region in the motor cortex was strongly correlated with the contralateral motor region and midline regions within the motor system, and coherent fluctuations were observed within individual participants.

1.2.1 Resting state and brain functional connectivity

The earlier approaches to functional connectivity focused on stimulus-evoked modulations, therefore, as usual fMRI studies, subjects used to perform a task during the acquisition. Spontaneous modulation of the BOLD signal which cannot be attributed to the experimental paradigm or any other explicit input exists and it has been viewed as "noise" in task-response studies that usually minimized it through averaging. Then this spontaneous activity has been studied in humans and animals across many spatial and temporal scales and it has been identified as neuronal activity intrinsically generated by the brain.

The ability to map functional connectivity with MRI during resting state was first discovered by Biswal et al. [15]: they found that signal fluctuations in the left and right primary motor areas were significantly correlated even when the subject was not performing any motor task. Correlated fluctuations observed by Biswal were manifest while participants rested passively without any detectable movements. Further work by a number of research groups provided important foundational work for this technique ([23], [24], [25], [26]), remarkably, it would take more than 10 years before resting state functional connectivity was finally accepted and adopted by the larger neuroimaging community.

There is a theoretical motivation for studying spontaneous brain activity: a deeper understanding of brain energy metabolism. Indeed, the resting human brain represents only 2% of total body mass, but it consumes 20% of the body's energy. Task-related increases in neuronal metabolism are usually small ($< 5\%$) when compared with this large resting energy consumption. Therefore most of our knowledge of brain functions comes from studying a minor component of brain activity. There is also an empirical motivation, that arises from the observation that spontaneous BOLD activity is not random noise, but it is specifically organized in the resting human brain, and so studying these spontaneous fluctuations may provide insight into the functional topography of the brain.

During a resting state acquisition the patient lies still in the scanner and refrains from falling asleep. The question about the extent to which this is due to unconstrained behaviour or conscious mentation may arise. Although spontaneous behaviour is likely to contribute to resting state bold fluctuations, it is unlikely to be the predominant source: similar topography of BOLD correlations can be observed across different behavioural states (different resting conditions, task performance, sleep, anaesthesia), coherent spontaneous fluctuations have been observed within systems associated with specific behaviours even in the absence of those behaviours, task-evoked activity due to a specific behaviour seems to be distinct from and superimposed on underlying spontaneous activity, spontaneous cognition results in patterns of neuronal activity in visual regions that are distinct from patterns observed in spontaneous activity, coherent spontaneous fluctuations are present continuously within a large number of neuro-anatomical systems and it is difficult to imagine a behaviour that would simultaneously modulate every known brain systems, [27]. Multiple functional systems have been demonstrated to exhibit correlated fluctuations at rest: visual and auditory systems [28] [29], default network [30], medial temporal lobe memory system [31], language system [32], dorsal attention [33] [34] and frontoparietal control system [35].

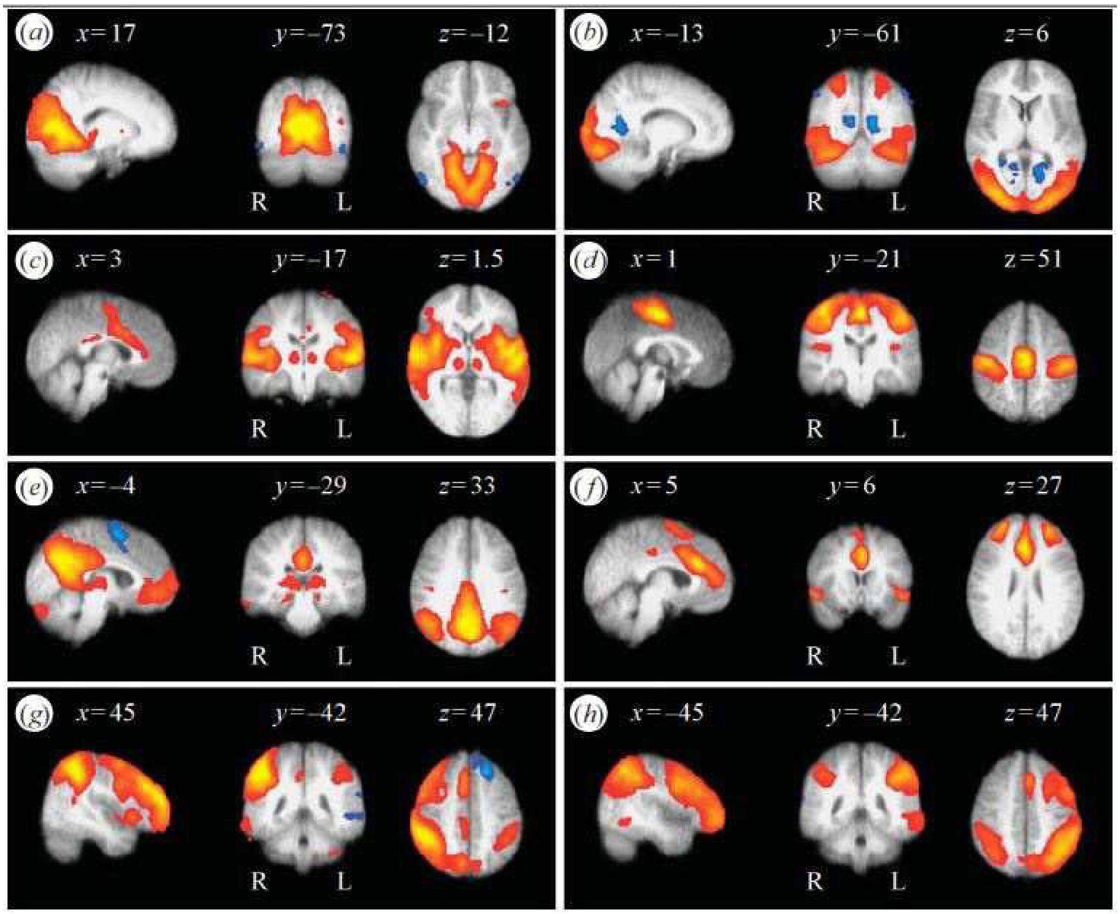

Figure 1.13: Sagittal, coronal and axial views of different spatial brain maps associated with low-frequency resting patterns estimated from a group of 10 healthy subjects. All images have been coregistered into the space of the MNI template. (a) medial visual cortical areas, (b) lateral visual cortical areas, (c) auditory system, (d) sensorimotor system, (e) visuo-spatial system, (f) executive control, (g),(h) dorsal visual stream, [36].

The observation that spontaneous correlations are present ubiquitously across brain systems and persist in multiple states of consciousness raises the question of their origin and whether they provide indirect information about anatomical connectivity [38]. The physiology of spontaneous BOLD, and therefore how spontaneous BOLD fluctuations relate to electrical measures of neuronal activity, is

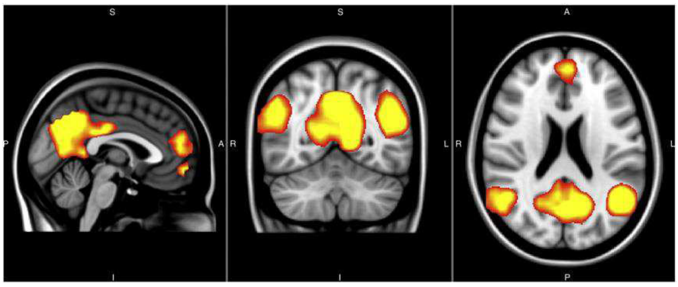

Figure 1.14: The default mode network: specific brain structures that are particularly active in the resting brain and deactivate during a variety of task. The DMN includes the medial prefrontal cortex, posterior cingulate cortex, precuneus, anteriur cingulate cortex, and the parietal cortex, and in a minority of studies also the hippocampus, [37].

not exactly clear yet. A candidate for electrophysiological correlate of spontaneous BOLD fluctuations is the fluctuation in the power of higher frequency electrical activity, [39]. For example brain electrical activity in the gamma frequency band fluctuates at $60 - 100Hz$ but the amplitude of gamma at a particular moment fluctuates at a much slower rate. These fluctuations in power exhibit 1/f behaviour and are correlated across large regions of cortex, [39]. Supports for this hypothesis come from simultaneous recordings of spontaneous fMRI fluctuations with electrical measures of brain activity such as EEG in humans, [40], and local field potential recordings in monkeys, [41]. Fluctuations in the power of high-frequency electrical activity are correlated with spontaneous BOLD fluctuations both locally and across widely distributed neuro-anatomical systems. Another candidate is slow (<0.1Hz) electrical fluctuation that has been observed with DC-coupled EEG, [42]. These fluctuations correlated themselves with changes in the power of higher frequencies. The idea is that slow fluctuations may modulate the power of higher frequency activity, so rapid fluctuations such as alpha or gamma activity might coordinate neuronal activity across small spatial scales, whereas slower fluctuations in the power of these frequency bands may be required for long-range coordination. However whether spontaneous BOLD activity is directly related to slow electrical fluctuations or to changes in the power of higher frequency electrical activity remains to be determined, [27]. Further insight into BOLD physiology may be gained by relating BOLD fluctuations to a rich literature on spontaneous fluctuations observed in various haemodynamic and metabolic parameters, and in neurotransmitter release, remembering that the physiology underlying spontaneous fluctuations in the BOLD signal might not be the same as physiology underlying task- or stimulus-evoked BOLD responses. For example, molecular mechanism of synaptic vesicle release in response to an action potential appears to be distinct from the mechanism involved in spontaneous neurotransmitter release, [43]. Both spontaneous and task-evoked BOLD responses depend on T_2^* BOLD contrast, [26], but future investigations of similarities and differences in the underlying physiology are needed to better interpret spontaneous BOLD activity. Spatial properties of spontaneous BOLD activity distinguish it from random noise, but so do the temporal properties. It follows a 1/f distribution, so there is increasing power at lower frequencies. Some studies, e.g. [23] or [24], focused on understanding which frequencies in this 1/f distribution are responsible for the spatially specific correlation patterns: essentially frequencies below 0.1 Hz. Currently, it is still unclear how the magnitude of spontaneous BOLD fluctuations should be interpreted. There are lines of evidence that indicate that intrinsic BOLD fluctuations are constrained by anatomic connectivity, i.e. that fluctuations are driven by intrinsic activity events constrained by anatomy. Such as a case study where spontaneous correlations were assessed before and after the reception of the corpus callosum, finding a significant loss in interhemispheric BOLD correlations while intrahemispheric correlations remained unchanged, [44]. In a study on monkeys, [45], patterns of spontaneous synchronous fluctuations showed significant overlap with an anatomical network revealed by retrograde tracer injection. Reinforcing this possibility, combined diffusion-based and resting state functional methods provided initial evidence that bold signal correlations between regions are mediated by direct and indirect anatomic projections. For example cortico-cortical axonal pathway densities among regions covering the entire cortex (measured with diffusion-based imaging, [46]), showed a significant relationship to the strength of spontaneous fluctuations among those same regions. However it is difficult to directly assess anatomical connectivity in humans. Usually this is done with studies on patiences with abnormalities. The relationship between spontaneous BOLD correlations and anatomical connectivity using DTI, suggests some relationships but this combination is often limited by not having spontaneous BOLD and DTI data from the same subjects or by restricting the analysis to adjacent gyri, [12]. At the same time, there is also evidence that functional connectivity is not merely a reflection of direct structural connections. For example functional connectivity results are consistent between passive and active task state, while performing a task can induce regional variation in correlation strength indicating that functional connectivity can be modulated despite unchanged structural connectivity, [47]; moreover functional connectivity exists between regions that do not display direct anatomic connectivity, [45].

As far as potential clinical applications of resting state fMRI are concerned, [12], one class of applications rely on the basic idea to use the strength of correlations between functionally coupled regions as marker of brain system integrity. It seems surprisingly powerful for detecting dysfunction across a wide range of disorders and it is a high sensitive technique but the generality of detectable deficits whether disruption of large-scale brain system is a common outcome of many underlying processes and whether functional connectivity MRI is sufficiently specific for clinical use or not is still an open question. Another class of clinical applications concerns the presurgical planning: treatments of epilepsy and brain tumors may involve the neurosurgical removal of brain tissue, maps of the locations of functioning brain systems critical information allow the surgeon to maximize the size of the recestion while minimizing the damage. For this use, an important bright side of resting state fMRI is that it can be performed while subject is at rest or under light anaesthesia.

1.2.1.1 Methods for analysing spontaneous BOLD data

The methods used to study spontaneous BOLD activity have the aim to identify spatial patterns of correlated spontaneous fluctuations in the brain. Several approaches and techniques exist, in the following the the most common ones are briefly outlined.

The seed-based connectivity analysis is the oldest method, and was first introduced by Biswal et al. in [15]. It consists of extracting the average BOLD time course from a region of interest (seed region) and then determining the temporal correlation between this extracted signal and the time course from all other brain voxels. It is widely used, it has an inherent simplicity, a good sensitivity and it's easy to be interpreted. Its main disadvantages are that its results depend on the a-priori definition of a seed region, that multiple systems cannot be studied simultaneously and that the extracted waveform may not be a true independent variable when assessing statistical significance. Anyhow it may be particularly useful if the interest is in investigating connections with specific areas of the brain.

Also the hierarchical clustering requires a-priori definition of seed regions but instead of extracting time course from just one, or few, seed region, time courses are extracted from many brain areas and then a correlation matrix is constructed. A clustering algorithm may be used to determine which regions are more distantly related and also hierarchical trees or topological maps can be constructed, [48]. The analysis of networks properties and graph theory can be applied to characterize global and local properties of brain networks (e.g. [49]) in ways that are not captured by focusing on individual brain systems or distinct patterns of connectivity. Graph theoretical analysis allows abstract properties of complex systems to be quantitatively characterized and mapped, with simple metrics derived to capture the global tendencies and local topological properties.

Independent Component Analysis (ICA) has been first applied to fMRI data by McKeown et al., [11] and [50], and then it has become a quite common approach ([36], [29], [28], [51]); for some information about ICA in fMRI data, see Appendix A. It doesn't require a-priori definition of seed regions as the algorithms analyse the entire BOLD dataset and decompose it into components that are maximally independent in a statistical sense. Each component is associated with a spatial map, some maps corresponding to noise components, others to neuro-anatomical systems. The method is data-driven and automatically isolates sources of noise, but it is highly dependent on the number of components. Moreover, sophisticated algorithms introduce interpretive complexities and the user must determine which components reflect noise and which ones look like neuro-anatomical systems, introducing a-priori criteria for system selection.

1.2.1.2 Physiological noise in fMRI data

Before analysing resting state data identifying spatial patterns of simultaneous fluctuations, it is important to consider and take account of the various possible sources of non-neuronal noise. There are several methodological issues associated with the application of functional connectivity MRI: raw BOLD signal time courses may be noisy due to thermal noise, system noise, participant motion and physiological sources such as cardiac and respiratory cycles. This noise introduce reasons why two regions of the brain could have similar MRI signal fluctuations: for example head motion results in correlated signal changes at the edges of the brain and in regions with large spatial variations in image contrast, or physiological processes such as cardiac pulsation and respiration can lead to correlated signal fluctuations in the brain.

Thermal noise and system noise are related to the properties of the scanner and are intrinsic to the imaging process. Thanks to technical improvements in MRI hardware the severity and the frequency of occurrence of these artefacts have been significantly reduced. System noise may be a result of static field inhomogeneities due to imperfect shimming, nonlinearities or instabilities in the gradient field and off-resonance or loading effects in the radiofrequency transmitter and receiver coils. An example of this kind of noise is the scanner drift, which results in slow change in voxel intensity over time. The random thermal noise arises primarily from stray currents in the body that induce random signals in the receiver coil. It is spread throughout the raw acquired data and can be accurately described as uniform random Gaussian noise, with the noise in each voxel having the same standard deviation and being independent of the noise in the other voxels. Ideal thermal noise has no spatial structure. It is always present in MRI and can only be eliminated by reducing the sample temperature to absolute zero, which is obviously not practical in fMRI. However in general thermal noise is not of much concern: since it is random, and not related specifically to the experimental task, its effects can usually be mitigated by simply averaging over data points.

Head motion is one of the major sources of fMRI noise in general. Various schemes have been proposed for suppressing motion artifacts in MRI as far as participant motion is concerned. Trying to minimize movements during acquisition is the first step but however is not usually enough. Volumes registration to a reference volume (motion correction) may be applied, recently also the approach of deleting motion components after ICA decomposition has been suggested and motion parameters (resulting from motion correction) could be added as regressors of no interest in the statistical model.

Physiologic-related fluctuations can increase the temporal variance in fMRI acquisition and consequently reduce the sensitivity of studies of BOLD activation. Physiological noise is essentially related to the cardiac and the respiratory process.

Cardiac pulsation results in brain tissue movement and inflow effects leading to correlated signal fluctuations primarily in and near large blood vessels; the effects of cardiac function tend to be rather localized in the brain as a result of vessel-dependant brain pulsatility, [52]. The brain is not a static physical system which undergoes no structural changes during the course of an fMRI experiment. Because of the finite cranial volume, the influx of pumped blood results in a dynamic interaction between the competing space requirements of the blood volume, cerebrospinal fluid (CSF) pools and brain tissue. These physical changes cause variations in the signal measured with fMRI experiments, and these variation can have several effect, such as hiding or masking the changes due to neural activity or leading to voxels activation not actually related with neural activity, especially in resting state experiments. Areas showing high signal variation have a strong correspondence to the locations of the major blood vessels, therefore cardiac driven signal seems to be mostly due to vascular pulsations, [52]. Probably more than one factor plays a role: in-flow enhancement caused by the introduction of unsaturated blood into the imaged slice, flow dephasing between the excitation pulse and the readout, oblique flow displacement and misregistration artefacts caused by the shifting locations of blood vessels, brain tissue and CSF, [52]. Little induced variation is usually seen in tissue distant from major vessels, suggesting that cardiac-induced changes in blood oxygenation at the capillary level are not a significant cause of signal variance in fMRI. This also suggest that cardiac-related bulk brain tissue motion is not great enough to introduce significant signal changes variation as this would also be present in tissue distant from major vascular structures. In the superior regions of the brain the effects of cardiac activity are not so strong, and this is expected as only smaller vessels are present in these regions and due to the dampening that occur along the cerebral circulatory system. On the other hand, variation in signal around the sinuses is not surprising due to the pulsatile blood flow that is unique to cranial veins, [52].

Variability in heart rate is correlated with MRI signal changes throughout gray matter ([53], [54]) and cerebral blood vessels exhibit vasomotion, a spontaneous low frequency (0.1Hz) oscillation in vascular tone and blood flow, [55].

Respiration effects originate from three different mechanisms: rigid body motion of the head (which, in part, is likely to also be reflected in the movement parameters), susceptibility changes in the brain due to movement of organs in the abdomen and respiration-dependant vasodilation or oxygenation difference. These effects are often more spatially global, but can also be localized, mainly on the edges of the brain. Respiration causes changes in the size and susceptibility of the air cavity in the lungs, along with a movement of tissue in the chest and abdomen, both of which lead to variation in static magnetic field within the brain tissue. These variations in field strength and homogeneity lead to a shift of the image and a shading of image intensity mainly in the phase encoding direction, and signal variation due to intravoxel dephasing, [56]. The theory beyond this effect is that when a human body is placed in a uniform magnetic field, its diamagnetism results in a slight decrease in the effective field in tissue. On the other hand, paramagnetic air cavities (i.e. containing molecular oxygen) in the body will tend to increase the effective field in their neighbourhoods. The three-dimensional characteristics of these induced fields are determined by the shape of the body and the size, shape and contents of the cavities, [57]. Therefore changes in magnetic susceptibility associated with variations in oxygen concentration within an appropriate cavity may cause B_0 field variations at some distance.

Finally, additional physiological fluctuations exist due to variations in breathing depth and rate that lead to alterations in CO_2 levels. Since CO_2 is a potent vasodilator decreased breathing depth and/or rate leads to an increased blood flow and, thus, to an increase in the BOLD signal [58], [59]. These alterations are part of a complex feed-back circuit. Fluctuations of arterial CO_2 vary with a cycle of about $0.03Hz$, [60].

It has been shown that the signal and the intrinsic noise in high-field MRI are quadratic and linear in B_0, respectively, resulting in an SNR proportional to the strength of the magnetic field. These earlier studies characterized the dominant noise by thermally generated random noise from the subject and scanner electronics. In [61] Kruger and Glover developed a model for the intrinsic noise in oxygenation-sensitive MRI of the human brain, expanding the model of the earlier studies by considering physiological noise as a further significant contribution to the total image noise

$$\sigma = \sqrt{\sigma_T^2 + \sigma_S^2 + \sigma_p^2} \tag{1.8}$$

where σ_T is the thermal noise from the subject and scanner electronics and σ_S describes other system noise. $\sigma_0 = \sqrt{\sigma_T^2 + \sigma_S^2}$ is considered the raw noise and has been shown to be proportional to B_0 but independent of the MR-signal strength, [62]; σ_p describes the physiological noise. Kruger and Glover distinguish between two physiological noise terms: σ_B and σ_{NB}. The former describe fluctuations in the transverse relaxation rate closely linked to the brain physiology and is TE-dependant. The latter arises from image-to-image signal fluctuations due to cardiac and respiratory functions and it's not TE-dependant. Both contributions are signal dependant. Thee overall physiological noise can be expressed as in equation 1.9.

$$\sigma_p = \sqrt{\sigma_B^2 + \sigma_{NB}^2} \tag{1.9}$$

Because σ_p increases at the same rate as the signal S, the achievable SNR at high signal strength and high magnetic fields reaches an asymptotic limit.

BOLD fluctuations that most consistently produce correlations within functional networks occur within a range of 0.01-0.08 Hz, therefore the signals of interest are in the low-frequency spectrum and application of a low-pass filter as a preproscessing step is aimed at removal of higher frequencies. However a low-pass filter won't remove signal faster than the Nyquist frequency and slower than the band-pass cut-off.

Several ways to minimize unwanted physiological variations from BOLD data have been developed over the years.

High sampling rate (e.g. $TR < 250ms$) prevents aliasing of higher frequency cardiac or respiratory activity, but this comes with the limitation of reduced spatial coverage, [63]. Earliest studies used very short TR and filtered out physiological fluctuations occurring at about $1Hz$ (cardiac) and $0.3Hz$ (respiration) [64], by using also notch filters. The drawback of this methos is only a few slices of the brain could be imaged: whole brain imaging required a much longer TR (about $2-3s$), resulting in aliasing of cardiac and respiratory fluctuations. A simple low pass filter will not remove them.

Navigator methods correct k-space data using either an auxiliary echo [65] or the scan data themselves [66], [67]. They sample either a projection of the brain or the entire slice and therefore lack specificity in localizing the source of motion, which in turn can cause incomplete correction or can introduce fluctuations in quiescent parts of the brain.

Retrospective correction techniques use heart beat and respiration recordings during the scan to regress out the physiologically induces fluctuations ([68], [69], [70]). They take into account the phase of the respiratory and cardiac cycle at which each image is acquired, therefore respiration and cardiac induced signal fluctuations can be reduced despite aliasing or variations in cycling during acquisition. The first retrospective correction was proposed by Hu et al., [68], and it fits a low-order Fourier series to the k-space time-series data based on the phase of the respiratory or cardiac cycle. Only the data near the k-space origin have adequate signal-to-noise ratio for the Fourier fit to be robust, thus only low-order spatial corrections can be made and this introduces correlation between pixels in the correction. A retrospective correction technique, RETROICOR, similar to the method of Hu but operating in the image domain was suggested by Glover et al. [69]. Also the combination of both respiration volume and heart rate changes was proposed, [53], and often referred to as RVHRcor.

The physiological noise removal techniques described so far (apart from applying temporal low-pass filter, or more sophisticated methods, when TR is short enough to avoid aliasing) require an independent measurement of the pulse and respiration (e.g. using pulse oximeter and respiration belt). There are also some techniques that do not require these measures and that can be applied with longer TR. Noise sources can be isolated from the BOLD data itself trough techniques such as independent component analysis (ICA), removing the components identified as related to noise, [71]. Independent component analysis (ICA) has become a popular, data-driven analysis methodology to investigate non-normal signal relationships in BOLD-weighted MRI timeseries data and it has been shown that, when applied to resting state data, temporal ICA [72] and spatial ICA [36], [29] can isolate voxels whose contribution is primarily from cardiac- and respiratory-related effects. CORSICA uses spatial independent component analysis to identify and remove signal fluctuations that match spatially with patterns of known physiological noise. Anyhow, ICA decomposition is significantly affected by physiological noise and the ICA process alone may be not sufficient to separate physiological noise effects in the brain ([73]).

The method PESTICA, [72], estimates the physiological fluctuations from the fMRI data using a temporal ICA approach and then the obtained estimates can be used with retrospective methods such as RETROICOR.

An other approach is to include nuisance regressors derived from the data itself, i.e regressing out signals that are common to all voxels (the global signal) or signals from region that are likely to have a relatively high degree of physiological artefact relative to the amount of neuronal activity, such as the ventricles or white matter. This global signal regression is quite a common step in processing functional connectivity data and it makes a certain amount of sense, as we are not interested in signal changes that are constant over the entire brain and certain physiological artefacts occur relatively globally over the entire brain. The problem is that global signal necessarily contains a portion of the signal of interest as well and removing it can therefore remove some of the signal of interest and distort the measure of functional connectivity. There are heated debate and controversy about this issue: using the average signals over the white matter and CSF as nuisance regressors improved the specificity of the connectivity maps, [74] and [75], but the use of these kinds of regressors is also discouraged, [76].

Recently new and always more sophisticated methods have been thought, such as the Canonical Autocorrelation Analysis (PHYCAA) [77] or APPLECOR, [78], but they still need to be tested and verified by different groups.

The optimal set of nuisance regressors and pre-processing steps that can produce both the most robust functional connectivity maps as well as reliably reveal individual differences in functional connectivity is therefore still an active area of investigations.

Chapter 2

Simultaneous EEG/fMRI

2.1 Principles of EEG (a brief outline)

Electroencephalography is a completely non-invasive electrobiological measurement that reads scalp electrical potentials generated by brain structures. The electroencephalogram (EEG) is defined as electrical activity of an alternating type recorded from the head surface after being picked up by metal electrodes and conductive media, [79]. The first account, by Richard Caton, documenting the recording of spontaneous brain electrical activity from the cerebral cortex of an experimental animal dates back to 1875. In 1924 Hans Berger carried out the first human EEG recordings: he was able to measure the irregular, relatively small electrical potentials generated in the brain without opening the skull. It was ten years later, in 1934, however, when Adrian and Matthews published their paper verifying Berger's findings, that the concept of "human brain waves" was truly accepted and the study of EEG activity was placed on a firm foundation.

EEG registers variations in electrical field generated by groups of neurons in the brain cortex: when neurons are activated, local current flows are produced, [80]. Membrane potentials, measured with intracellular recordings, of about $60 - 70mV$ exist across the membrane of the nerve with negative polarity in the intracellular space. These potentials are subject to various fluctuations elicited chiefly by synaptic activities. Action potentials do not contribute to the formation of potentials that are recordable from the scalp, indeed EEG signal is primarily produced by post-synaptic potentials: it measures mostly the currents that flow during synaptic excitations of the dendrites of many neurons in the cerebral cortex. The amplitude of the electrical field produced by the propagation of an action potential decreases much more faster than the amplitude of the fields produced by the post-synaptic potentials. The duration of action potentials is very short, of the order of $1ms$, and to produce an activity recordable with a non-invasive method a very high level of synchronization between neurons would be necessary: even a slight asynchrony of few milliseconds will make the summation of action potentials impossible. Instead, synaptic currents fluxes last between 10 and $40ms$ and therefore, as they are slower, even without a perfect synchronization, these potentials can sum more effectively than action potentials, and can produce electrical fields ample enough to be measured from outwards.

If an action potential travels along a fiber which ends in an excitatory synapse, an excitatory post-synaptic potential (EPSP) occurs in the following neuron; if two action potentials travel along the same fiber with a short interval, there will be a summation of EPSP triggering an action potential on the post-synaptic neuron after reaching the membrane threshold; if an action potential travels along a fiber ending in an inhibitory synapse, then hyperpolarization will occur, representing an inhibitory post-synaptic potential (IPSP).

The arrival of an action potential from an afferent neuron causes the depolarization of the pre-synaptic ending, and as a consequence the voltage-dependent channels open. This leads to the synaptic vesicles opening and to the release of neurotransmitters. Most part of neurotransmitters diffuses until they meet post-synaptic receptors. The interaction between neurotransmitter and post-synaptic receptor allows the passage of sodium and potassium ions, leading to a variation in ionic concentration both in the intracellular and in the extracellular space. The movement of sodium and potassium ions across the post-synaptic membrane (transmembran current) leads to a depolarization of the membrane that, if enough ample, could trigger an action potential. Primary transmembraneous currents (brain electrical current consists mostly of Na+, K+, Ca++, and Cl- ions that are pumped through channels in neuron membranes in the direction governed by membrane potential) generate secondary ionic currents along the cell membranes in the intra- and extracellular space. The EPSP has, as effect, two net fluxes of current, one extracellular and one intracellular. The sum of intracellular and extracellular currents is null, and they represent just two aspects of the same biolectrical phenomena: the flux of transmembranic currents in the activated area. The portion of these currents that flow in the extracellular space is directly responsible for the generation of field potentials measured in EEG: differences of electrical potentials are caused by summed post-synaptic graded potentials from cells that create electrical dipoles between soma (body of neuron) and apical dendrites (neural branches).

The cerebral cortex contains two main kind of nervous cells: pyramidal neurons and non-pyramidal neurons. The former are the principal cortex constituent, they have cell bodies with a pyramidal shape and a lot of connections. They project long axons to other regions and their dendrites pass through various cortical layers and allow a good integration of afferent and efferent signals. They are orientated one in parallel to the other ones and their apical dendrites are orthogonal to the cortex surface. Non-pyramidal neurons have oval-shape cell bodies and project short axons to other local neurons. They don't have any preferential orientation in respect to the cortical surface. The simultaneous activation of various pyramidal neurons produces current fluxes, and hence electrical fields, that, given their similar orientation, can sum up and hence can be registered with electrodes positioned on the scalp.

EEG is a measure of the extracellular current flux that is produced by the sum of the activity from a great number of neurons. Surface potentials are mainly the result of the activity of cortical pyramidal neurons displaced in the correspondence of the cortical area below the electrode. EEG measures the potential difference between an active electrode and an indifferent electrode. The electrical contribution of each neuron is extremely small and the signal must pass through various layer of non-neuronal tissue before reaching the electrodes. Therefore, thousands of neurons activated simultaneously are necessary to generate a signal that can be measured with EEG. The amplitude of the EEG signal depends strongly on how the activity of involved neurons is synchronized. Typically the amplitude of the electrical potentials measured on the scalp varies between 20 and $100 \mu V$ and the oscillations have frequencies between 1 and $60 Hz$.

Cerebral matter shows spontaneous activity, constituted by small fluctuations that can reveal different mental states (such as attention or concentration), different conscious states (e.g. sleep or coma) or some pathologic disturbs. These rhythms are classified on the basis of the frequency interval within which they vary and has typical corresponding states: delta ($0.5 - 3Hz$, pathologic conditions when awake, or deep sleep), theta ($3 - 7Hz$, in a variety of mental states, such as sleep and cognitive processing), alfa ($8 - 13Hz$, relaxed wakefulness), beta ($14 - 30Hz$, attention, concentration, cortical areas activated, drugs effect) and gamma ($> 30Hz$, attention, concentration, cortical areas activated).

Cerebral activity can be modified by various events, i.e. by a sensory stimulus or an endogenous process. Event-related potentials (ERP) are specific variation in EEG resulting from a sensory stimulation or a motor event or an endogenous event. They are characterized by a tight temporal relation with the event, variations of the signal power that are correlated with the event and the realignment of the signal phase in respect to the event. Instead, induced responses are variations in cerebral rhythms power whose phase does not realign with the event.

EEG is primarily generated by cortical gray matter and is also influenced by deeper gray matter (thalamus). Source analysis deals with the localization of neuronal generation, i.e. the individuation of the precise location of cortical sources that produce event-related potentials. Both the direct and the inverse problems exist. In the direct problem the aim is to deduce the electrical field distribution on the scalp for a given electrical source localized in a conductive medium or conductive volume; in the specific case, the source is the cortical activated area and the conductive volume is the head. In the inverse problem, instead, the goal is to get the characteristics (position, orientation, intensity) of the electrical source given the surface potential distribution and the characteristics of the conductive volume. In the EEG case, it aims for producing good estimates of the intra-cranial sources that contribute to generate the measured electrical signal.

2.1.1 EEG measurement

Encephalographic measurements employ recording system consisting of electrodes with conductive media, amplifiers with filters, A/D converter and recording device. Electrodes read the signal from the head surface, amplifiers bring the microvolt signals into the range where they can be digitalized accurately, converter changes signals from analog to digital form, and personal computer (or other relevant device) stores and displays obtained data.

Scalp recordings of neuronal activity in the brain allow measurement of potential changes over time in basic electric circuit conducting between signal (active) electrode and reference electrode. Extra third electrode, called ground electrode, is needed for getting differential voltage by subtracting the same voltages showing at active and reference points. Commonly used scalp electrodes consist of Ag-AgCl disks, 1 to 3 mm in diameter, with long flexible leads that can be plugged into an amplifier

Skin preparation consists of cleaning of the skin surface from oil and brushing from dried parts. Using the silver-silver chloride electrodes, the space between the electrode and skin should be filled with conductive paste, also helping to stick. With the cap systems, there is a small hole to inject conductive jelly. A low-impedance contact is desirable at the electrode-skin interface ($< 10k\Omega$), this objective is confounded by hair and the difficulty of mechanically stabilizing the electrode: conductive electrode paste helps obtain low impedance and keep the electrodes in place.

The signals need to be amplified to make them compatible with devices such as displays, recorders, or A/D converters. The amplifier gain is the ratio of the output signal to the input signal. In order to provide optimum signal quality and adequate voltage level for further signal processing, the amplifier has to provide a gain of $100 - 100000$ and needs to maintain the best possible signal-to-noise ratio. In order to decrease an impact of electrically noisy environment differential amplifiers must have high common-mode rejection ratios (at least $100dB$) and high input impedance (at least $100M\Omega$). The common-mode rejection ratio is the ratio of the gain of differential mode (wanted signal) over the gain of the common mode (original input signal between the inputs and ground). A/D converter usually uses minimally 12 bits (discerning 4096 value levels). Ability to resolve $0.5\mu V$ is recommended.

In 1958, the International Federation in Electroencephalography and Clinical Neurophysiology adopted standardisation for electrode placement called 10-20 electrode placement system. This system standardized physical placement and designations of electrodes on the scalp. The head is divided into proportional distances from prominent skull landmarks (nasion, preauricular points, inion) to provide adequate coverage of all regions of the brain. Label 10-20 designates proportional distance in percents between ears and nose where points for electrodes are chosen. Electrode placements are labelled according adjacent brain areas: F (frontal), C (central), T (temporal), P (parietal), and O (occipital). The letters are accompanied by odd numbers at the left side of the head and by even numbers on the right side. Left and right side is considered by convention from point of view of a subject.

Different brain areas may be related to different functions of the brain. Each scalp electrode is located near certain brain centres, however the scalp electrodes may not reflect the particular areas of cortex, as the exact location of the active sources is still an open problem due to limitations caused by the non-homogeneous properties of the skull, different orientation of the cortex sources, coherences between the sources and so on (source analysis).

As for signal distortions, the artefact in the recorded EEG may be either patient-related or technical. Patient-related artefacts are unwanted physiological signals that may significantly disturb the EEG, while an example of technical artefacts may be the AC power line noise.

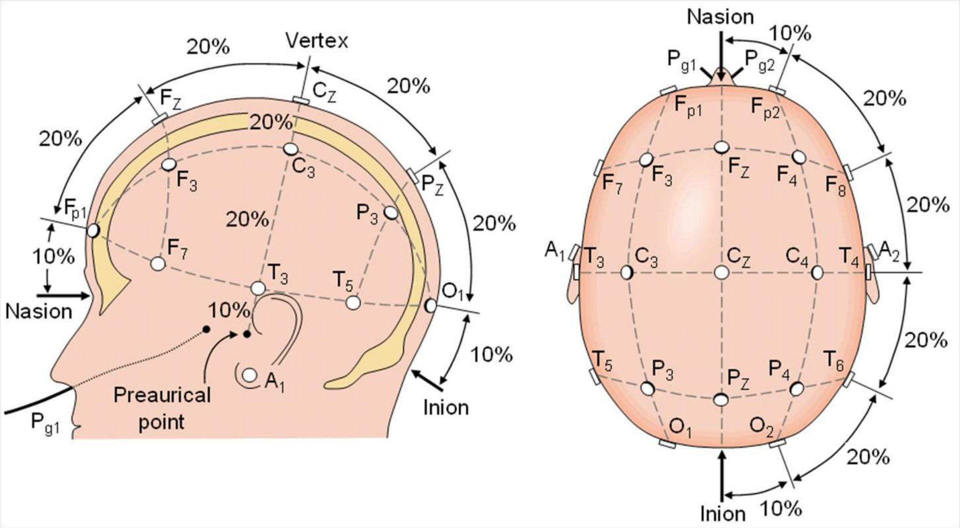

Figure 2.1: EEG electrode setup internationally standardized 10-20 system - *source: J. Malmivuo, R.Plonsey, Bioelectromagnetism handbook - source: http://www.elin.ttu.ee/mesel/Study/Courses//3240BME/Content/1_Bioelectricity/BME_2_bioelectric_signals.h*

2.2 Combination of EEG and fMRI

Simultaneous acquisition of EEG and fMRI can lead to take advantage of the bright sides of both techniques: high time resolution of EEG and high spatial resolution and information from the whole brain with fMRI.

A fundamental limitation of EEG is that precise source localization is difficult: there is not a unique way of defining the numbers or localizations of neuronal generators that can give rise to any given activation pattern measured at the surface of the head, an attractive approach to minimize these difficulties is using fMRI to set limits on the number or localization of sources. This may be achieved by assigning a higher probability to sources that co-localized with fMRI activations.

EEG-fMRI has found application in various fields of neurological studies, as it may provide new insights into brain function and it is promising, indeed the number of applications has increased over the last years.

Its first, straightforward, application, was in studying epilepsy: the simultaneous measurement of EEG and fMRI has been shown to provide reliable information concerning the localization of the regions generating interictal epileptiform activity, [81]. The ability to localize the source of the spike will help in gaining a better understanding of epilepsy.

For a long time EEG rhythms where the sole window on the resting state of the brain. Recent fMRI studies showed the presence of networks in the brain that are active during the resting state of the brain. Hence, investigating a possible connection between EEG rhythms and brain networks is getting a primary interest.

Also during sleep the combination of EEG and fMRI may lead useful information: EEG monitors the different sleep stages, while fMRI follows changes in the default mode network through various stages. Task execution depends on cognitive control and a variety of ERP components are known to be cognitive control markers. They can also be investigated with fMRI, exploiting EEG-fMRI in investigating cognitive control and attention. Also as for visual perception they may be useful, to study what happens with a visual stimulus when it coincides with different phases of ongoing brain activity and loci in the brain

The integration of MRI devices and EEG devices is a critical process, [82]. The first attempts to combine both techniques at the same time dates back to the late 80s. A setup developed exclusively for the intended use of performing combined recordings was constructed in the early 90s by the group of Krakow, Lemieux and Allen. The inability to use digital circuits in the design, due to broadcast interference from internal circuits was solved thanks to optical data transmission, to the recording computer outside the scanner room. Pulse artefact removal (see 2.2.2.1) was the first problem and was resolved by implementing a correction module based on the average subtraction method. Even if combining these two techniques has not been straightforward, as for the patient's safety and due to the presence of artefacts both in EEG signal and in MRI images due to electromagnetic interactions between the two devices, this method is becoming a key method in neuroscientific research.

2.2.1 Safety

The first and most detailed study that systematically addressed the potential safety hazard that exist when EEG and fMRI are simultaneously acquired is by Lemieux et al., [83].

The potential safety hazard is related to the presence of electrical wires connected to the patient in rapidly changing magnetic fields, i.e. by the possible induction of EMFs (electromotive forces), and therefore of currents, in the EEG electrodes and leads by the various electromagnetic fields used in MRI, and hence leading to low-impedance conduction through the patient.

We recall that in MRI imaging there are three electromagnetic fields: the static magnetic field (B_0) homogeneous in the imaged volume, the time varying magnetic gradient fields (frequencies of the order of $1kHz$) and the radiofrequency pulsed field (frequency of about $64MHz$ at $1.5T$).

In EEG the conducting loops, inevitably present in order to measure potential differences, normally have a high impedance (thanks to amplifiers), but however low-impedance loops may form due to a variety of reasons: lead wire in contact with the patient, two leads in direct electrical contact, a single wire bending on itself, failure of EEG pre-amplifiers circuit and conducting loop due to the capacitance between leads running parallel with the induced current flowing through the patient. Currents are induced in human body under normal scanning conditions, but if there are conducting loops a concentration of current in low impedance metallic components can appear and hence a high current density in the tissue under an electrode. Contact currents (induced in the body through conductors in contact with the body) were studied irrespective of the EEG-fMRI issue, and health risks were documented: ulcers, electric shock and heating. Moreover, current may flow even if no loop is present: extended wires acting as dipole antennas will pick up the electrical component of RF field; this won't generate any difference of potential higher than usual, but it may cause excessive heating.

EMFs are induced due to three mechanisms:

- fixed loop in rapidly changing gradient fields, i.e. EMF due to switching gradients: EMF (V) in conducting loop placed in a time-varying magnetic field is given by the Faraday induction law (integral form in eq. 2.1).

  $$V = -\frac{d}{dt}\int_A \overrightarrow{B} \cdot \overrightarrow{dS} \tag{2.1}$$

  where $\overrightarrow{dS}$ is an orientated infinitesimal surface element and the integral is over the area comprised within the circuit, A. The right side of equation 2.1 is the rate of change of the magnetic flux through the loop. In this case the rate of change of the magnetic flux is related to the maximum gradient slew rate, s_{max}. Assuming the worst case (three gradient switching simultaneously and loop lying in a plane perpendicular to the field, with an area A and at a distance z from the gradient coil isocenter):

  $$|V_{Gz,max}| = \sqrt{3}s_{max}Az \tag{2.2}$$

- fixed loop in a RF electromagnetic field, i.e. EMF due to RF pulses: field B_1 is circularly polarized and rotating in the axial plane at the Larmor frequency ω_0

  $$V(t)_{RF} \approx -K\omega_0 b_1(t)A \tag{2.3}$$

where K is a gain factor that represents the combined effect of loop position and field inhomogeneity and A is the area of the conducting loop.

- moving loop in the static magnetic field, i.e. EMF due to movement in static field

  $$|V_{mov}| = B_0 \frac{dS}{dt} \tag{2.4}$$

  where $\frac{dS}{dt}$ is the rate of change of loop area normal to the field.

  Movement of the loop while the patient is fixed inside the headcoil will be limited, more significantly may occur due to movement in or out of the bore.

As for heating, in current-limiting resistors the surface temperature rise of a resistor is a function of the power dissipated and thermal resistance, which is function of the head conductivity of the resistor material, its dimensions and to a lesser extent method of mounting It can be caused also by eddy currents in electrode and gel or due to electric field in extended wires due to RF pulses.

Current-limiting resistors have been shown to be a simple and safe way to ensure patients safety. They should be placed as near as possible to the EEG electrode and a series of studies and evaluations can lead to calculate their suitable value.

2.2.2 Artefacts in EEG recordings

The interactions between the patient, the EEG electrodes leads and the magnetic field in the scanner cause artefacts both in the EEG signal and in MR images. The main physical principles which underlie the generation of these artefacts are Faraday's induction law and a blood flow effect (whereby the movement of blood, a conductor, normal to a magnetic field leads to induced potential).

2.2.2.1 The pulse artefact

Providing that patient movement is minimal (requirement for fMRI), artefacts in EEG due to gross subject movement are not a primary concern. However, small pulse-related body movements may produce a pulse artefact (PA), that may result from the acceleration in blood flow in the aortic arch during each heart beat and scalp movement due to the expansion and contraction of scalp arteries, [84]. It is present in a wide area of the scalp and it is also known as balistocardiogram (BCG) artefact. Typically, it is a broadband signal with a high amplitude sharp peak time-locked to the pulse, followed by a complex oscillating waveform. Minimizing PA by preventing small head movement is impractical. Moreover, blood flow effect may also result in PA due to the electric field associated with the pulsatile movement of blood perpendicular to B_0, an effect well known in ECG monitoring and result in an increased T-wave. Its amplitude is proportional to B_0, blood flow, the orientation of flow with respect to B_0 and the proximity of the EEG electrodes to blood vessels. There is a large interindividual variability in PA amplitude, and minimizing it is not easy.

A signal processing techniques to reduce PA was suggested by Allen et al., [84], and it is known as AAS (averaged artefact subtraction). They first performed an experiment to investigate the amplitude and distribution of this artefact, and then implemented and tested a subtraction algorithm that is essentially still used by various software for EEG analysis.

The subtraction algorithm is applied on a second-by-second basis as follows: first, the ECG peaks (QRS complexes) in the previous $10s$ are identified. The average PA wave form for the period ± half the R-R interval, time-locked to the ECG peaks in this period, is then calculated for each referential EEG signal. This average waveform is then subtracted at the time corresponding to the ECG peaks identified during the penultimate second of EEG and the 1-s periods bracketing this. The ECG signal may also contain artefacts due to the same reasons that cause PA in the EEG; detecting a high proportion of ECG peaks is essential, therefore a great effort was made to produce a robust peak detection method, see Figure 2.3.

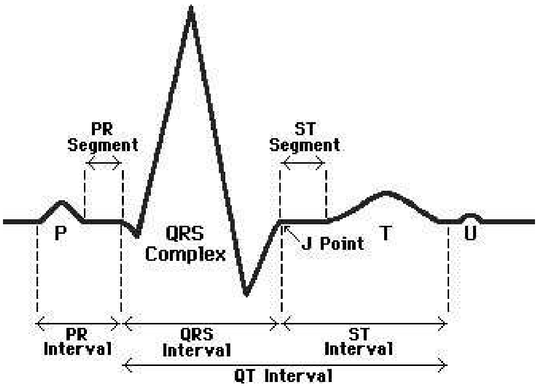

Figure 2.2: Schematic representation of the ECG waveforms - *source: http://www.usfca.edu/fac-staff/ritter/ekg.htm*

Recently, also different techniques, such as ICA, have been getting quite widespread to remove BCG artefacts, and also the combination of AAS and ICA seems to give good results.

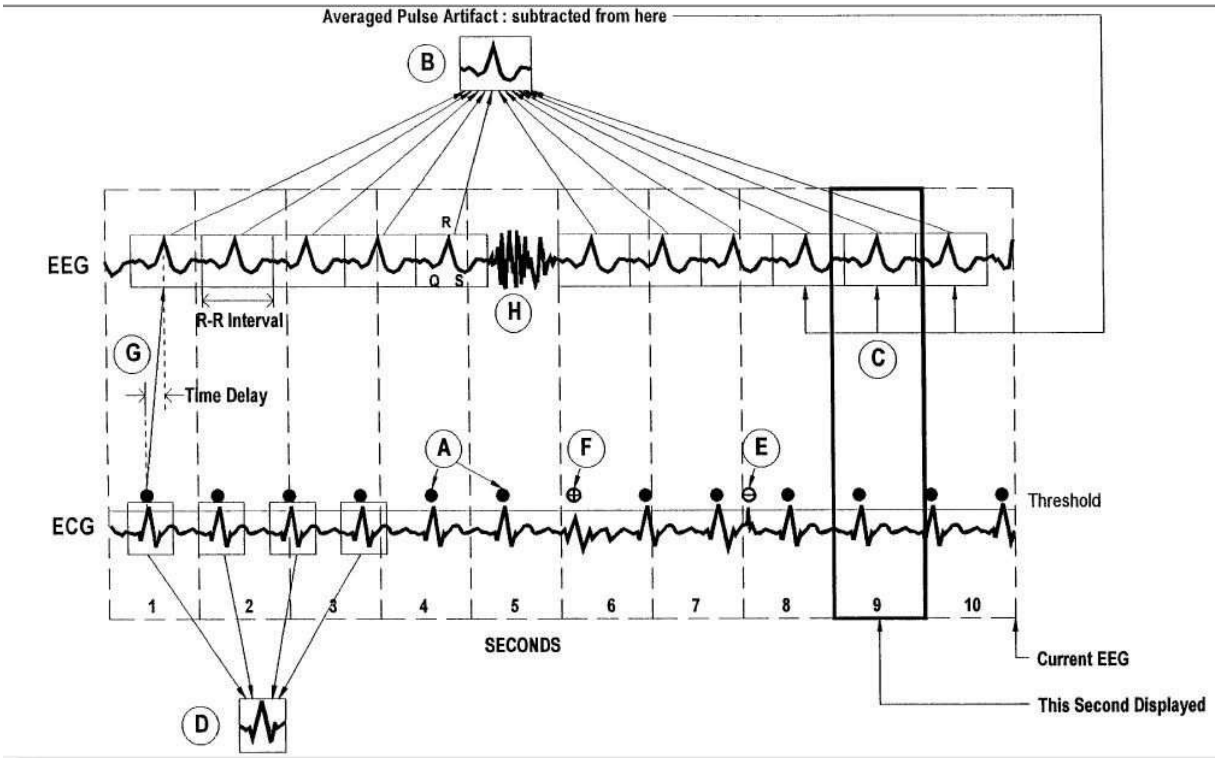

Figure 2.3: Schematic of the PA subtraction method, [84]. (A) ECG peak corresponding to a QRS complex is identified. (B) PA waveforms in the EEG channels, time-locked to the ECG peaks, are averaged. (C) The averaged PA signal for each channel is subtracted from the EEG signals at times corresponding to the ECG peaks. To confirm that an ECG peak detection corresponds to a QRS complex, (D) an averaged QRS waveform is calculated from the first four ECG peak detections with temporal characteristics which indicate a high probability of being QRS complexes, this is then cross-correlated with the ECG waveform at each peak detection. (E) ECG peaks corresponding to noise in the ECG signal are rejected. (F) QRS complexes which are not detected by threshold crossing are identified by detecting an "R-R" interval between successive ECG peaks which is an integer number of the mean R-R interval and extra ECG peaks are added accordingly. (G) The sections of EEG occurring a short time interval after the ECG peaks are averaged. A time interval is necessary as the peak of the PA in an EEG channel normally occurs a short time after the QRS complex. (H) If the section of EEG time locked to an ECG peak contain other artefacts, the section is excluded from the average PA waveforms.

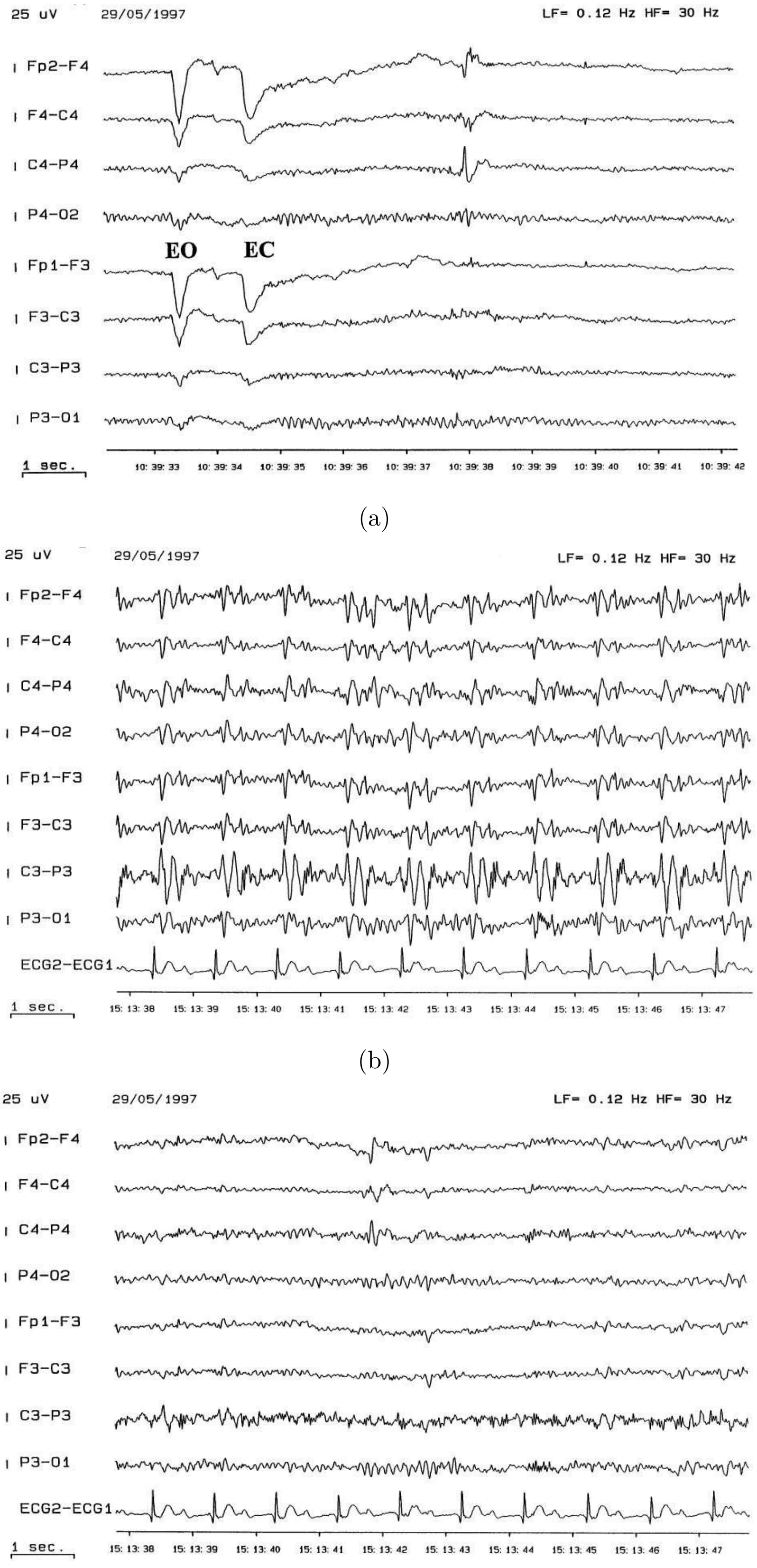

(a)

(b)

(c)

Figure 2.4: Example of PA application from [84]: (a) ECG recording from a normal subject outside the scanner, (b) the same subject inside the scanner, (c) the section of EEG illustrated in (b) but with PA subtraction applied.

2.2.2.2 The MR gradient artefact

The switching magnetic fields applied during image acquisition induce EMF in the electrode leads and head, that result in artefacts in EEG signal. fMRI is normally performed using echo-planar imaging and there are large artefacts induced by the use of gradients in this sequence.

Most of the early studies of EEG-fMRI had used aperiodic fMRI: image acquisition was triggerd immediately after the observation of an event of interest in EEG. This procedure has various disadvantages: events of interested during image acquisition are loss and may leads to confound result and long refractory period after image acquisition is needed to allow complete T_1 relaxation. It was hence important to develop methods to remove this imaging artefact.

Allen et al., [85], started from the observation that waveforms have very low inter-volume variability, therefore the subtraction of the image artefact waveform averaged over a number of volume acquisitions may be effective. The EEG recording system must have a large dynamic range to record both the EEG with appropriate resolution and the image artefact without saturation. Two different fields are applied: RF and gradient. Artefacts induced by RF have a much higher frequency than EEG hence can be reduced effectively by low-pass filtering applied before the EEG amplifier front end. On the other hand, gradient artefact contains components in the EEG frequency range. With common values of maximum rate of change of gradient field assumed to be $25Ts^{-1}$ and the maximum loop assumed to be $100cm^2$, the maximum gradient artefact amplitude is about $250mV$ ($500mV$ pk-pk).

The first stage of this image artefact reduction method is the calculation of an average imaging artefact waveform over a fixed number of epochs. For periodic fMRI sequence with delays between volume scans, an epoch can be defined as the TR, while for continuous fMRI acquisitions, i.e. no delays between volumes, an epoch can be defined as one slice. An fMRI slice-timing signal, which define accurately the time at the start of each slice, is sourced from the scanner and used by the algorithm to synchronize artefact averaging. To optimize calculation of the average artefact a 25-coefficient sinc function is used to interpolate the EEG values synchronous with the slice-timing signal. When subtracting the averaged artefact from the EEG in each epoch, a similar interpolation is performed in the reverse direction to synchronize the averaged waveform to the EEG samples. After subtracting the average artefact, the signals, acquired with a high sampling rate (e.g. $5kHz$) to better synchronize the EEG with gradient activity timing, are smoothed to reduce the likelihood of aliasing in the next process, which is downsampling to $200Hz$ (or similar values), a sampling rate typically used for EEG.

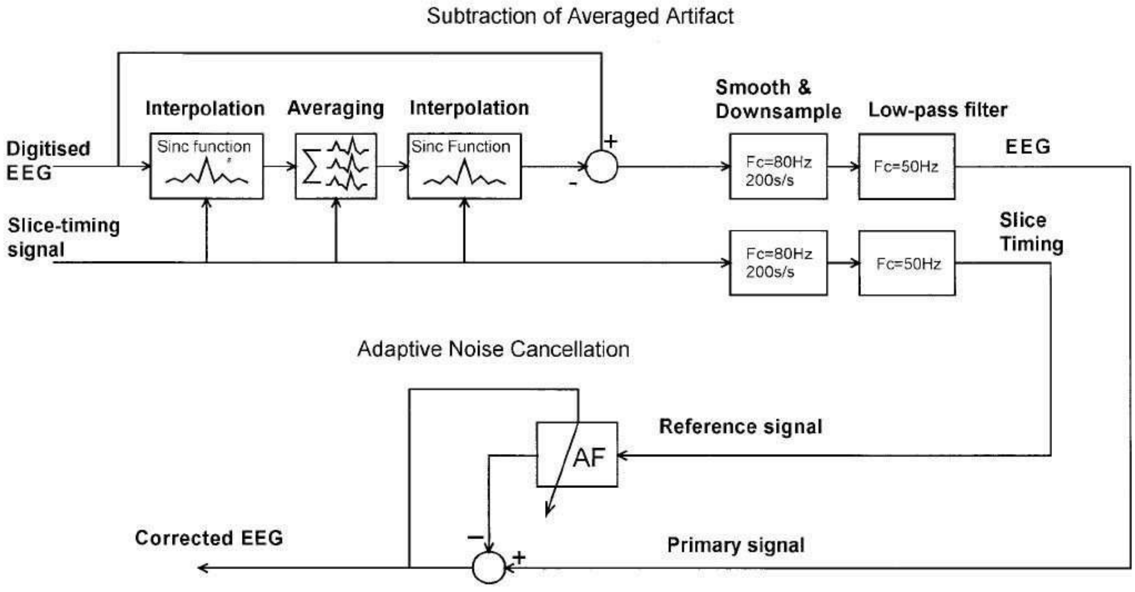

Figure 2.5: Schematic of the image artefact reduction algorithm, [85]

2.2.3 Artefacts in MR images

The effects of EEG devices on MRI images have a lower extent, indeed it is possible to acquire fMRI data in the presence of EEG equipment without making significant modifications to MRI techniques or hardware, [86].

Differences in magnetic susceptibility between the materials used in EEG recordings (electrodes and leads) and the human head may cause inhomogeneity in the main magnetic field, B_0. All materials have a magnetic susceptibility (that is a measure of how readily a material develops a magnetic moment when exposed to an external magnetic field). In most paramagnetic and diamagnetic materials the magnetic moment iduced in an applied field is relatively small, so that the magnetic field perturbation produced by the material is much smaller than the applied field. Unwanted magnetic field inhomogeneity may appear if the wires, electrodes or conductive gel have a significantly different magnetic susceptibility from the tissues of the head, as the field deviation can cause the frequency of precession to vary, leading to two main forms of artefact: image distortion (as in image reconstruction all frequency variation is assumed to result from the effect of the applied magnetic field gradients, any additional field offset translates into a spatial misregistration of signal contributions) and local signal loss if spins at different locations across the slice precess at different rates and consequently get out of phase with one another during the echo time. It is generally localized to the site of electrodes and only penetrates on average distances of the order of $10mm$, given that the average scalp-brain distance is $13.8mm$ the signal loss is not often observed within the brain. By carefully choosing type and amount of materials used in electrodes and leads magnetic field inhomogenity can be minimized, leading to residual effects generally

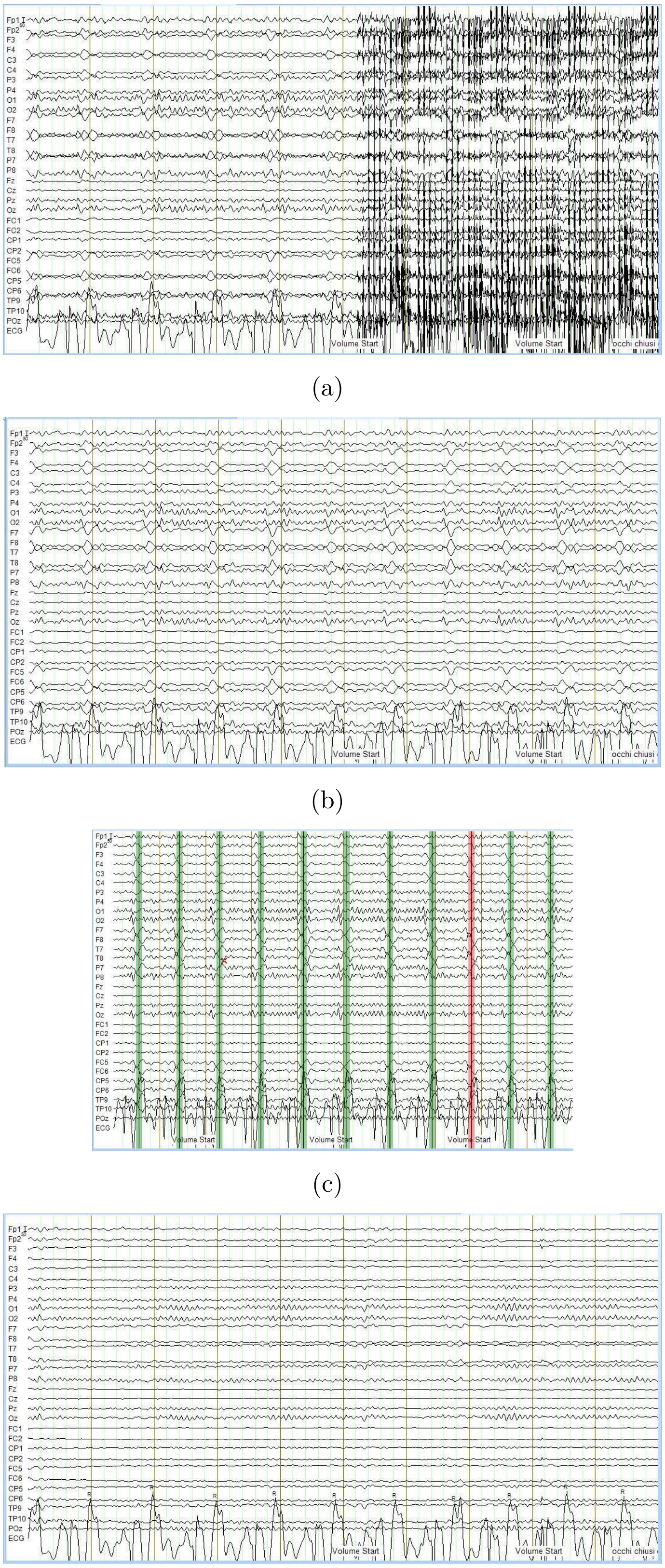

(a)

(b)

(c)

(d)

Figure 2.6: Example of MRI gradient and pulse artefacts correction in EEG traces, performed with the software BrainVision Analyzer 2.0: (a) raw data, (b) after the MR gradient artefact correction, (c) peak detection, (d) after the pulse artefact correction.

less than those caused by natural susceptibility variations in the human head and that therefore do not significantly compromise magnetic resonance image quality.

As for the uniform RF field, the presence of EEG cap may affect its homogeneity reducing image quality by affecting the signal-to-noise ratio and causing local signal loss in EPI data, Figure 2.7. Electrical devices, such as EEG amplifiers, that must be sited close to the subject inside the scanner room can generate RF interference and the effects of this interference on the image depend on its frequency content and on the image sequence. They can anyhow be minimized using fiber-optic cables to transfer data from the EEG amplifiers inside the shielded room to a recording system places outside, with a high degree of RF screening of the EEG amplifier and RF filters. Perturbation of the RF magnetic field can be a major cause of unwanted spatial variation in signal intensity in MR images and of global variation in SNR. If the magnitude of the applied B_1 field varies spatially over the region that is being imaged, unwanted spatial variations of the signal will be produced. Moreover, when materials of high electrical conductivity are exposed to RF, large surface current densities that act to screen the RF field from the interior of the material are generated and these currents also disturb B_1 in regions that are in close proximity to the conductor. The interaction between the RF field and conducting material increases the effective resistance of the RF coil, and as any resistance acts as a source of noise, this effect can lead to a reduction in the SNR of images. Finally, particularly significant disturbance of the RF field can occur if the wires of the EEG cap have a length that is close to an integer multiple of half the RF wavelength, since a standing wave may then be set up in the wire. This resonance can produce a large perturbation of B_1 around the lead, that manifests in artefact and signal loss.

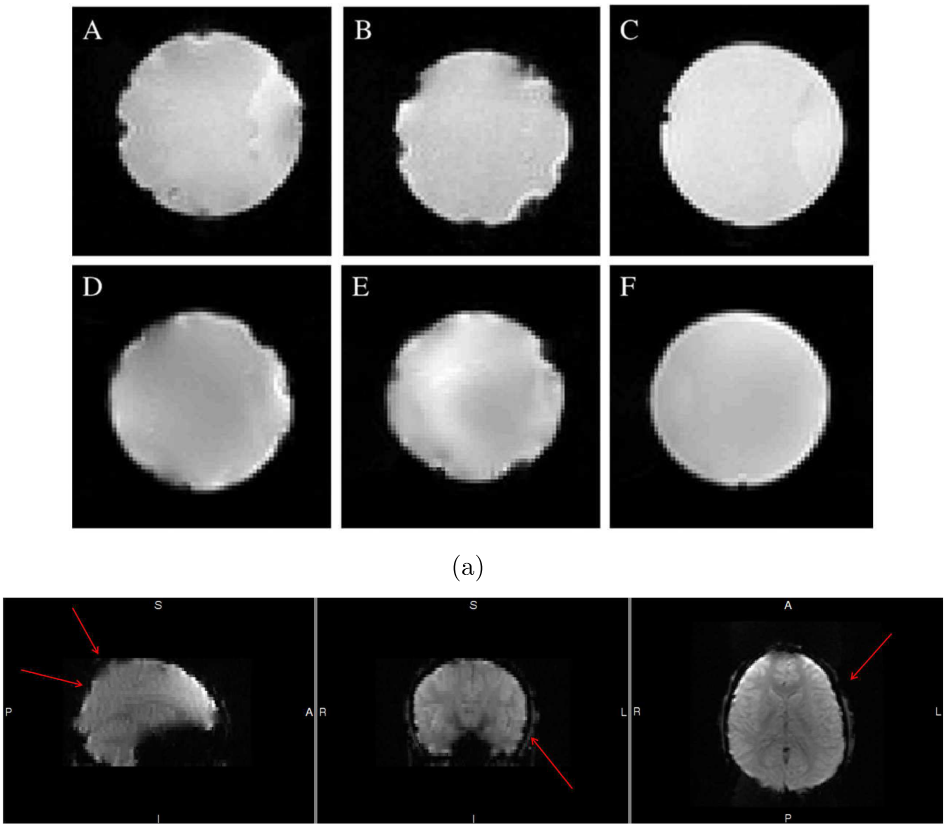

(a)

(b)

Figure 2.7: Examples of EEG-induced artefacts in MR EPI images, (a) in a phantom, [87], (b) and in a healthy subject (data from our archive).

Chapter 3

Parkinson's disease and brain functional connectivity

3.1 Parkinson's disease: a brief overview

Idiopathic Parkinson's disease (PD) is a chronic, progressive and usually sporadic neurodegenerative disorder, [88]. It most commonly affects people $55 - 75$ years old, but it can also develop in younger people. Parkinson's disease is the most common type of parkinsonism (parkinsonism refers to a group of movement disorders that share similar symptoms with PD, but also have unique symptoms of their own).

Parkinson's disease occurs when neurons located in substantia nigra die or become impaired. This brain area is functionally linked to the corpus striatum, gray and white bands of tissue located in both sides of the brain and there the cells release dopamine, an essential neurotransmitter. Loss of dopamine in the corpus striatum is the primary defect in Parkinson's disease. Clinical manifestation of PD develops when almost 80% of dopaminergic neurons in substantia nigra become impaired. Dopamine is one of three major neurotransmitters known as catecholamines: loss of dopamine negatively affects the controlling of movements and coordination, resulting in the main symptoms of Parkinson's disease. Dopamine also appears to be important for efficient information processing, and deficiencies may also be responsible for the cognitive decline that may occur.

Figure 3.1: Brain pathological specimens showing a degeneration of substantia nigra in a Parkinson's disease patient (left) compared to a healthy subject - *source: http://neuropathology-web.org/chapter9/chapter9dPD.html*

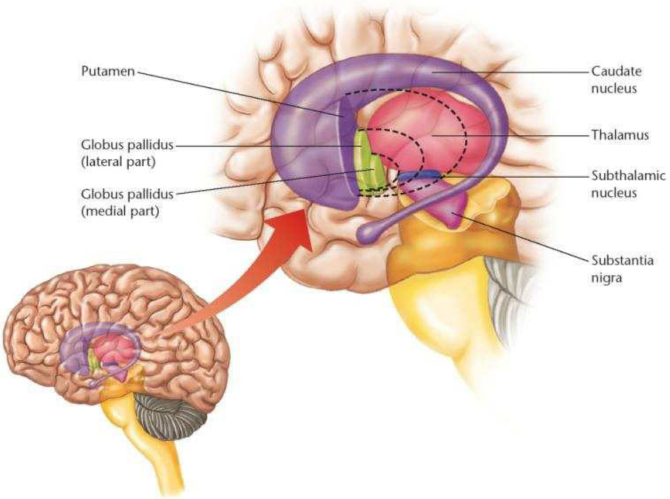

(a)

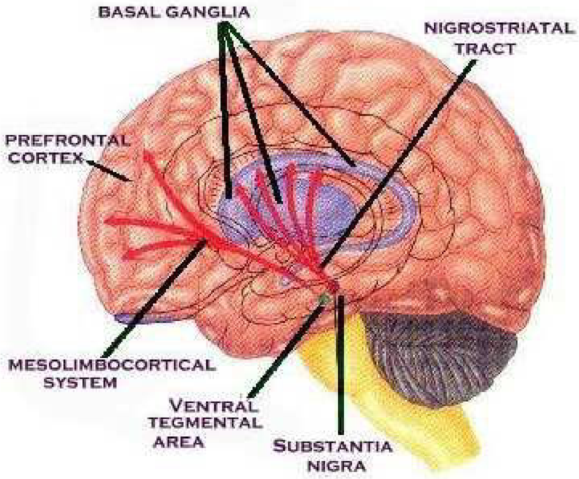

(b)

Figure 3.2: (a): brain structures involved in Parkinson's disease, (b): main dopaminergic tracts

At the present, the precise cause of Parkinson's disease is unknown, i.e. the cause of cells death or impairment in substantia nigra is not known. So far, different theories and hypothesis have been suggested: one theory holds that free radicals - unstable and potentially damaging molecules generated by normal chemical reactions in the body - may contribute to nerve cell death; another one suggests that Parkinson's disease may occur when either an external or an internal toxin selectively destroys dopaminergic neurons; a relatively new theory explores the role of genetic factors in the development of Parkinson's disease. A possible explanation is that a combination of different mechanisms - such as oxidative damage, environmental toxins, genetic predisposition, and accelerated ageing - may ultimately be shown to cause the disease.

The cardinal symptoms and signs are motor (caused by problems in the brain circuits that regulate movement): tremor, that is rhythmic and frequently causes an action of the thumb and fingers known as pill rolling, it occurs when the limb is at rest or when it is held up in a stiff unsupported position and it usually disappears briefly during movement and does not occur during sleep, it can also eventually occur in the head, lips, tongue, and feet; bradykinesia, i.e. slowness of motion, particularly when initiating any movement; stooped posture and a slow, shuffling walk; muscles rigidity. A typical characteristic of the disease is that it has an asymmetrical onset, i.e. at the early stage these symptoms affect exclusively or mainly only one side of the body.

In the advanced phase other deficits and complications may also appear, such as postural instability, cognitive impairment, dementia, autonomic deficits, motor fluctuations/dyskinesia, psychiatric symptoms, swallowing problems (dysphagia), sleep disorder, sensory deficits (decreased sense of smell, vision problems, pain), sexual dysfunction, bowel and bladder complications.

Parkinson's disease can be difficult to diagnose in its early stages and diagnosis remains mostly clinical. No laboratory or imaging tests can diagnose Parkinson's, although brain scans such as computed tomography (CT), magnetic resonance imaging (MRI), or positron-emission tomography (PET/SPECT) may be used to rule out other neurological disorders. Definite diagnosis is only anatomopathological (with specific brain structural lesions), while diagnosis *in vivo* may be only probable or possible, on the basis of a series of inclusion-exclusion-supportive criteria (see UK Parkinson's Disease Society Brain Bank). The diagnosis must periodically be re-examined, as atypical signs may appear forward in time leading to the exclusion of Parkinson's disease by distinguishing it from other diseases, often parkinsonisms.

In a neurological exam, the doctor will ask the patient to sit, stand, walk, and extend his arms. The doctor will observe the patient's balance and coordination. Parkinson's may be suspected in patients who have at least two of the following four symptoms, especially if they are more obvious on one side of the body: tremor (shaking) when the limb is at rest, slowness of movement (bradykinesia), rigidity, stiffness, or increased resistance to movement in the limbs or torso and poor balance (postural instability).

Therapies for PD are just symptomatic and include pharmacological treatments, surgical interventions and physical therapy.

The main pharmacological interventions are represented by dopaminergic therapies. Levodopa, usually combined with carbidopa (a peripheral inhibitor of L-dopa catabolism) is the standard drug treatment. Therapeutic alternatives are represented by dopamine agonists (drugs that mimic the action of dopamine), inhibitors COMT (Catechol-O-methyl transferase), inhibitors MAO (Monoamine Oxidase), amantadine and anticolinergics. Many of these drugs can cause side effects and lose effectiveness over time. Rehabilitation can help patients to improve their balance, mobility, speech, and functional abilities. In some cases of advanced-stage Parkinson's disease, surgery may help to control motor problems; deep brain stimulation is currently the preferred surgical method.

Levodopa, or L-dopa, is the gold standard for treating Parkinson's disease: dopamine agonist drugs mimic dopamine to stimulate the dopamine system in the brain. It increases brain levels of dopamine but its effectiveness tends to decrease after 4 - 5 years of usage. In general L-dopa has the following effects on Parkinson's disease: it is most effective against rigidity and slowness but it produces less benefit on balance impairment and gait disturbances. In many patients, levodopa significantly improves the quality of life for many years. Anyhow taking levodopa has also various side effects, both physical and psychiatric or mental, such as dyskinesia, hypotension, arrhythmia, gastrointestinal effects, effects in the lung, confusion, visual and possibly auditory hallucinations, effects on learning, sleepiness and sleep attacks. Within 4 - 6 years of treatment with levodopa, the effects of the drug in many patients begin to last for shorter periods of time after a dose (called the wearing-off effect). To reduce the effects of fluctuation and the wearing-off effect, it is important to maintain as consistent a level of dopamine as possible.

3.2 Parkinson’s disease and brain connectivity

Parkinson’s disease (PD) patients have difficulty, or inability, to initiate movements (bradikynesia or akinesia), and this has been extensively investigated, but the underlying pathophysiology of this deficit is still unclear, [89]; indeed many studies have been carrying out to get further insights in Parkinson’s disease and in the mechanism that lead to it, in order to improve both diagnosis and therapy.

When the symptoms of PD appear, so at the earlier stage of the disease, the impact on routine structural imaging findings is minimal, therefore structural imaging has in general been unrewarding. Despite the relatively limited structural changes, decline of nigral dopamina neurons has substantial functional effects on cortical-striatal-pallidal-thalamic-cortical circuitry. Functional imaging techniques may therefore shed insights into PD and the basis for its complications. An improved definition of PD related changes in the architecture of functional networks is important for a better understanding of the pathophysiology of the disorder and may help to guide the development of novel therapeutic strategies, [90].

Currently, a large variety of invasive and non-invasive electrophysiological and imaging techniques exists, allowing the description of brain activity during the performance of tasks and of networks in terms of functional connectivity based on the temporal coherence of neural activity on vastly different time scales and spatial resolution.

Electrophysiological data from living humans showed a close association between the occurrence of motor symptoms in PD patients with a pathologically increased oscillatory local field activity in the subthalamic nucleus (STN) and other basal ganglia (BG) nuclei and with increased STN-cortical functional connectivity, primarily in the α- and β-frequency EEG bands. However, non-invasive electrophysiological techniques such as EEG or MEG suffer from poor resolution in subcortical brain areas and are, thus, of limited usefulness for the determination of BG neuronal activity within that certain frequency range. A notable contribution can therefore come from neuroimaging techniques; at the present and in the near future most part of research effort is probably going to be focused on the study of connectivity and brain networks, and this is what we are dealing with here, but also on the automated classification of individual cases leading to machine learning techniques able to assist in clinical diagnosis and on the multimodality approach including molecular imaging.

The first neuroimaging studies, using PET or fMRI, have investigated brain activity in PD patients during performance of movements, mainly self-initiated or self-selected. The common findings of task-related studies are the hypoactivation of the supplementary motor area (SMA) and hyperactivation of some other cortical motor regions, such as the lateral premotor cortex and parietal cortex in PD patients compared to healthy subjects ([91], [92], [93], [94], [95], [96], [97]). Moreover, the connectivity of cortico-cerebellar motor regions is increased in PD patients when performing self-initiated movements. Levodopa or apomorphine administration, ventral posterolateral pallidotomy or deep brain stimulation of the subthalamic nucleus can relatively normalize the hypoactivation of the SMA, and decrease the overactivaton of other cortical areas. The dysfunction of the SMA seems to be an important factor contributing to akinesia in PD. Meanwhile, PD patients may need compensatory activity of other motor circuits to overcome their difficult in performing self-initiated movements.

Abnormal brain activity in PD patients may happen not only while performing movements but also before movements, in the resting state. The first method used to investigate brain activity in the baseline state was transcranial magnetic stimulation (TMS). Decreased cortical facilitation and reduction of intracortical facilitation were observed in PD patients. Only recently fMRI resting state has been applied to investigate brain functional connectivity in PD patients while they were not performing any movements, compared to normal subjects and comparing PD patients before and after the intake of L-dopa. Investigating the interactions of neural networks (interregional connectivity) may provide more valuable information in understanding functional changes than simply investigating regional brain activity.

The main findings are in general modified patterns of connectivity with the primary motor cortex and the SMA, [89]. Comparing PD patients to healthy subjects, a decreased functional connectivity was found in SMA, dorsal lateral prefrontal cortex, putamen ([98]), functional connectivity also decreased between substantia nigra and various other structures, such as striatum, subthalamic nucleus, thalamus, SMA, cerebellum, temporal lobe, default mode network, [99]. An increased connectivity was instead observed in the cerebellum, primary motor cortex, parietal cortex, [98], between subthalamic nucleus and cortical motor areas, [90], and in the associative and limbic connections, [100].

Chapter 4

Materials and Methods

In the present work we dealt with data from EEG-fMRI acquisitions, i.e. they were acquired during simultaneous acquisitions of EEG and fRMI. We just analysed the fMRI data, as for the EEG data analysis a different research group is dealing with. The combination of these two different types of data will be a further, and probably conclusive, step of the whole EEG-fMRI study.

4.1 Hardware for fMRI

Brain fMRI acquisitions were performed using the MR medical scanner in Policlinico S.Orsola: it is an MR medical scanner GE Medical Systems Signa HDx 15 with the characteristics reported in Table 4.1.

magnetic field strength	1.5 T
gradient strength	33mT/m
receiver channels	8 channels
slew rate	276 ms
maximum rise time	120 T/m s

Table 4.1: Technical characteristics of the GE scanner we used for fMRI acquisitions, Figure 4.1(a)

The receiver coil was a 8-channel brain phased array coil GE (1.5T HD 8 Channel High Res Head Array for the GE HDx MR System), see Figure 4.1(b)

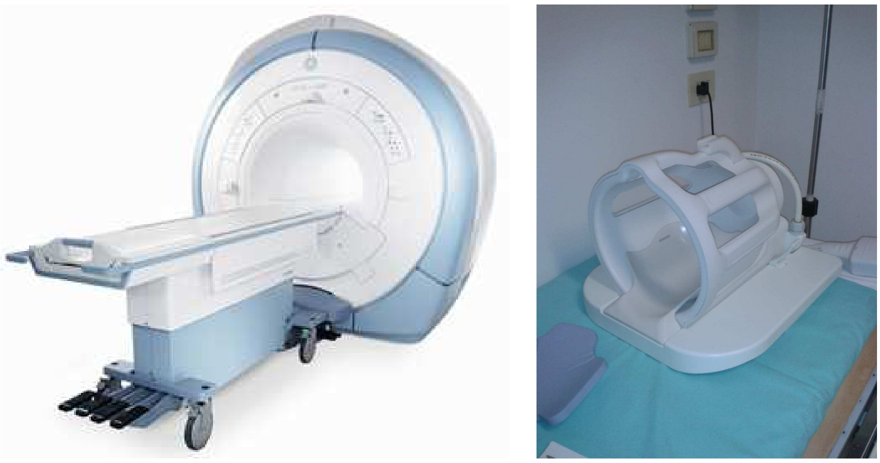

(a) (b)

Figure 4.1: (a) The GE Medical Systems Signa HDx 15 scanner - *source: http://www3.gehealthcare.com/en/Products/Categories/Magnetic_Resonance_Imaging*; (b) The 8 Channel High Res Head Array

4.2 EEG MR-compatible

The equipment used for the EEG measurements was made of the following BrainVision products, which are specific for EEG acquisition inside the MR scanner:

- BrainCap MR (64 channels)
  The design of this cap is optimized for the safety and the comfort of the patient, and to avoid as much as possible artefacts in MR images. Electrodes are pit type sensors placed inside a plastic holder mounted on the cap; they must not touch the skin. The holder is filled with gel to reduce skin conductance and to establish a contact between the sensor and the subject's skin. Every electrode contains safety resistors between the sensor and the connection wire and wires are located on the outside of the cap to ensure isolation between skin and wires. Moreover, all wires are fixed into the cap to avoid loops and high temperature isolating tubes are placed around the ECG electrode cable to avoid contact between skin and wire, Figure 4.2 (a). Electrode holders are as much flat as possible and quite spare, and the cap is made of a soft fabric to increase comfort and to widen the fit to accommodate different head sizes. To reduce image artefacts, the amount of Ag/AgCl in the cap is reduced thanks to the pin sensor design and the number of extra electrodes hanging out of the cap is reduced. Finally, wire outlets for the cable tree at central positions ensure short cable routing distances through the head coil.

- BrainAmp MR
  This device consists of three components: the amplifier, the fiber optic cable and the USB2 Adapter Box, Figure 4.2 (b).

- V-Amp
  This is a digital DC amplifier with 16 unipolar channels and 2 auxiliary channels. It is used as a part of computer-based system for short term registration of the electrophysiological signals, Figure 4.2 (c).

The recording program was BrainVision Recorder and EEG acquisitions were performed with a resolution of $0.1\mu V$ and a sampling frequency of $5kHz$. The software used to analyse the EEG data was BrainVision Analyzer 2.0 (Brain Products GmbH).

(a) (b) (c)

Figure 4.2: BrainVision EEG equipment for fMRI simultaneous registration: (a) BrainCap EEG MR compatible, (b) BrainAmp MR, (c) setup for co-registration inside the MR scanner - source http://www.nitrc.org/project/list_screenshots.php?group _id=587& screenshot_id=490

4.3 Parkinson's disease patients

The patients that underwent this study had been recruited by neurologists Prof. P.Cortelli (IRCSS Istituto delle Scienze Neurologiche di Bologna, DIBINEM, Dipartimento di Scienze Biomediche e Neuromotorie) and Dr. G.Rizzo (DIBINEM) and they had to meet the following criteria.

Inclusion criteria:

- Diagnosis of Parkinson's disease "probable" (at least 3 years of disease)
- Therapy with only L-dopa (other drugs as dopaminergic agents or MAO inhibitors stopped a week before)

Exclusion criteria:

- Moderate-severe rest tremor
- L-dopa induced dyskinesia
- Evidence of gray or white matter abnormalities on conventional MRI (i.e. ischemic lesions)
- Contraindications for MR (e.g. metallic prosthesis, claustrophobia..)

These were quite restricting criteria, therefore it was not so easy to find suitable patients. So far, 8 patients have been recruited, but the data from 2 of them have to be discarded; in one case we obtained very bad fMRI and EEG data due to particularly strong perspiration of the patient and anxiety during the acquisition, that lead to strong movement artefacts and very bad EEG measurement, and in the other case the patient didn't manage to undergo the acquisition until the end of the session due to claustrophobia. Therefore we had 6 patients for which the analyses of EEG and fMRI data were feasible whom clinical data are in table 4.2. We are aware that this is quite a small group (typically, fMRI studies involve at least 10 subjects), indeed the idea is to enlarge it in the next future, anyhow it is sufficient at the moment to define the pipeline, i.e. the various steps of data analysis. At the early stage of the study no healthy controls were contemplated, as its main goal is to compare connectivity patterns before and after the subministration of L-dopa, i.e. patients themselves without assuming L-dopa can be considered as controls. Anyhow, a set of matched (for sex and age) healthy controls is going to be recruited in the next future.

N	Age (yrs)	Sex	Age at onset (yrs)	Side of onset	Disease duration (yrs)	HY stage	UPDRS off	UPDRS on	UPDRS reduction after L-dopa
1	46	F	40	R	6	2	19	9	52.6 %
2	58	M	55	L	3	2	17	6	64.7 %
3	52	F	48	R	4	2	18	10	44.4 %
4	46	M	41	R	5	2	17	8	52.9 %
5	58	M	54	L	4	2	19	10	47.3 %
6	57	M	51	R	6	2	15	10	33.0 %

Table 4.2: The 6 patients acquired so far with suitable data for EEG-fMRI analysis: clinical data (HY: Hoehn and Yahr stating of severity of Parkinson disease, UPDRS: Unifed Parkinson's Disease Rating Scale).

4.4 EEG-fMRI procedure

The experimental EEG-fMRI procedure, to which all the patients were subjected, is the following:

- The patient was examined in the early morning, before the intake of the first daily dose of L-dopa.
- He underwent UPDRS testing (OFF state - without taking L-dopa)
  UPDRS is the Unified Parkinson's Disease Rating Scale, a rating scale useful to quantify clinical symptoms and to follow the longitudinal course of Parkinson's disease. A series of elements are evaluated by interview and clinical observation (evaluation of mentation, behaviour, and mood, self evaluation of the activities of daily life, clinician-scored motor evaluation, Hoehn and Yahr stating of severity of Parkinson disease, Schwab and England ADL scale) and then a

score can be assigned. It is the most commonly used scale in the clinical study of Parkinson's Disease, and it is used by clinicians, neurologist and scientific researcher.

- The EEG cap was placed by neurophysiopathology technicians.
- The patient was positioned in the scanner (using fixed landmarks on the head as reference for position).
- A scout sequence (3 plane localizer) and a calibration sequence (necessary as we used a phased-array coil) were acquired.
- Two runs of rest-BOLD were acquired ($6min45s$ each one): OFF state (details about specific parameters are shown below, in table 4.3, and, simultaneously, the EEG was acquired.
- The patient exited the scanner and took L-dopa ($100mg$).
- The patient was tested clinically every $5-10min$ until the start of the L-dopa effect (mean time $30min$) and UPDRS testing was performed, in ON state. The EEG acquisition continued also outside the MR scanner: at least $15min$ during OFF state and $15min$ during ON state.
- The patient was repositioned in the scanner (using the previous landmarks).
- Two runs of rest-BOLD were acquired ($6min45s$ each one) during the ON state.
- A high resolution 3D structural image was acquired too, during the ON state (lasting $13min$), see table 4.4.

TR	2910 ms
TE	40 ms
flip angle	90°
number of slices per volume	33
number of volumes	130
FOV	24 cm (nv 128)
voxel dimension	1.875x1.875x4 mm

Table 4.3: Resting state BOLD fMRI acquisition parameters

The pulse sequence we used for fRMI was a pure axial EPI (usually, axial slices are actually acquired with reference to anatomical landmarks, but for fMRI acquisition the scanner, as far as switching the gradients is concerned, performs better with pure axial slices). For each acquisition, the first five volumes acquired were rejected (dummy scans), as a steady-state imaging has not yet been reached: it is necessary to allow T_1-related signals to equilibrate. During the acquisition of an entire volume, slices were acquired in an interleaved way, i.e. all the even ones and then all the odd ones $(0, 2, 4, ..., 32, 1, 3, ..., 33)$. The advantage of interleaved acquisition is that it's difficult to perfectly excite one slice without partially exciting neighbouring slices, so doing it interleaved gives time for the overlapping activation to wear off.

A clarification about the TR is necessary: the time needed to acquire each volume and the time that is between two consecutive acquisitions of the same slice (i.e. the time that passes between the start of the acquisition of a volume and the start of the acquisition of the following volume) typically coincide and are indicated as TR (Repetition Time). In our case there is a slightly difference between these two times: the duration of our single volume acquisition is $2.910s$ (during which we acquire the 33 slices) then there are $0.090s$ without gradients activation, i.e. no acquisition, and then the acquisition of the following volume starts; therefore, 3s passes between the start of a volume and the start of the following one, but actual acquisition lasts $2.910s$. The reason for this choice is an easiest interpretation of EEG trace. Taking exactly account of this "inter-volume time" in the further analysis is not possible. For the following analysis we decided to set the TR as $3s$, having a correct information about the time at which each volume was acquired, but assuming that each slice was acquired in $90.91s$ instead of $88.18s$ as it actually was, therefore making an error of about 3%, that we considered acceptable, also considering the preprocessing step of slice-timing correction (see 1.1.3.1).

TR	12.360 ms
TE	5.176 ms
FOV	25.6 cm (nv 256)
voxel dimension	1x1x1 mm

Table 4.4: 3D structural MRI acquisition parameters

4.5 Data analysis

4.5.1 Physiological noise correction

4.5.1.1 ECG measurement

The EEG acquisition system includes the measurement of the ECG trace by means of a specific ECG cable. In EEG the pulse artefact is present (see 2.2.2.1) and measuring the ECG is useful in order to remove the artefact.

The ECG trace is a physiological record that can be used also to remove the cardiac effect (signal fluctuations) in fMRI data. EEG and fMRI acquisition were synchronized, and this is essential for removing methods that need the correspondence between MRI slice acquisition and the cardiac cycle. The drawback is that ECG trace is affected by artefacts too, due to switching gradients and movements of the subject during acquisition.

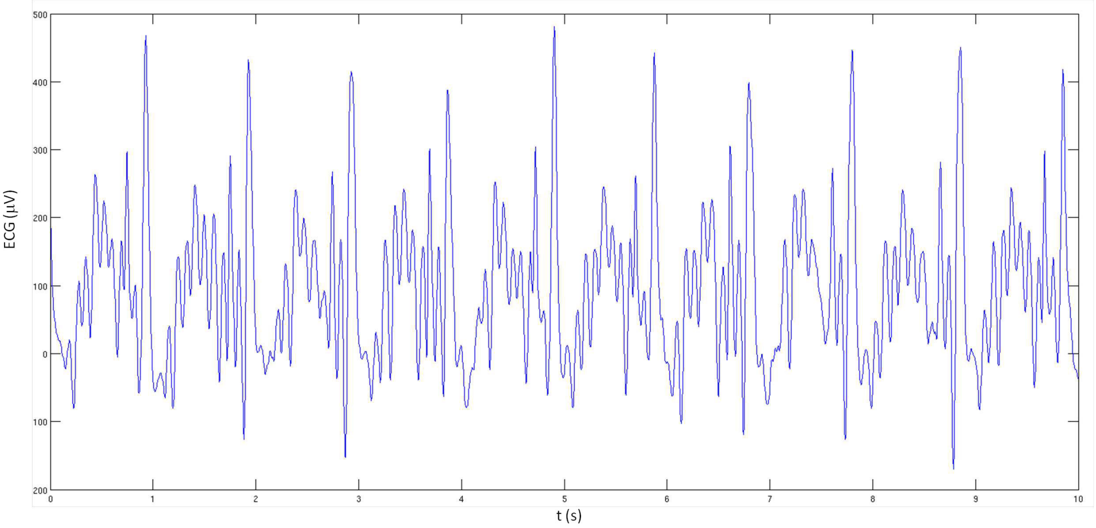

Figure 4.3: Example of our measured ECG (zoom on a temporal window of 10 seconds)

Correction methods are based on the timing of R-wave peaks: they only require the periods to be known (heart beats or peak inspiration), therefore there's no need of the complete trace, it is sufficient to locate the R-peaks, [69]. This was done by using the BrainVision analysis software Analyze 2.0 through an automatic method and a following visual check. Anyhow in some cases managing to identify R-peaks was not so simple. Once we had the time of each R-peak (the zero of the time series is synchronized with the trigger of the MR scanner at the beginning of the first volume acquisition), a synthetic trace was created: value of zero everywhere and five in correspondence of R-peak times.

4.5.1.2 PESTICA

It was not possible to measure respiration during fMRI acquisition due to the unavailability of the suitable instrumentation, but it has been assessed that respiratory effects due to bulk susceptibility changes and movements of the chest during respiration cause magnetic field changes that create a shifting of the brain image during fMRI acquisition (see 1.2.1.2). For respiration and standard echoplanar imaging, the artefact is a phase-encode direction field shift in synchrony with the breathing, that is an anterior/posterior shifting. Even if at 1.5T the effect is probably weak, it make sense to resort to correction methods that don't need physiological recordinds (see 1.2.1.2).

The possibility of regressing out the averaged signal from the whole brain or from specific areas exists, but this is a very controversial procedure, quite common but recently the trend seems to discourage it. We decided to follow this latter approach and therefore we did not use it. Another method may be ICA-denoising, but considering the availability of measured ECG trace it seemed reasonable to use it. Moreover, some studies showed that ICA can identify components in BOLD-weighted data whose principal temporal behaviour is attributable to physiologic noise - either cardiac, respiratory or and unknown combination of these - but there is only indirect evidence that the remaining components are unaffected by physiological noise. ICA performs incomplete separation of sources if there is any spatial or temporal overlap in the components and there may be an undefined number of components related to physiologic noise. Again there isn't an unequivocal view, some groups habitually perform ICA-denoising, while other studies discourage it, [73].

We decided to use a method to obtain an estimation of the respiration effect from the data themselves, with the possibility to use this estimated trace to correct the data by the retrospective method we had decided to use for the cardiac effect (see 4.5.1.3). PESTICA (Physiologic EStimation by Temporal ICA) is a method that uses temporal independent component analysis in order to isolate a direct-sampled estimator of cardiac and respiratory fluctuations, [72]. For some information about ICA in fMRI data, see Appendix A. These estimators accurately represent the periodicity information for the physiologic cycles, similarly to parallel measurement, and then the noise artefact may be removed by a robust methodology such as RETROICOR. It is not assumed that all the variance due to physiologic sources is separated completely into one component, only the assumption that there is a set of slice-wise identifiable components from each volume that has a stable phase representation of the physiologic noise source across the volume is made. Global pattern of voxels containing representations of these signals is general enough to be used in datasets that are statistically independent from the dataset that was used to determine that spatial pattern, [72].

The first step done by Beall et al. was the determination of physiological-related sources within subject (Figure 4.4 (a), method 1 selection). Temporal ICA was performed on each slice independently and a cardiac and a respiratory source (for each slice) were selected by calculating the correlation, $cc(S, C_j)$, between one of these physiological signals ($\vec{S}$, measured during fMRI acquisition) and the time course of each component ($\vec{C_j}$), then the component most likely to contain the variance due to a particular source is assumed to be the one with the maximum absolute correlation.

$$cc(S, C_j) = \frac{\vec{S} \cdot \vec{C_j}}{|\vec{S}||\vec{C_j}|} \tag{4.1}$$

$$|cc(S_{cardiac}, C_{j=cardiac})| = \max(|cc(S_{cardiac}, C_j)|) \tag{4.2}$$

Applying the spatial mixing map of component j (M_j, with the correspondent unmixing matrix W_j, its inverse) to data matrix $\mathbf{Y}$ gives only the temporal source that is represented spatially by the same spatial map in data matrix $\mathbf{X}$

$$C_j^X = W_j^X \mathbf{X} \tag{4.3}$$

$$C_j^Y = W_j^X \mathbf{Y} \tag{4.4}$$

Then the determination of sources-across subject follows. The idea that is at the basis of PESTICA generalized implementation is that for physiologic noise the spatial distribution of the sources of coupling to BOLD signal will be identical for the same subject across scans in the same session and even similar across subjects or different scan sessions. Therefore the hypothesis is that the spatial distribution of a given source can be determined by correlating it in one or few cases with a known signal present in the data, and the relevant spatial map constructed and used to identify the temporal signal of the source in other, statistically independent, scans. The unmixing maps were created from multiple datasets and once that they were realigned to a common spatial basis an average unmixing matrix can be constructed.

$$W^{avg} = \sum_{i}^{scans} W_j^i \tag{4.5}$$

A spatial correlation of the averaged map with an individual spatial map gives the statistic useful in distinguishing the components. The component most likely to contain the variance due to a particular source is found by the index relating to the maximum absolute correlation (Figure 4.4 (b), method 2 selection).

$$cc(W^{avg}, W_j) = \frac{\vec{W^{avg}} \cdot \vec{W_j}}{|\vec{W^{avg}}||\vec{W_j}|} \tag{4.6}$$

$$|cc(W^{avg}_{cardiac}, W_{j=cardiac})| = \max(|cc(W^{avg}_{cardiac}, W_j)|) \tag{4.7}$$

The component timecourse is then the relevant component for the cardiac or respiratory cycle. Once that physiologic sources for all slices are determined, they are ordered by slice acquisition timing to create an estimator for the source.

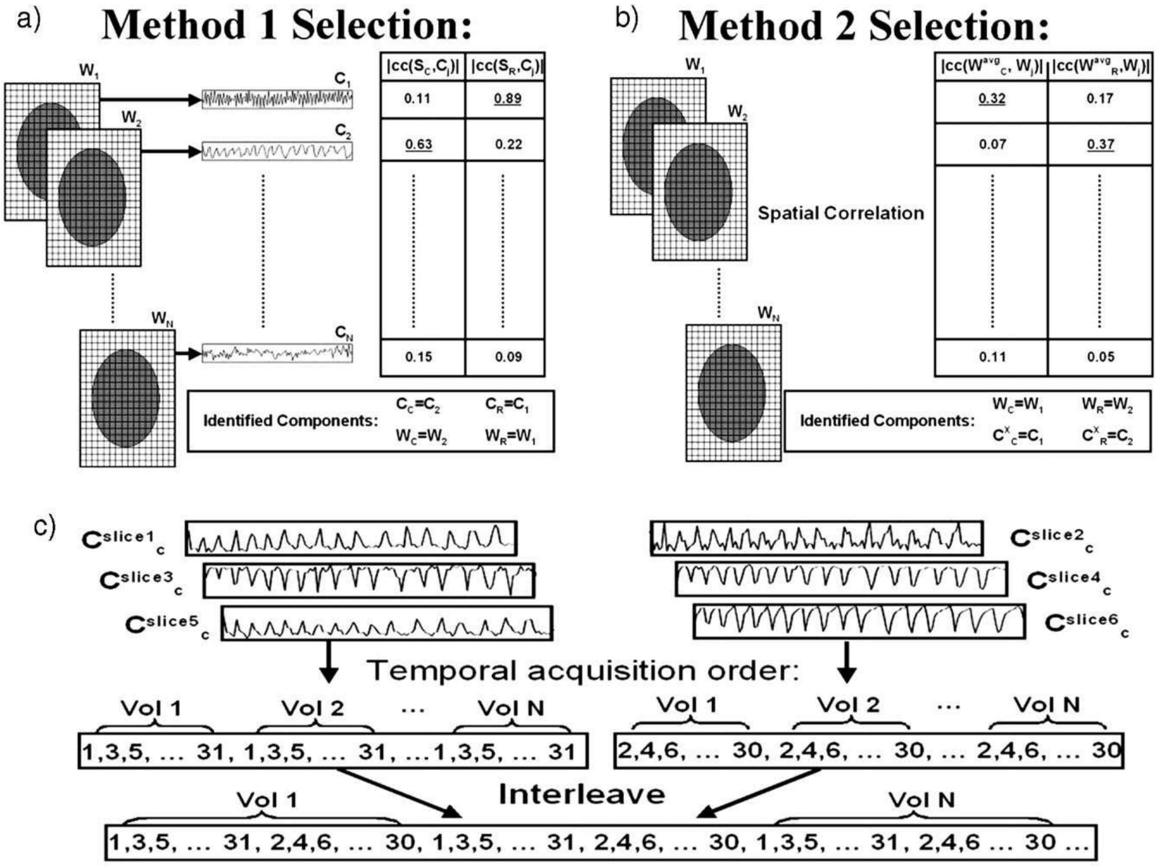

Figure 4.4: PESTICA, diagram of methodology. (a): component selection using temporal correlation of component timecourses with parallel measured physiological data; (b): component selection using spatial correlation between unmixing matrices and a group-averaged spatial unmixing matrix; (c): ordering of selected components into slice-acquisition timing, used by both methods, [72]

Beall et. al [72] in their study collected Dataset 1 (16 subjects, 4 males, age 39.5 ± 8 years) acquiring two fMRI scans for each subject. The first one was used to determine selected components spatial maps then these maps were directly applied to get estimators for the independent second scan of the same subject. Then the same procedure was performed exchanging the scans: the second one is used, along with the associated physiologic measurements, to get the spatial matrix, which is then applied to the former scan. They also collected Dataset 2 (22 subjects, 9 males, age 42.2 ± 10 years) with different TRs and voxel dimensions from Dataset 1 (to study the generality of the method). The respiratory and cardiac unmixing matrices determined from other subjects were transformed in a common space and averaged and then were used to determine the physiologic signal for a given subject. To get a validation of the estimators they compared the estimators with the parallel measured data (temporal correlation), studied the dependence on dimensionality of decomposition (number of components in ICA decomposition), studied the effect of various typical data corrections, comparing the performance of the estimators versus the actual measurements, and explored the dependence on different acquisition parameters. Their results suggest that this is a robust estimation method for determining pulse and respiratory signals from BOLD data without parallel measurement of the physiologic signals.

PESTICA has been implemented with AFNI (Analysis of Functional NeuroImages, *afni.nimh.nih.gov*) and MATLAB and it is available as open-source software. It runs on data in the AFNI image format (i.e. .BRIK and .HEAD) and, as PESTICA instructions and directly professor Beall suggested, we run PESTICA on almost raw data: no pre-processing step was done, a part from motion correction (preformed with *3dVolReg*, volume registration function in AFNI, [101]).

As we did not measure directly respiration, it seemed hazardous to calculate the RVT (Respiratory Volume per Time, according to what suggested in [58], [59]) and adding it as a confounding regressor.

4.5.1.3 RETROICOR

We decided to correct the physiological noise in our data by means of the robust and wide-used retrospective method RETROICOR (RETROspective Image-based CORrection).

It is a retrospective correction technique similar to the method of Hu et al. [68], but if the method proposed by Hu et al. operates in the k-space, RETROICOR operates in the image domain. The retrospective correction proposed by Hu et al. fits a low-order Fourier series to the k-space time-series data based on the phase of the respiratory or cardiac cycle during each acquisition. The main drawbacks are that only the data near the k-space origin have adequate SNR for the Fourier fit to be robust and thus only low-order spatial corrections can be made, this, in turn, introduces correlations between pixels in the correction. Image-based correction provides advantages: spatial-frequency filtering is not imposed on the correction and therefore it functions equally well for both global and localized noise. RETROICOR allows to correct the data apart from performing a statistical analysis, anyhow it is also possible to add parameters obtained from RETROICOR as confounding to be regressed out in the general linear model. This method requires that cardiac and respiratory states are monitored during MRI acquisition. The initial assumption is that the time series of intensities $y(t)$ in a voxel is corrupted by additive noise resulting from cardiac and respiratory functions, [69]. Physiological processes are assumed to be quasi-periodic so that it is possible to assign unique cardiac and respiratory phases to each image (i.e. slice) in the time series. The physiological component of the signal is modelled with a low-order Fourier series expanded in terms of these phases.

$$y_\delta(t) = \sum_{m=1}^{M} [a_m^c \cos(m\phi_c) + b_m^c \sin(m\phi_c) + a_m^r \cos(m\phi_r) + b_m^r \sin(m\phi_r)] \tag{4.8}$$

Preliminary studies showed that including terms of higher order than 2 leads to little gain, so $M = 2$ is typically used. Once that equation 4.8 is evaluated, the data are corrected by subtracting $y_\delta(t)$ from $y(t)$.

The phases follows the definitions given by Hu. The cardiac phase is defined as

$$\phi_c(t) = 2\pi \frac{t - t_1}{t_2 - t_1} \tag{4.9}$$

where t_1 is the time of the R-wave peak in the cardiac cycle just preceding t, and t_2 is the time for the subsequent R-wave peak. Cardiac phase advances linearly from 0 to 2π during each R-R interval and is reset to 0 for the next cycle. The idea is that the cardiac effect on fMRI data depends on when each slice was acquired within the cardiac cycle.

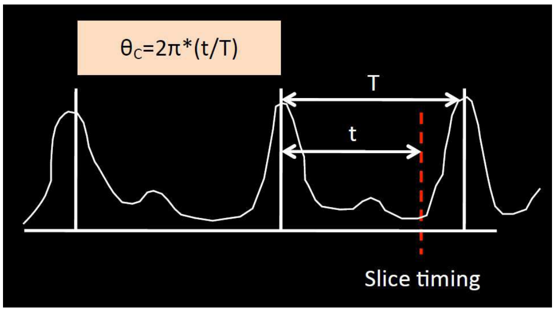

Figure 4.5: Schematic representation of how the cardiac phase is calculated, [102].

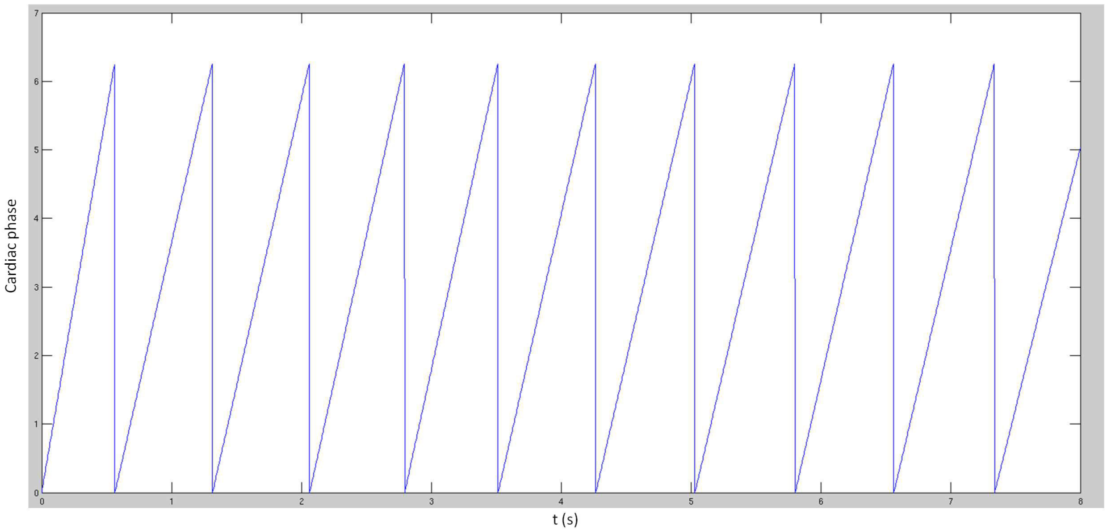

Figure 4.6: Example of cardiac phase (zoom on 8 s)

The definition of the respiratory phase is slightly more complex as the NMR shift that result from magnetic field variation, as well as any bulk motion of the head from respiration, depends on the depth of the breathing cycle, i.e. the amplitude of the respiration cycle should also be accounted for. A histogram-equalized transfer function is generated between respiratory amplitude and ϕ_{resp}. The amplitude of respiratory signal $R(t)$ is normalized to the range $(0, R_{max})$, a histogram $H(b)$ is obtained as the number of occurrences H of respiratory values during the scan at bin value b, where 100 bins are chosen to span the range, and therefore the b-th bin is centred at $bR_{max}/100$. End-expiration is assigned a phase of zero and peak inspiration has a phase of $\pm\pi$, while inhaling $(dR/dt > 0)$ the phase spans 0 to π, during expiration $(dR/dt < 0)$ the phase is negated. Transfer function that relates $\phi_{resp}(t)$ to $R(t)$ is

$$\phi_r(t) = \pi \frac{\sum_{b=1}^{rnd[\frac{R(t)}{R_{max}}]} H(b)}{\sum_{b=1}^{100} H(b)} sgn\left(\frac{dR}{dt}\right) \tag{4.10}$$

where $rnd()$ is denotes an integer-rounding operation (e.g. 0.82 rounded to 82).

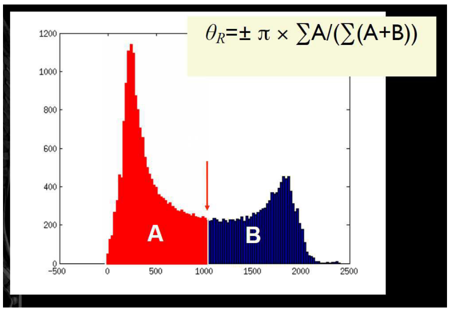

Figure 4.7: Schematic representation of how the respiratory phase is calculated, [102].

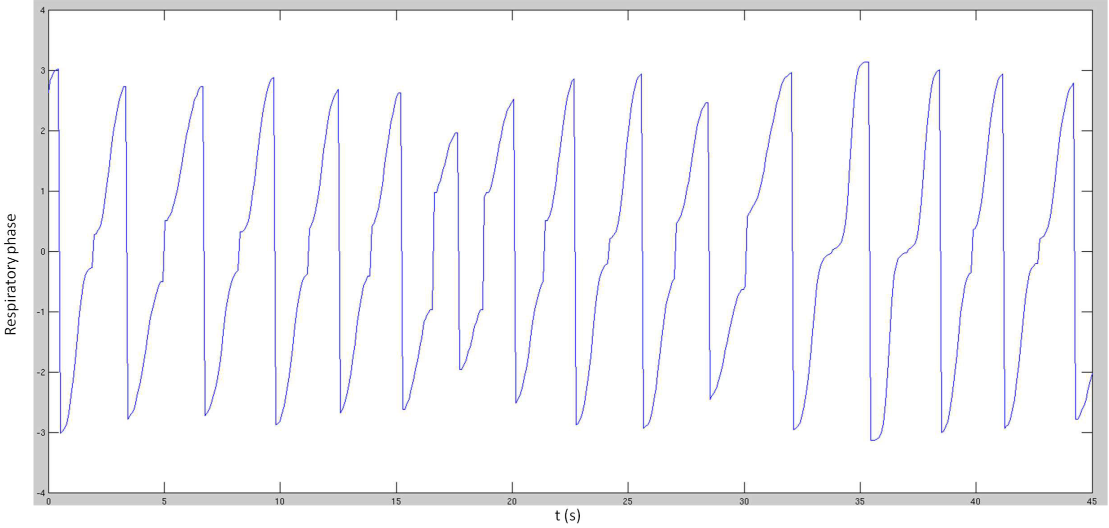

Figure 4.8: Example of respiratory phase (zoom on 8 s)

The coefficients a and b are obtained for every voxel by a Fourier summation over all time points t_n, see equations 4.11 and 4.12.

$$a_m^x = \frac{\sum_{n=1}^{N}[y(t_n) - \bar{y}]cos(m\phi_x(t_n))}{\sum_{n=1}^{N} cos^2(m\phi_x(t_n))} \tag{4.11}$$

$$b_m^x = \frac{\sum_{n=1}^{N}[y(t_n) - \bar{y}]sin(m\phi_x(t_n))}{\sum_{n=1}^{N} sin^2(m\phi_x(t_n))} \tag{4.12}$$

where $\bar{y}$ denotes the average of y over the time series, and x means either cardiac or respiratory.

We used the RETROICOR implementation made in the AFNI function *3dretroicor*, that follows the original method described above, according to Glover study and without any further modification.

The input data to *3dretroicor* are raw fMRI data in the AFNI image format, with no preprocessing done on them. Whether volume registration may be useful or not before RETROICOR is a controversial issue, and there are contrasting approaches; a study proposed a modified version of RETROICOR to take into account of volume registration performed previously, and found better results on simulated data but really slightly effects on real data, [103]. It is important that the information about slice timing acquisition (slice offset) is present and readable in the image header. Data acquired from the scanner were saved in the DICOM format (Digital Imaging and COmminications in Medicine) and then converted into AFNI format with the function *to3d*; after that PESTICA and 3dretroicor correction had been performed, data were converted into NIfTI (Neuroimaging Informatics Technology Initiative, *nifti.nimh.nih.gov*) format (with the function *3dAFNItoNIFTI*) as it is the format FSL - the software we used for further analyses - deals with. Due to a different dealing of orientation, also applying the functions *fslswapdim* and *fslorient* was necessary to get the right orientation of images and to have data usable in FSL.

A useful measure of image time course stability is the temporal signal-to-noise ratio (TSNR) calculated by dividing the mean of a time series by its standard deviation, [104]. To have an idea of the correction performed with *3dretroicor* we computed TSNR percentage difference between data after and before the correction, as it is useful to quantify the influence of each physiological noise correction on the voxel's time series. TSNR is defined as:

$$TSNR = \frac{mean(y(t))}{sqrt(y(t))} \tag{4.13}$$

It is an important characteristic of fMRI time courses, that depends on fMRI acquisition parameters, tissue type and the amount of physiological noise. In the context of MRI, signal-to-noise ratio (SNR) reflects static or single image MRI signal strength over the noise present in the absence of signal. However, it does not provide insight into the temporal noise characteristics of fMRI time courses.

In order to average the maps relative to different subjects, registering them to a common space was necessary; the common procedure consists of registering fMRI data to the high-resolution structural image, registering the structural image to the standard, and then registering fMRI data to the standard. In order to register images to a common space minimizing the registration errors and using only a type of image (functional EPI), we tried a relative new approach (at least in fMRI context): the creation of a study specific template, a quite diffused procedure for example for VBM (Voxel Based Morphometry) studies. We used one volume of functional data from different EEG-fMRI acquisitions performed in our department, for a total of 24 images. After pre-processing steps (re-sampling to isotropic voxels and registration to a volume of reference, one of the 24, through linear registration with flirt, [105], [106]) the average of the various images was performed with the registration tool Dartel (Diffeomorphic Anatomical Registration Through Exponentiated Lie Algebra) of SPM8, [107]. TSNR maps were then registered to the template with Dartel, using the flow field (i.e. a sort of non linear registration map) previously computed for each subject volume and it was then possible to average them together. For the contextual purpose of averaging maps together, this kind of study specific template is enough. If the information of a standard space (for example atlases information) are needed, the study specific template should be registered itself to the standard space. Even if not strictly necessary here, we registered it to the MNI space with a linear registration (with flirt, [105], [106]). This approach is not so widespread yet, in the literature there's just a recent preliminary study testing the efficiency of a study specific template with BOLD data, [108]. However it seems promising and may help to improve registration of functional image, which is often problematic due to their lack of contrast and details.

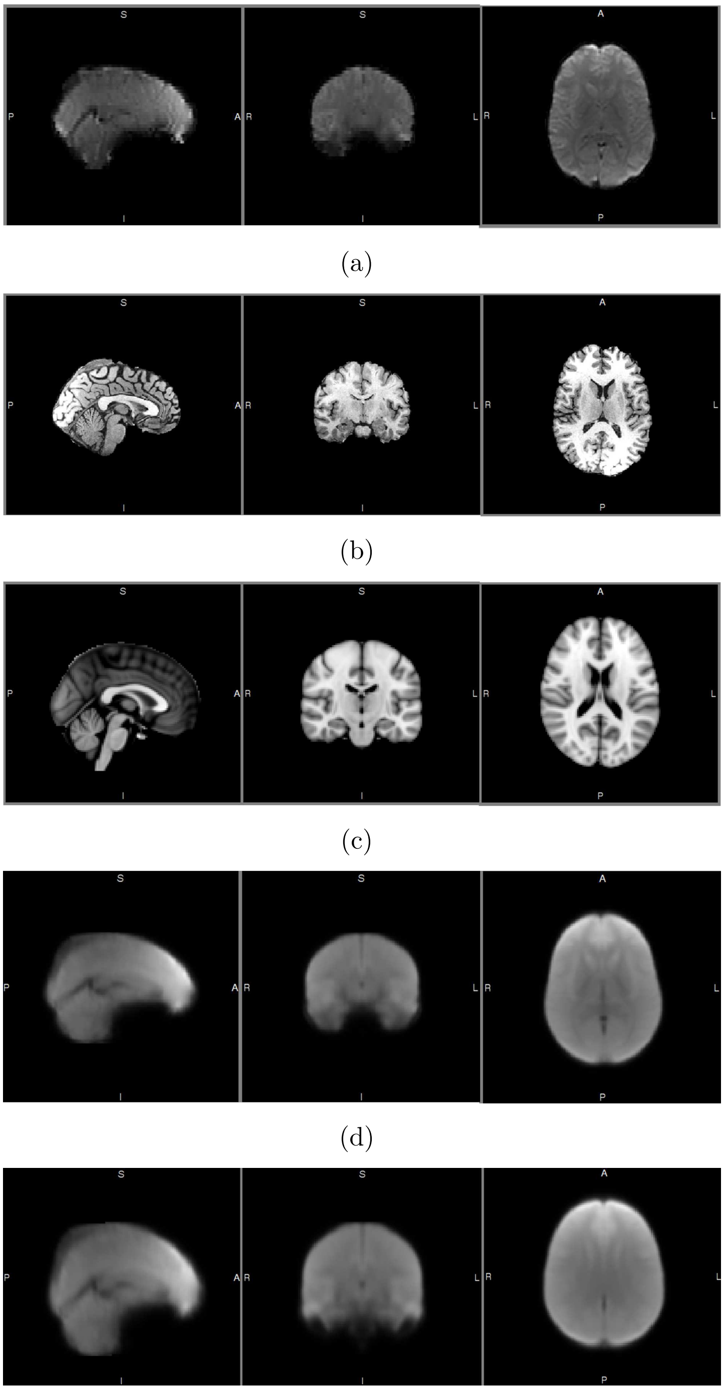

(a)

(b)

(c)

(d)

(e)

Figure 4.9: Examples of a brain MR slice from (a) a functional volume, (b) structural 3D, (c) standard MNI space, (d) our study specific template (e) our study specific template registered to the MNI.

4.5.2 Seed-based connectivity

Connectivity analyses based on techniques such as ICA or graph-theory give information about the global pattern of brain connectivity, instead we are more interested in the functional connectivity of specific region within the motor circuits, therefore we opted for the seed-based approach.

Parkinson's disease patients have difficulty in initiating movements (akinesia) and extensive neuroimaging studies have investigated brain activity during performance of self-initiated or self-selected movements. The common findings of these studies are the hypoactivation of the supplementary motor area (SMA), and hyperactivation of some other cortical motor regions, like the lateral premotor cortex (PMC), and parietal cortex in PD patients compared to normal subjects ([91], [92], [93], [94], [95], [96], [97]). PD patients may need compensatory activity of other motor circuits to overcome their difficulty in performing self-initiated movements [89]. It was showed that levodopa or apomorphine administration or deep brain stimulation can relatively normalize the patterns of activation ([91], [92], [109], [110]). Abnormal brain activity may happen not only during performance of movements but also in the resting state, and this is the situation we investigated.

The regions of interest we chose are the supplementary motor area - SMA (right and left) and the precentral gyrus (right and left) (M1 - primary motor area); SMA is critical in initiating movements, while bilateral M1 are critical in motor execution. The seeds were drawn manually by a neurologist in the MNI space, as spheres centred in the coordinates reported in table 4.5 and with a radius of $5mm$ (see Figure 4.10). To extract the average time-series within these areas we used the tools of the software FSL ([111], [112]) and performed the following steps:

- Inversion of the transformation matrix from fMRI space to MNI space, using the command-line program *convert_xfm* (in a preliminary analysis, linear registration of fMRI data to the standard space MNI have been performed for each run of each subject, storing the transformation matrix, that therefore can be inverted and used to register from MNI space to fMRI space of that specific run).
- Registration of ROIs drawn in MNI space to fMRI run-specific space, by applying the just calculated inverted matrix, using the tool flirt ([106], [105]).
- Extrapolation of the time series within the ROIs in the fMRI space, averaging the time series of all the voxels included in each ROI, by using the FSLUTILS command-line utility *fslmeants.*

At the end of this procedure (implemented in a bash script that automatically runs it for the four runs of each patient) for each run of each patient we have a text file for each seed with the temporal trend of the signal within that seed (averaged over the various voxels that constitute the ROI) and it will be used in the following analysis within the GLM.

seed	x	y	z
precentral gyrus (R)	23 (44.00)	59 (-8.00)	55 (38.00)
precentral gyrus (L)	67 (-44.00)	59 (-8.00)	55 (38.00)
SMA (R)	42 (6.00)	63 (0.00)	63 (54.00)
SMA (L)	48 (-6.00)	63 (0.00)	63 (54.00)

Table 4.5: Coordinates (in MNI standard space, voxels (mm)) of spherical seed's centres.

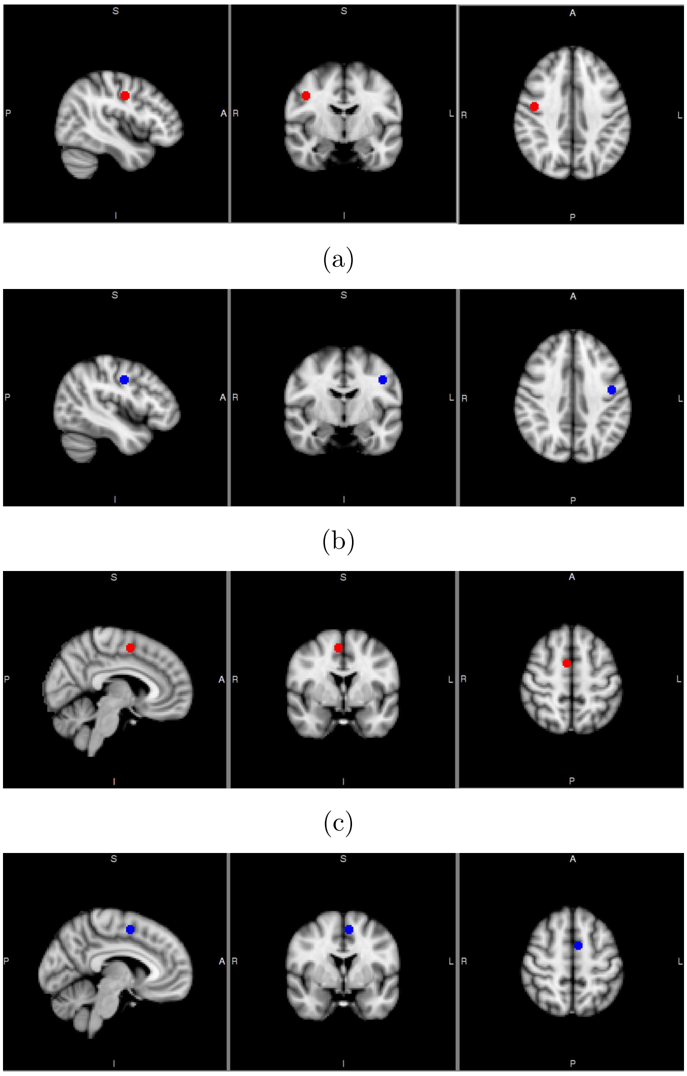

(a)

(b)

(c)

(d)

Figure 4.10: Seeds drawn on the standard space: (a) precentral gyrus, right; (b) precentral gyrus, left; (c) SMA, right; (d) SMA, left.

4.5.3 General linear model

We performed fMRI data analysis by using FEAT, a software tool for high quality model-based fMRI data analysis, with an easy-to-use graphical user interface, part of FSL (FMRIB's Software Library, [111] [112] [113] [114]). We run First-level analysis (Full analysis) for analysing each session's data - i.e. the time-series analysis of the raw 4D FMRI data.

The input data were fMRI 4D data (already corrected as far as physiological, i.e. cardiac and respiratory, noise is concerned). The high pass filter cut off was set at $100s$, and the same filter was applied to the model as to the data. We set up our TR of $3s$ (for more details about this value see 4.4) The motion correction (with MCFLIRT) and the slice timing correction (interleaved) were applied. The brain extraction (with BET) was set up and a spatial smoothing was performed with a Gaussian filter of FWHM $6mm$. FILM prewhitening was used (it is suggested for typical first-level time series analysis to make the statistics valid and maximally efficient; it accounts for temporal autocorrelation when assessing changes within voxels as it estimates autocorrelations and removes them, to get good linear unbiased estimators) and motion parametrs were added to the model (head motion parameter estimated by MCFLIRT are added as confounding EVs in the model, this may help to remove residual effect of motion. The best and univocal approach is not well defined yet: some groups suggest to use ICA-based denoising, other ones habitually add motion parameters to the model.)

As for the full model setup, we had one custom EV with one entry per volume (it was the file text containing averaged time series of seed), none convolution was performed (as the waveform was sampled from the data itself) and we set up two contrasts (1, -1) to consider both activations and deactivations.

A thresholding cluster analysis was performed, with a z-threshold of 2.3 and a cluster probability of 0.05. The z-statistic threshold was used to define contiguous clusters, then each cluster's estimated significance level (from Gaussian Random Field theory) was compared with the cluster probability threshold and the significant clusters were then used to mask the original z-statistic image.

The main high-resolution structural image to which low-resolution functional data are registered (with a linear registration, 6 DOF) was the structural 3D acquired for each patient.

As standard space we used MNI_152_T1_2mm (and the registration was nonlinear, with a warp resolution of $10mm$). We chose a non linear registration between the 3D and the standard space because one of our patients has quite large ventricles and a registration that does not allow deformation did not give good results.

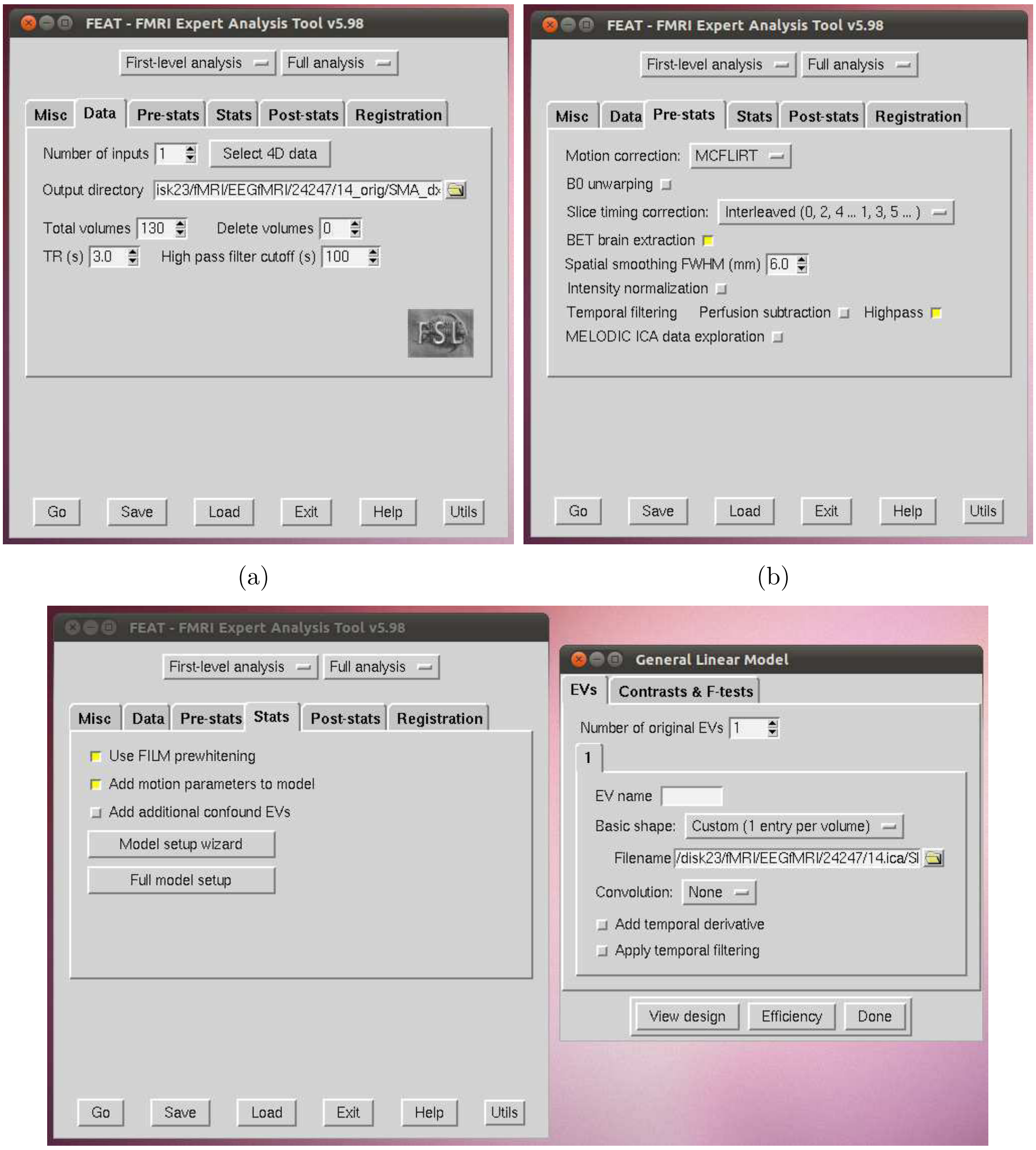

Number of inputs 1

Output directory isk23/fMRI/EEGfMRI/24247/14_orig/SMA_dx

Total volumes 130 Delete volumes 0

TR (s) 3.0 High pass filter cutoff (s) 100

(a)

Motion correction: MCFLIRT

B0 unwarping ☐

Slice timing correction: Interleaved (0, 2, 4 ... 1, 3, 5 ...)

BET brain extraction ☑

Spatial smoothing FWHM (mm) 6.0

Intensity normalization ☐

Temporal filtering Perfusion subtraction ☐ Highpass ☑

MELODIC ICA data exploration ☐

(b)

☑ Use FILM prewhitening

☑ Add motion parameters to model

☐ Add additional confound EVs

Number of original EVs 1

EV name

Basic shape: Custom (1 entry per volume)

Filename /disk23/fMRI/EEGfMRI/24247/14.ica/Sl

Convolution: None

☐ Add temporal derivative

☐ Apply temporal filtering

(c)

Figure 4.11: Feat GUI First-level analysis; (a): input data, (b): pre-stats, (c): stats.

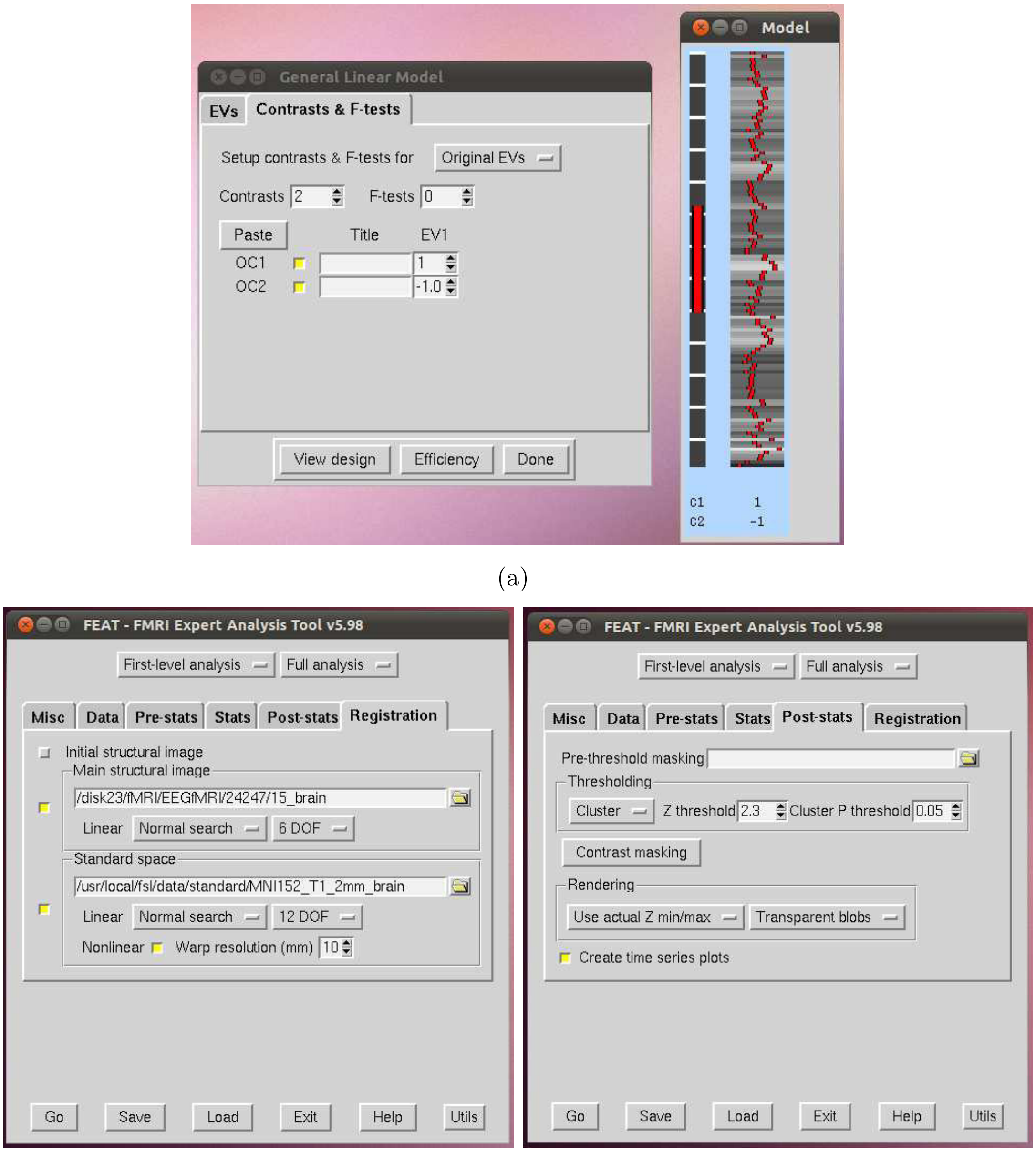

Setup contrasts & F-tests for Original EVs

Contrasts 2 F-tests 0

		Title	EV1
OC1	☑		1
OC2	☑		-1.0

c1 1
c2 -1

(a)

First-level analysis Full analysis

☐ Initial structural image

Main structural image
☑ /disk23/fMRI/EEGfMRI/24247/15_brain
Linear Normal search 6 DOF

Standard space
☑ /usr/local/fsl/data/standard/MNI152_T1_2mm_brain
Linear Normal search 12 DOF
Nonlinear ☑ Warp resolution (mm) 10

(b)

First-level analysis Full analysis

Pre-threshold masking

Thresholding
Cluster Z threshold 2.3 Cluster P threshold 0.05

Contrast masking

Rendering
Use actual Z min/max Transparent blobs

☑ Create time series plots

(c)

Figure 4.12: Feat GUI First-level analysis; (a): GLM desing, (b): registration, (c): post-stats.

4.5.4 Group analysis

Group statistic was performed once fMRI data had been analysed individually (each run), it is the analysis across subjects, and it is called higher-level analysis in Feat.

FEAT offers both fixed-effects and mixed-effects higher-level modelling: we chose a mixed-effects regression model in order to model the subject variability and to have the possibility to make inference about the wider population from which the subjects were drawn. A Paired Two-Group Difference (Two-Sample Paired T-Test) was performed to compare two groups of data and to find out if means were significantly different from one another or if they were relatively the same. In our case, we compared, for the same subjects, activations and deactivations in the connectivity with each of the four seeds, before (OFF state) and after (ON state) the assumption of L-dopa. Therefore the test was paired since we compare groups that were related as participants in the first group are the same as participants in the second group. There were two copes, i.e. two contrast of parameter estimates (activation and deactivation); for each voxel, the parameter estimate was the regression coefficient that resulted from regressing the intensity time-series on the model. Finally, the z-statistic image was thresholded and underwent a clustering analysis, analogous to the one described in 4.5.3. We took account of both OFF runs and both ON runs of each patient (it's resting state so differences between the two runs are not expected). The contrasts, i.e. the differences, were performed both for OFF versus ON and ON versus OFF; we were mainly interested in the latter, i.e. in activations (or deactivations) that were present in the ON state (after L-dopa) but not in the OFF state (before L-dopa).

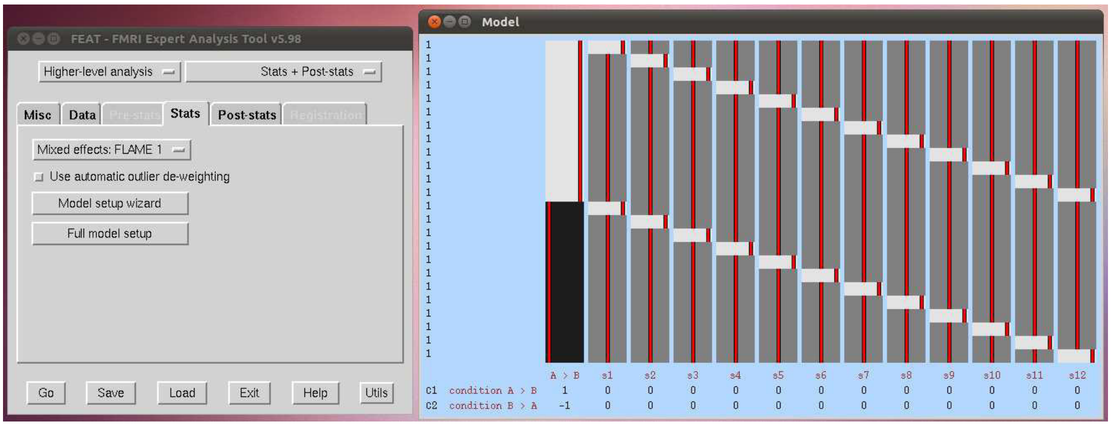

Higher-level analysis
Stats + Post-stats
Mixed effects: FLAME 1
☐ Use automatic outlier de-weighting

		A > B	s1	s2	s3	s4	s5	s6	s7	s8	s9	s10	s11	s12
C1	condition A > B	1	0	0	0	0	0	0	0	0	0	0	0	0
C2	condition B > A	-1	0	0	0	0	0	0	0	0	0	0	0	0

Figure 4.13: Feat GUI Higher-level analysis: paired two-group difference model design

Chapter 5

Results

5.1 Physiological noise correction

Physiological correction was performed using two software packages: RETROICOR (see 4.5.1.3), for cardiac noise, by using the ECG measured contextually with the EEG (see 4.5.1.1), and PESTICA estimation for respiratory noise (see 4.5.1.2). In order to quantify our correction, and to have an idea of brain areas in which it was more effective, we computed TSNR (see 4.5.1.3) percentage variation maps between data before and after the correction, therefore a higher positive value of TSNR percentage variation in a given voxel means that in that voxel a higher correction was performed. To average TSNR maps together, they were all registered to the study specific template we created (see 4.5.1.3), and then they were also registered to the MNI standard space. As far as the cardiac noise correction is concerned, Figure 5.1 shows all the axial views of the TSNR percentage variation map, averaged over 6 subjects, superimposed onto the study specific template, while in Figure 5.2 they are superimposed onto the MNI template (showing additional non-brain structures). In Figure 5.3 there are some orthographic views of the same map and in Figure 5.4 the same views as in Figure 5.3 but relative to just one subject. For the respiratory noise correction analogous images are displayed: in Figure 5.5 all the axial views of the TSNR percentage variation map, averaged over 6 subjects, superimposed onto the study specific template, in Figure 5.6 they are superimposed onto the MNI template (showing additional non-brain structures), in Figure 5.7 the same map but shown in various orthographic views and in Figure 5.8 the same orthographic views for one subject. The results for a single subject are consistent with the averaged results, and the comparison between Figures 5.3 and 5.4, and between 5.7 and 5.8 are an example of this. All the axial views and some orthographic views are also shown, respectively in Figure 5.9 and 5.10, for the combination of cardiac and respiratory correction. In the Figures displaying the TSNR percentage variation maps we showed only variations between 5% (or 3%) and 20% (or 10%) in order to focus attention on the areas on which the correction had a higher effect; anyhow small percentage variations were present also in other voxels. We also computed (with the AFNI function *3dttest*) maps of t-statistics values for % TSNR changes after the application of RETROICOR, with respect to 0% level (see Figures 5.11, 5.12, 5.13, 5.14, 5.15, 5.16). They are thresholded at t values corresponding to $p < 0.01$ after multiple comparison correction (for all voxels) was performed with the FDR (False Discovery Rate) method. Higher levels of significance are noticeable in the areas where the correction was more effective, and that also small variations (of a few percent) of TSNR were significant, especially when both corrections (cardiac and respiratory, Figure 5.15) were performed.

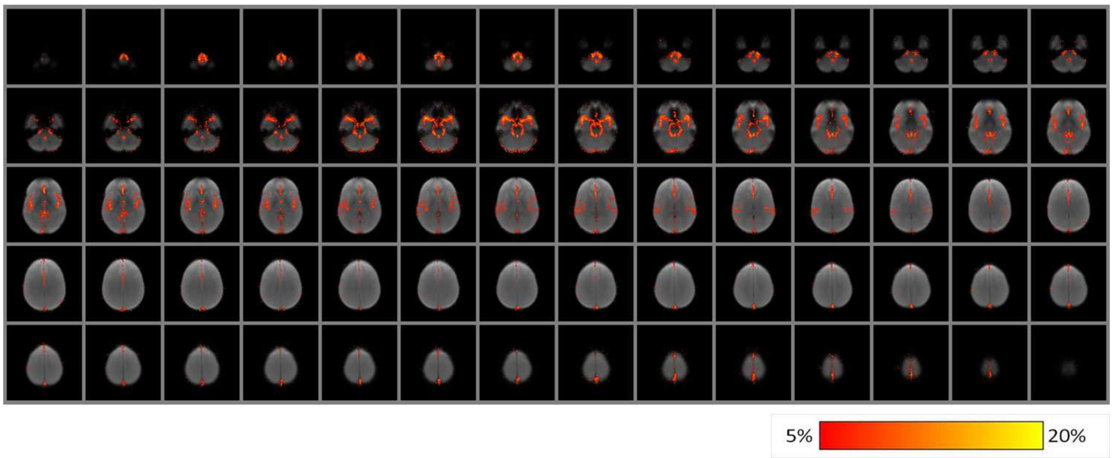

Figure 5.1: TSNR map (percentage variation) for cardiac noise correction: mean across 6 subjects, axial views. The map is superimposed onto the study specific template, to which single maps were registered.

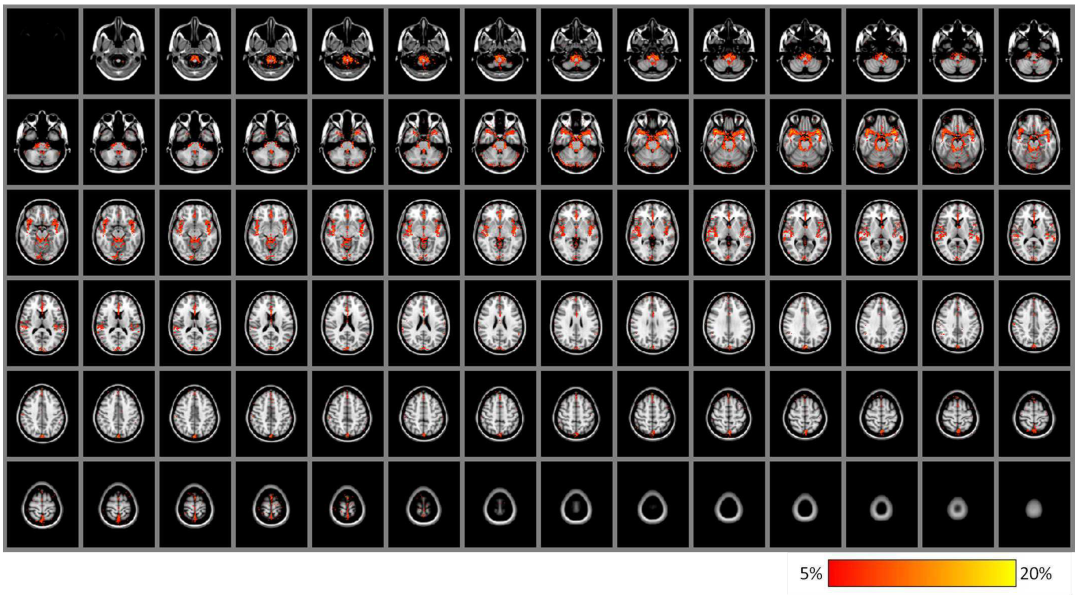

Figure 5.2: TSNR map (percentage variation) for cardiac noise correction: mean across 6 subjects, axial views. The map is superimposed onto the MNI standard template, to which it was registered.

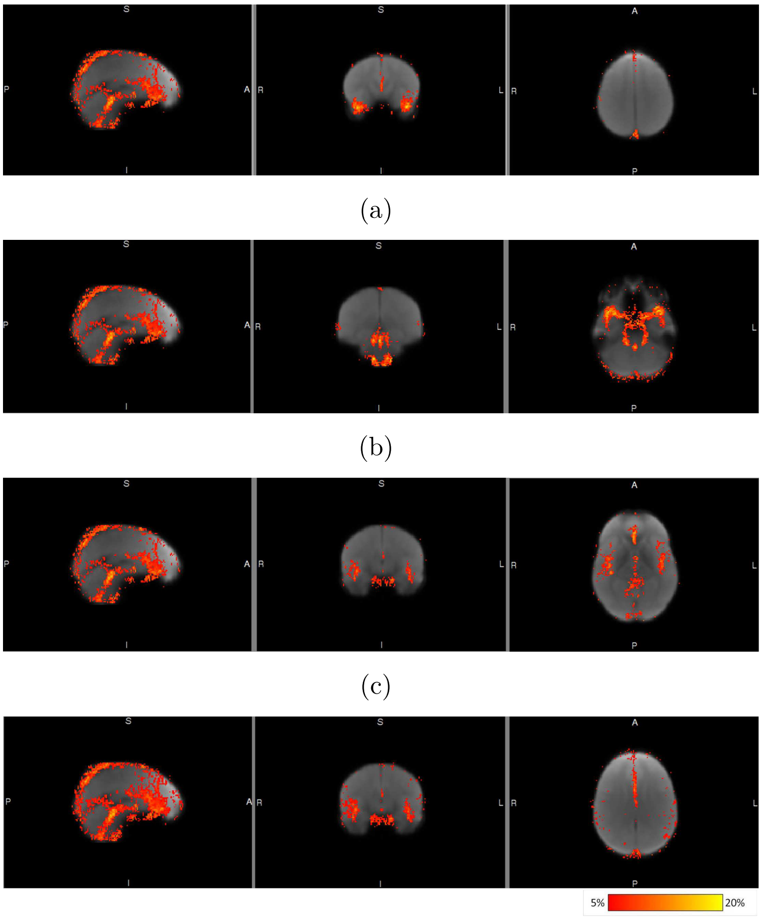

(a)

(b)

(c)

(d)

Figure 5.3: TSNR map (percentage variation) for cardiac noise correction: mean across 6 subjects, some orthographic views. The map is superimposed onto the study specific template, to which single maps were registered.

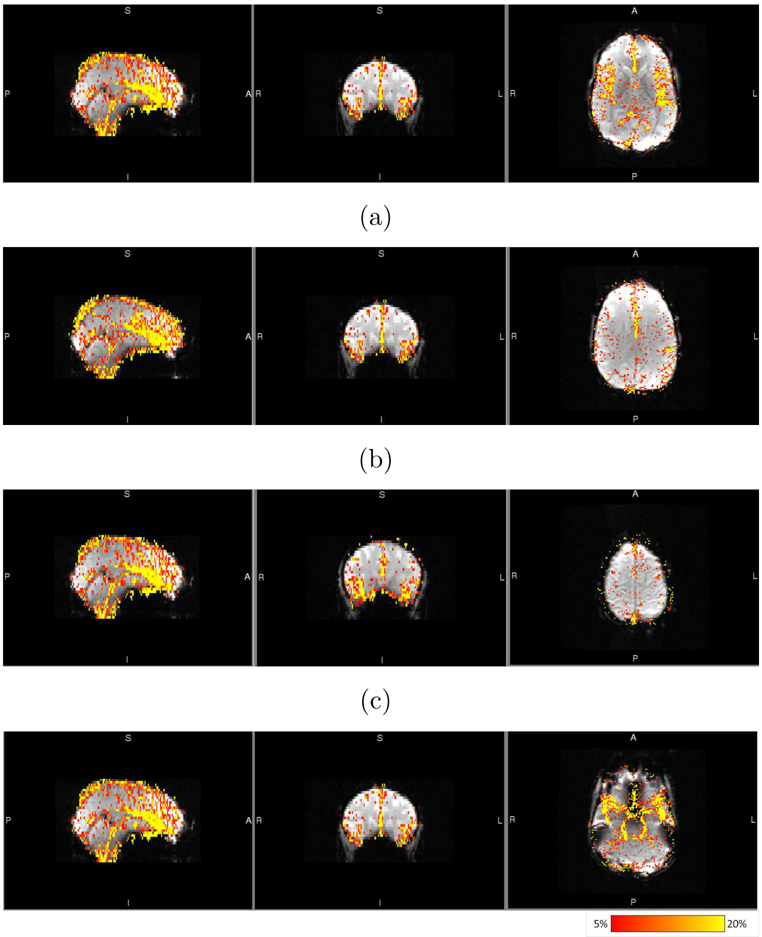

(a)

(b)

(c)

(d)

Figure 5.4: TSNR map (percentage variation) for cardiac noise correction: example of a single subject, some orthographic views. The map is superimposed onto a functional volume of the subject.

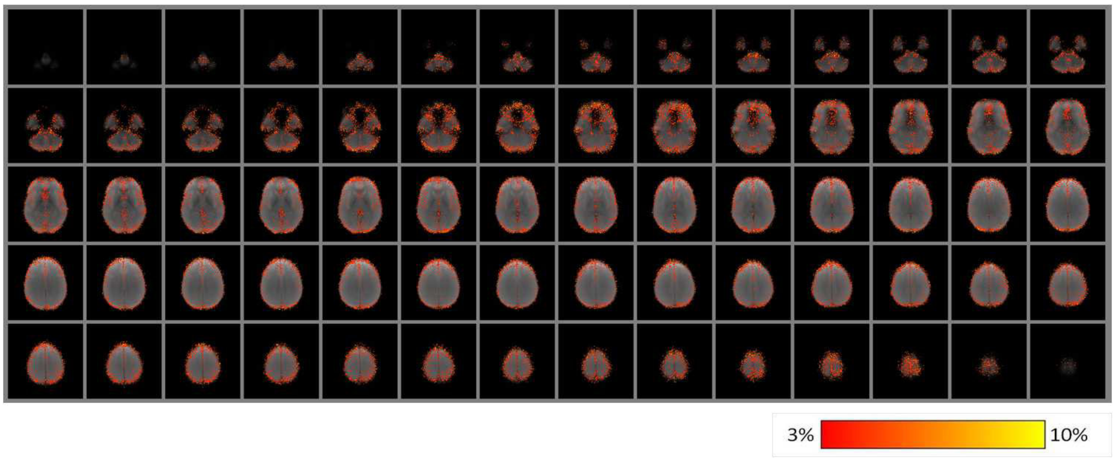

Figure 5.5: TSNR map (percentage variation) for respiratory noise correction: mean across 6 subjects, axial views. The map is superimposed onto the study specific template, to which single maps were registered.

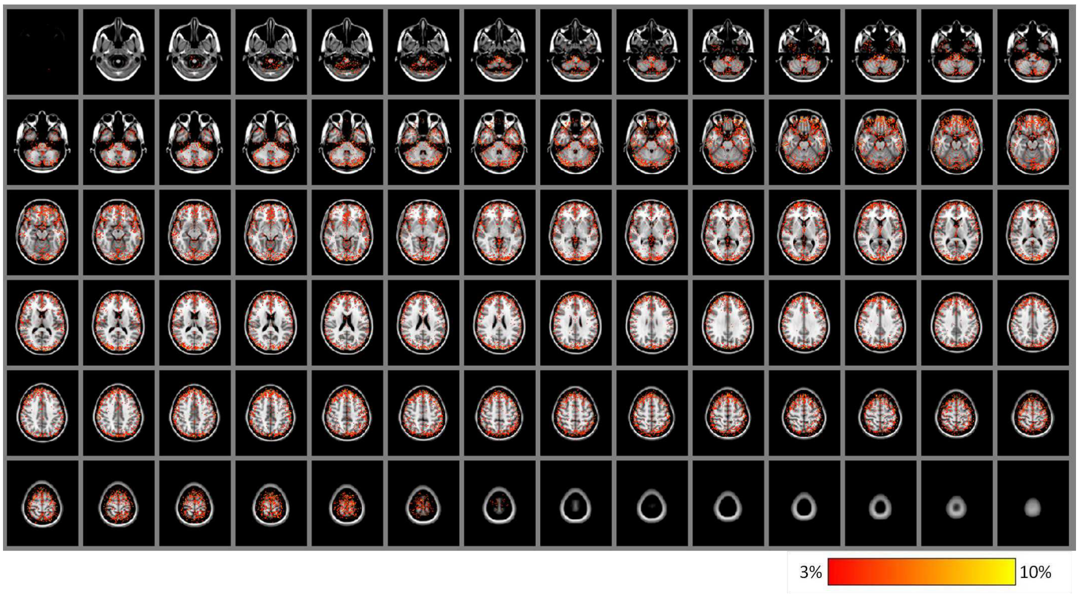

Figure 5.6: TSNR map (percentage variation) for respiratory noise correction: mean across 6 subjects, axial views. The map is superimposed onto the MNI standard template, to which it was registered.

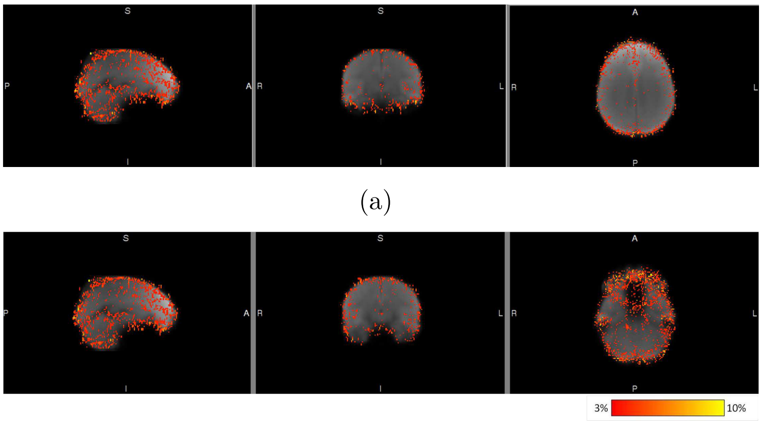

(a)

(b)

Figure 5.7: TSNR map (percentage variation) for respiratory noise correction: mean across 6 subjects, some orthographic views. The map is superimposed onto the study specific template, to which single maps were registered.

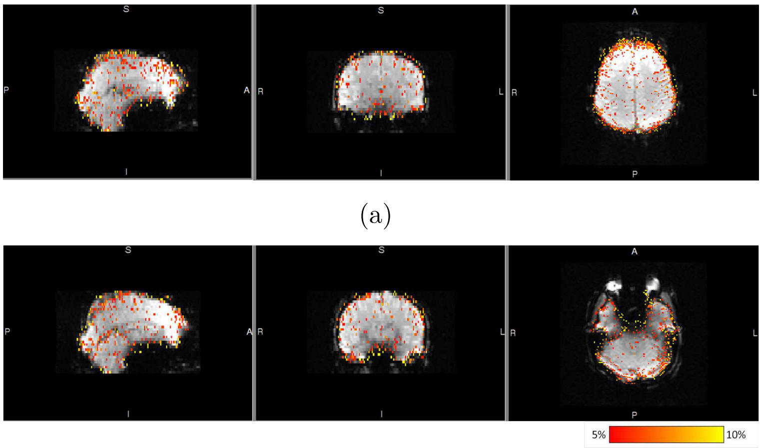

(a)

(b)

Figure 5.8: TSNR map (percentage variation) for respiratory noise correction: example of a single subject, some orthographic views. The map is superimposed onto a functional volume of the subject.

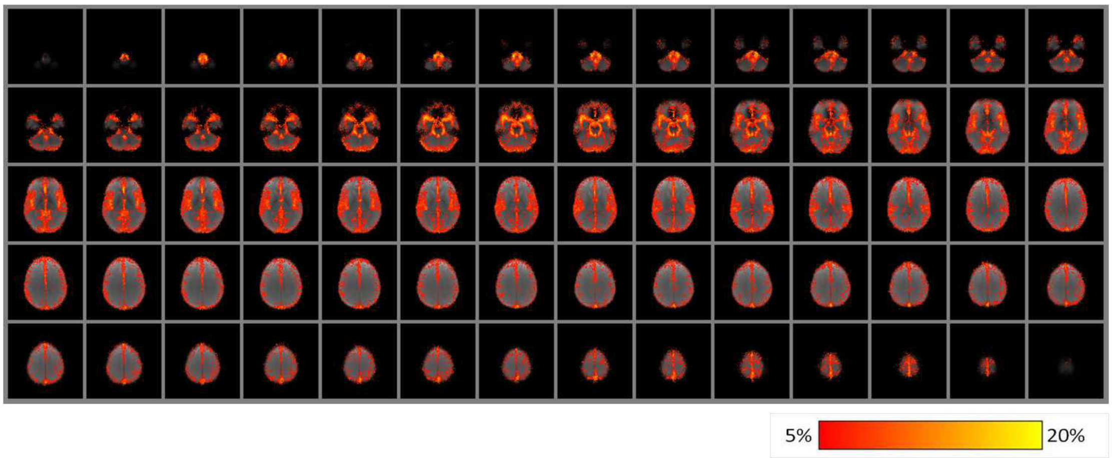

Figure 5.9: TSNR map (percentage variation) for both cardiac and respiratory noise corrections: mean across 6 subjects, axial views. The map is superimposed onto the study specific template, to which single maps were registered.

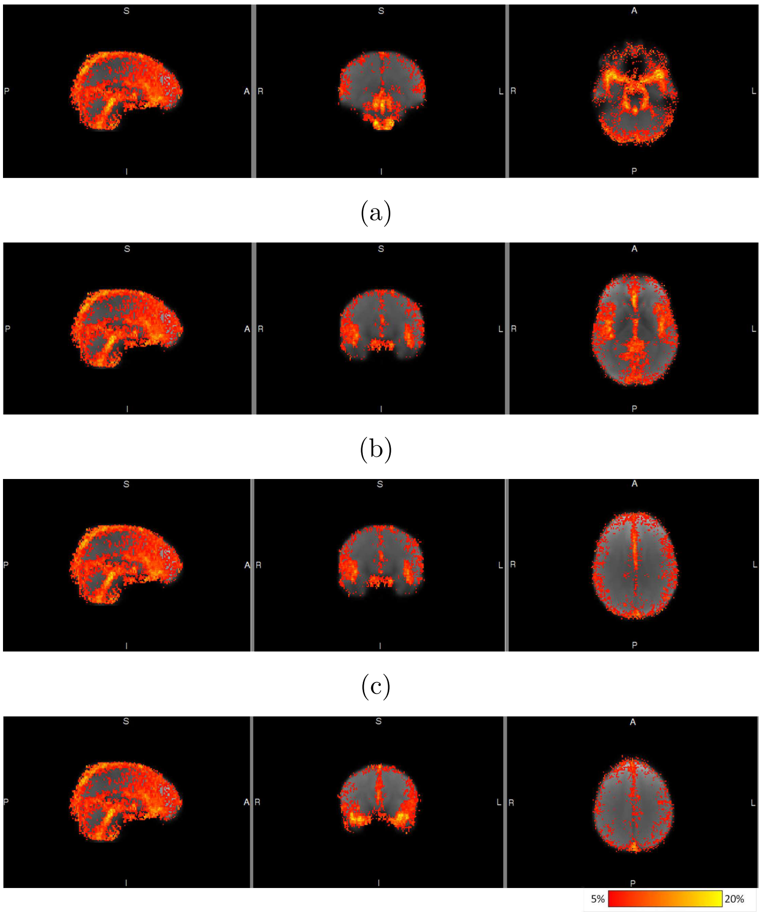

(a)

(b)

(c)

(d)

Figure 5.10: TSNR map (percentage variation) for both cardiac and respiratory noise corrections: mean across 6 subjects, some orthographic views. The map is superimposed onto the study specific template, to which single maps were registered.

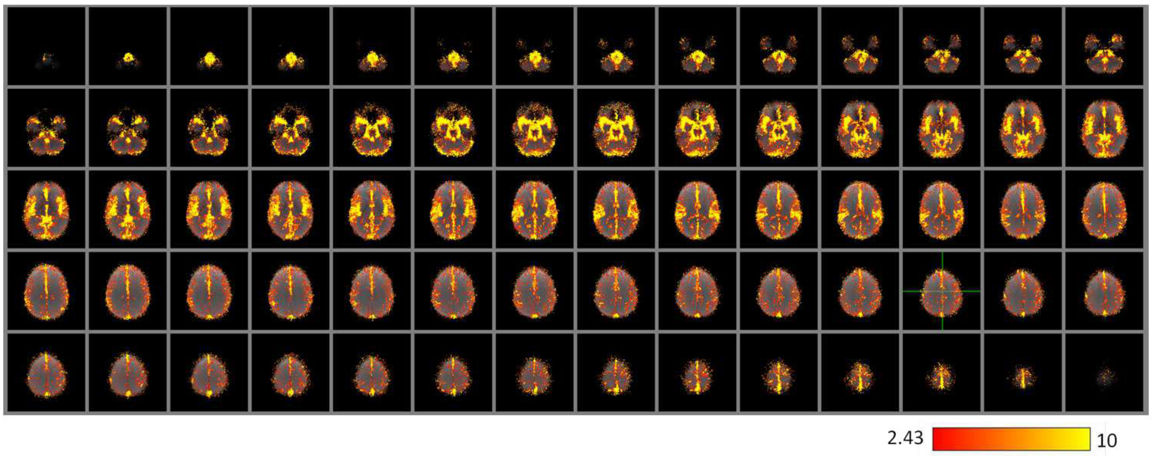

Figure 5.11: Maps of t-statistics values for % TSNR changes after the application of RETROICOR for cardiac noise, with respect to 0% level (axial views, thresholded at $t = 2.43$, that corresponds to a p-value, FDR correction, of < 0.01).

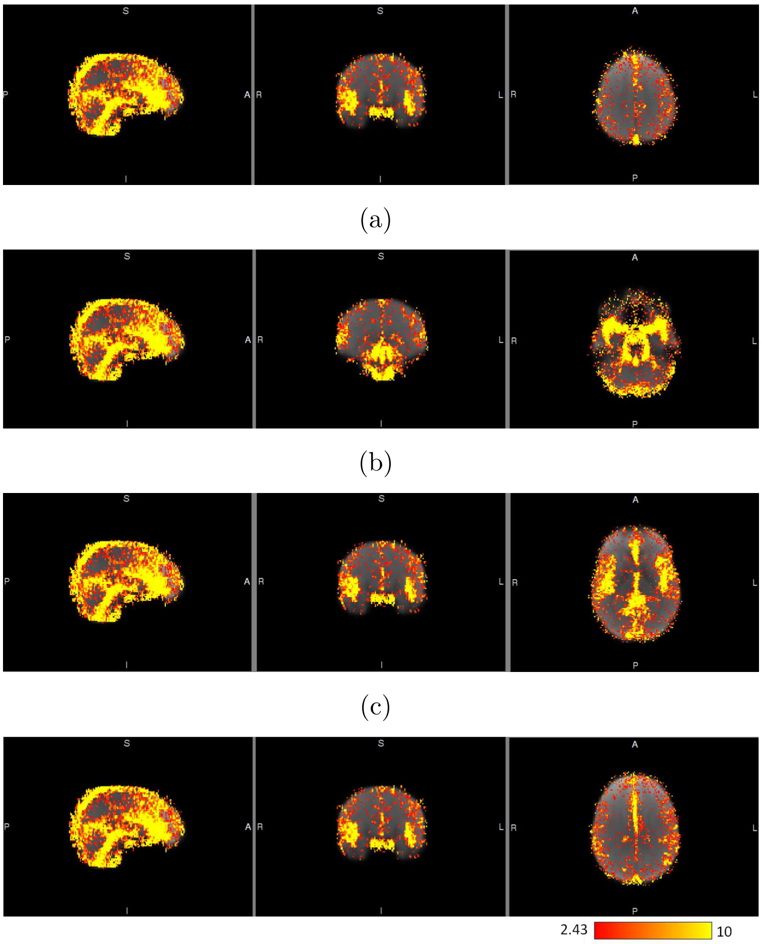

(a)

(b)

(c)

(d)

Figure 5.12: Maps of t-statistics values for % TSNR changes after the application of RETROICOR for cardiac noise, with respect to 0% level (some orthographic views, thresholded at $t = 2.43$, that corresponds to a p-value, FDR correction, < 0.01).

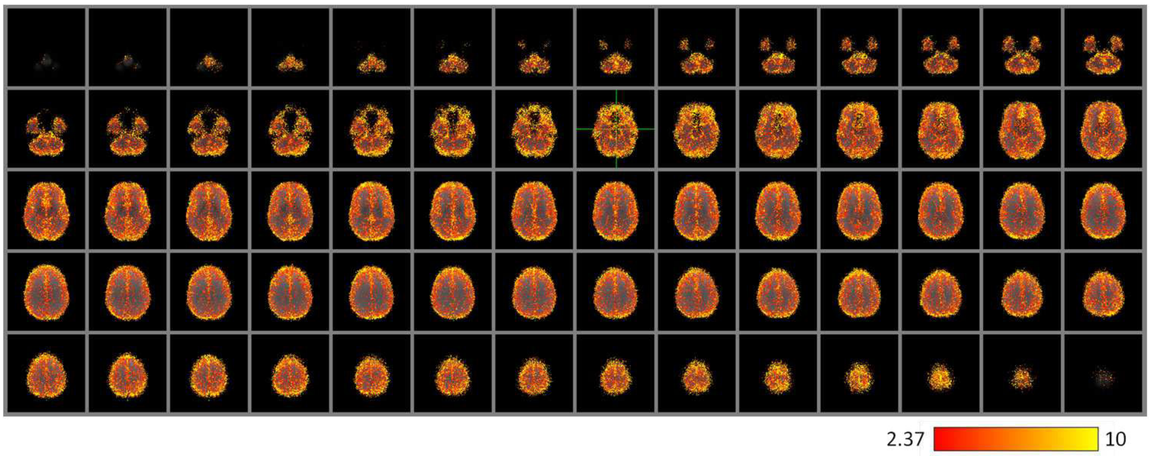

Figure 5.13: Maps of t-statistics values for % TSNR changes after the application of RETROICOR for respiratory noise, with respect to 0% level (axial views, thresholded at $t = 2.37$, that corresponds to a p-value, FDR correction, < 0.01).

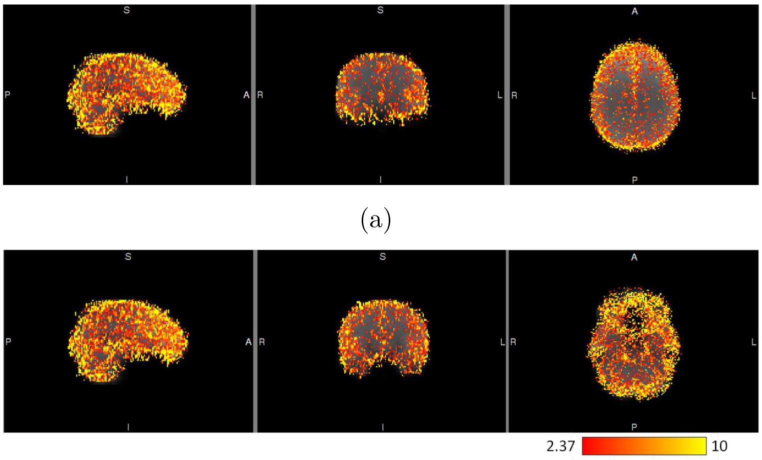

(a)

(b)

Figure 5.14: Maps of t-statistics values for % TSNR changes after the application of RETROICOR for respiratory noise, with respect to 0% level (some orthographic views, thresholded at $t = 2.37$, that corresponds to a p-value, FDR correction, < 0.01).

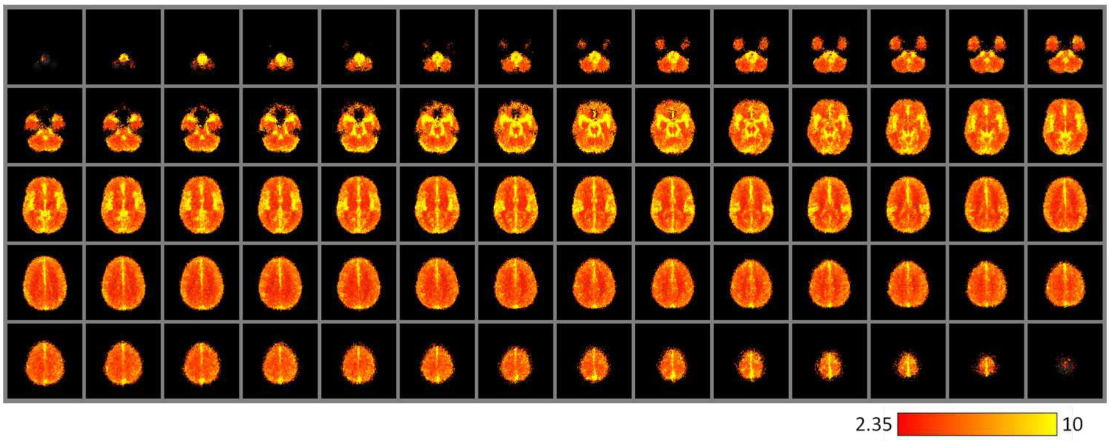

Figure 5.15: Maps of t-statistics values for % TSNR changes after the application of RETROICOR for both cardiac and respiratory noise, with respect to 0% level (axial views, thresholded at $t = 2.35$, that corresponds to a p-value, FDR correction, < 0.01).

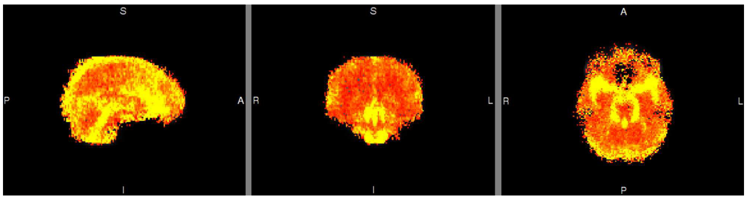

(a)

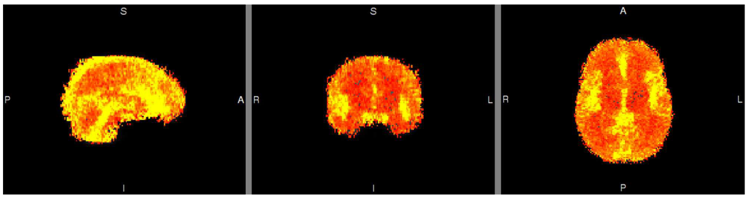

(b)

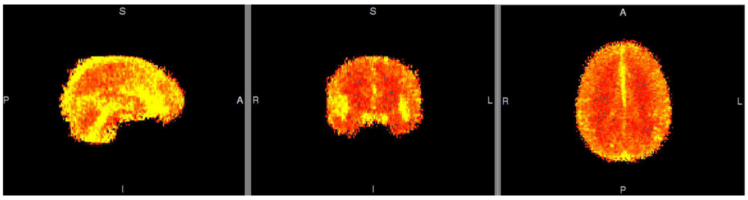

(c)

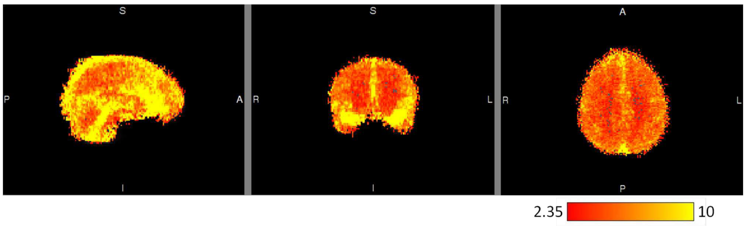

(d)

Figure 5.16: Maps of t-statistics values for % TSNR changes after the application of RETROICOR for both cardiac and respiratory noise, with respect to 0% level (some orthographic views, thresholded at $t = 2.35$, that corresponds to a p-value, FDR correction, < 0.01).

We can compare our maps with images reported in the literature, from studies that deal with the physiological-related signal changes in fMRI, such those by Dagli et al., [52], or Lund et al, [115], as far as cardiac-related noise is concerned. Dagli et al. presented a topographical description of the regions showing significant contributions of cardiac-related signal variance in resting state fMRI acquisitions. They measured the cardiac activity during MRI acquisition and estimated the signal intensity changes for each voxel during the cardiac cycle by fitting the data to a Fourier series expanded in terms of cardiac phase (quite similar to what Glover et al. proposed in [69] to correct physiological noise). They also acquired high-resolution 2D magnetic resonance angiography images to provide information on cerebral vascular anatomy, see Figure 5.18.
Their results, shown in Figure 5.17, were highly consistent across subjects, and showed that reduced sensitivity due to cardiac-induced noise in the BOLD signal is greater in specific areas, typically near major arterial and venous structures, whereas in tissue far from the major vessels the cardiac-induced variation is quite small. A notable variation is present around the sinuses, unsurprisingly as the pulsatile blood flow is unique to the cranial veins and occurs as the result of compression from pulsating brain tissue. Lund et al. [115] investigated various sources of non-white noise in BOLD fMRI, considering RETROICOR nuisance regressors in their analysis, and they also found that cardiac-induced noise is greater near majors vessels, such as the medial cerebral artery and the circle of Willis, see Figure 5.21. A good correspondence between our TSNR maps and their findings can be seen, comparing Figures 5.1, 5.2 and 5.3 with Figures 5.17, 5.18, 5.19.

As for respiratory noise, by comparing Figures 5.5, 5.6 and 5.7 with Figure 5.20 we notice that in this case too, the correction we performed tends to be more effective in areas quite consistent with what is found in literature, i.e. mainly near the edges of the brain and near CSF pools, therefore in areas where there are adjacent tissues with different susceptibility. It is important to remember that we could not directly measure respiration but used just an estimation of it.

As for the effects of physiological correction on functional connectivity results, we did not perform a systematic and detailed analysis or comparison; we can however say that, in general, the effect is that after the correction some of the smaller and less significant voxel clusters are no longer present, while bigger and more significant clusters are confirmed, sometimes with a higher level of significance and with a greater extent. Moreover, edges of active areas are cleaner and some clusters that were in areas where BOLD activation is not expected (such as the ventricles) tend to disappear (see Figures 5.22 and 5.23 for examples). It therefore seems that functional connectivity analysis on physiological-noise corrected data gives somewhat cleaner results.

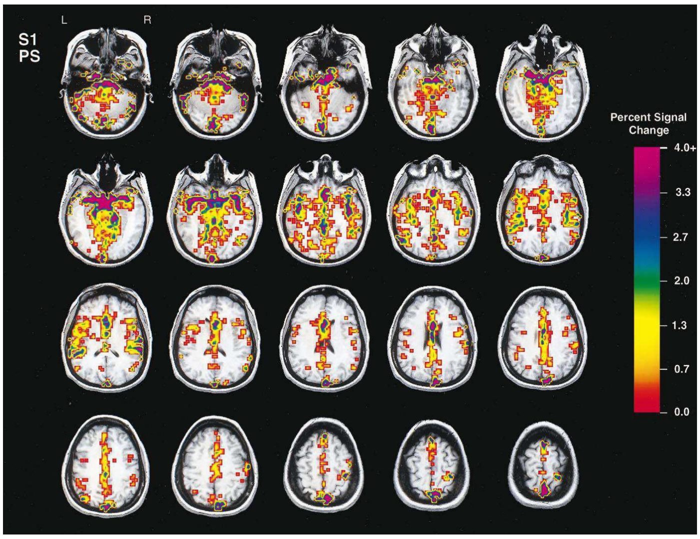

Figure 5.17: The full volume of a typical subject showing a topographical display of the percentage signal change during the cardiac cycle. Pixels shown in color indicate regions demonstrating significant cardiac-related signal changes, [52].

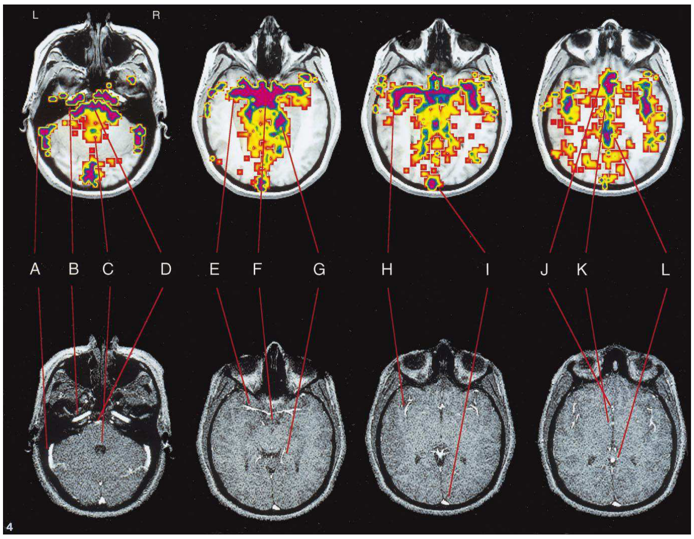

Figure 5.18: Comparison of selected functional slices (top slices) from one subject with the cerebral vasculature as examined by magnetic resonance angiography (bottom slices). There is a strong correspondance of tissue areas showing significant cardiac-related signal change to the locations of major blood vessels and CSF pools (A - transverse sinus, B - carotid artery, C - fourth ventricle, D - basilar artery, E - main trunk of middle cerebral artery (MCA), F - circle of Willis (entire region), G - posterior cerebral artery, H - branch of MCA, I - superior sagittal sinus, J - anterior cerebral artery, K - third ventricle, L - inferior sagittal sinus), [52].

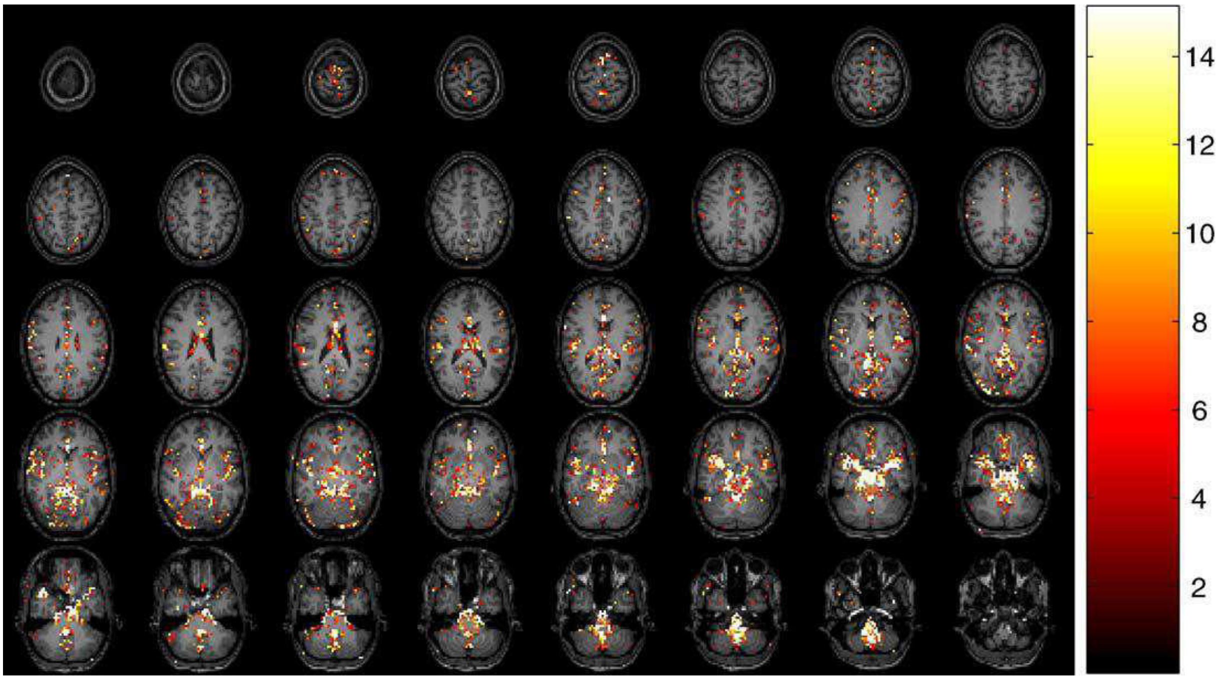

Figure 5.19: Cardiac-induced noise: F-test values of the voxels showing significant (P = 0.05 corrected using GRF) effect of a linear combination of the regressors describing the aliased cardiac oscillation. It is seen that the cardiac-induced noise is dominant near larger vessels (e.g. medial cerebral artery and Circle of Willis, see Figure 5.21), [115].

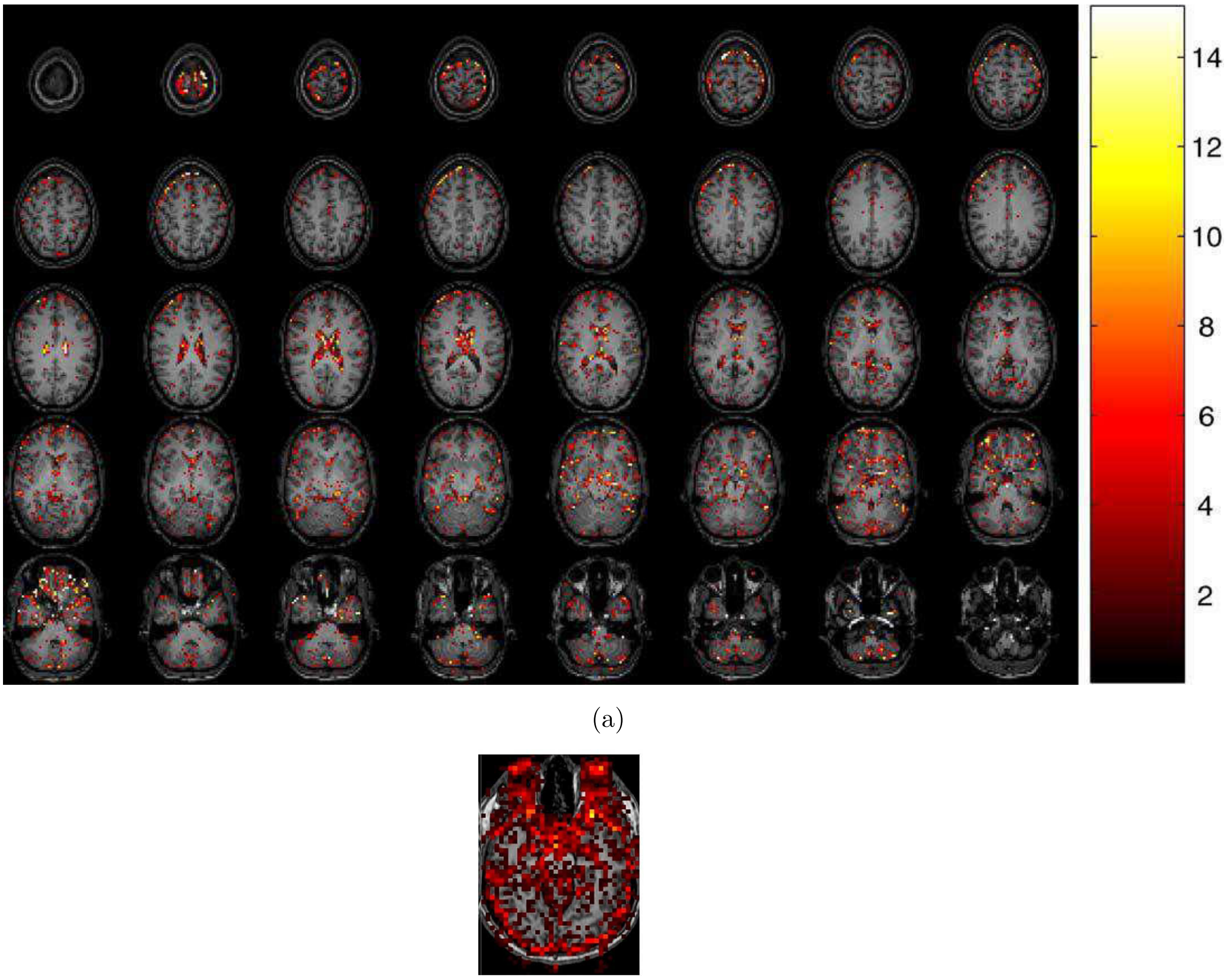

(a)

(b)

Figure 5.20: (a) Respiratory-induced noise: F test values of the voxels showing significant (P = 0.05 corrected using FDR) effect of a linear combination of the regressors describing the aliased respiratory oscillation. It is see that the respiratory-induced noise is dominant near the edges of the brain as well as near in the larger veins and in the ventricles, [115]; (b) coupling power from RETROICOR for respiratory data, [72]

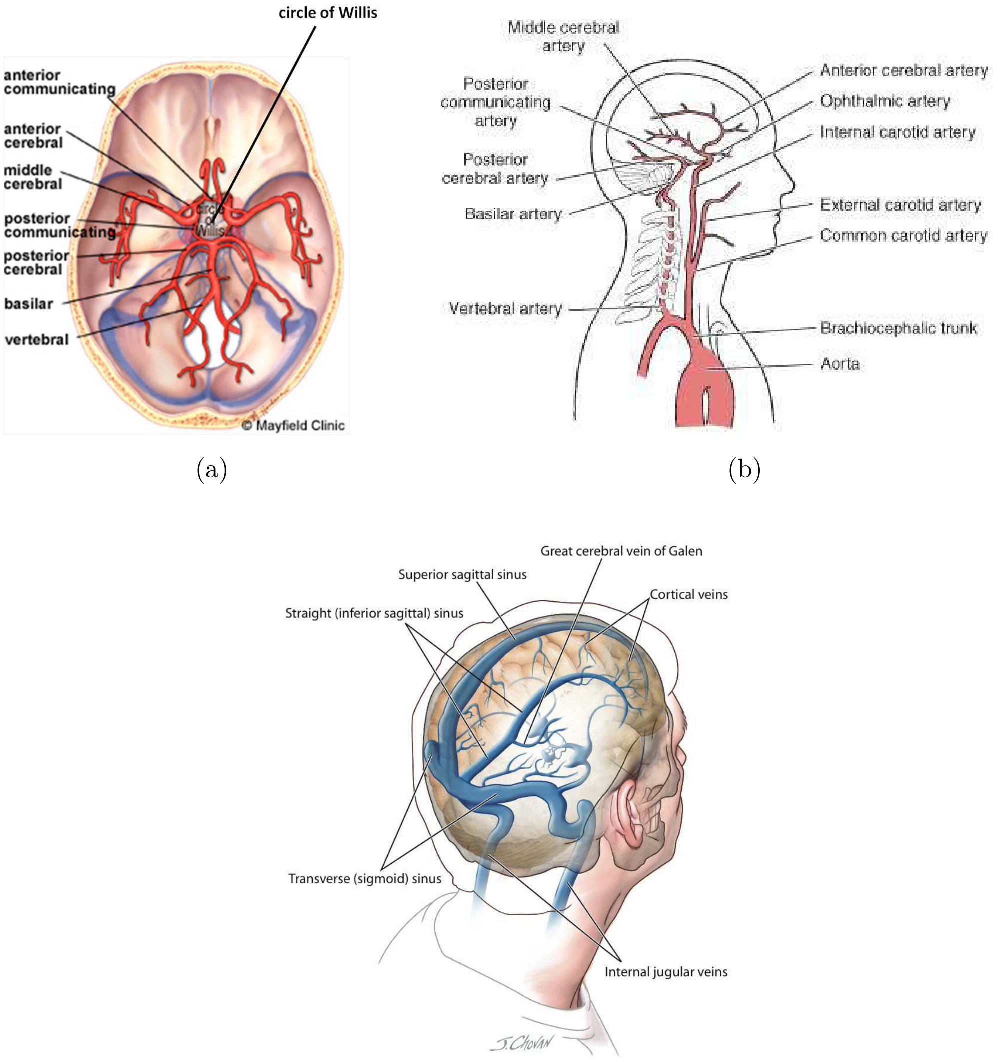

(a) (b)

(c)

Figure 5.21: Schematic representation of arterial system (inferior view (a), lateral view (b)) and of venous system (c) in human brain - *sources: (a)http://www.mayfieldclinic.com/PE-AnatBrain.htm#.Ui3eDD8atO-, (b) http://newnurseblog.com/2011/03/16/the-neuro-icu-for-beginners/arteries/, (c) http://patientblog.clotconnect.org/2011/02/07/sinus-and-cerebral-vein-thrombosis/*

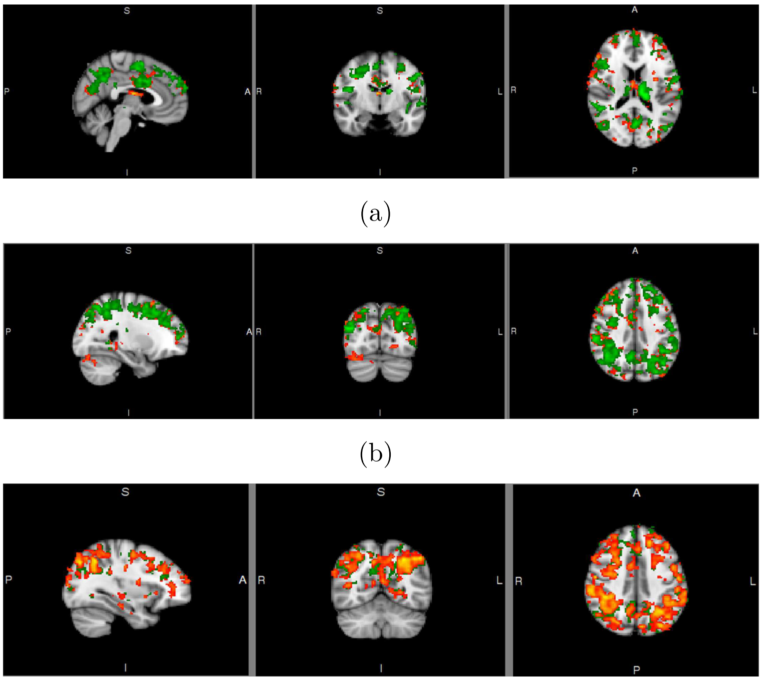

(a)

(b)

(c)

Figure 5.22: Examples of comparison between the results of FC analysis (with seed in the precentral gyrus) performed on the same dataset before (red) and after (green) the physiological noise correction.

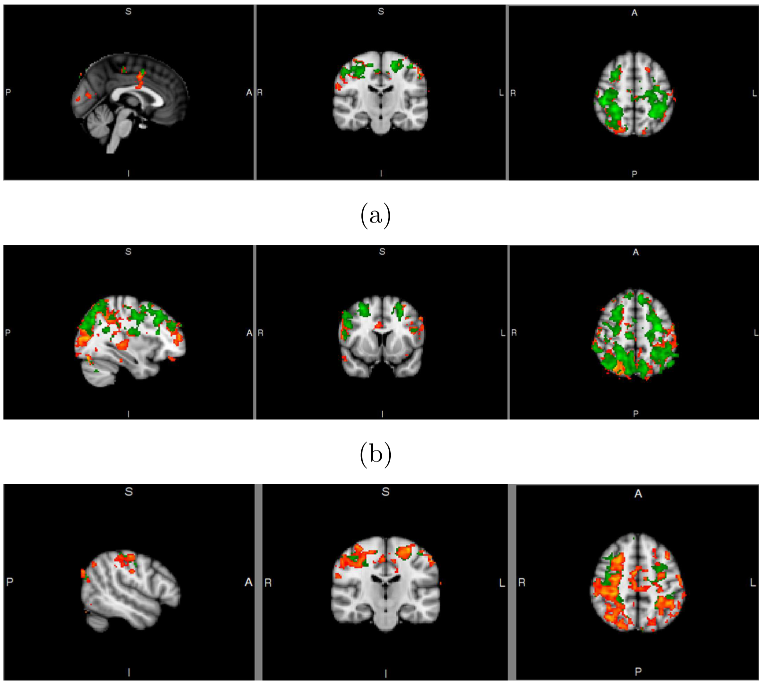

(a)

(b)

(c)

Figure 5.23: Examples of comparison between the results of FC analysis (with seed in the SMA) performed on the same dataset before (red) and after (green) the physiological noise correction.

5.2 Seed-based connectivity group analysis

Figures 5.24 and 5.25 show few examples of functional connectivity results for a single subject, comparing the ON state (after taking L-dopa, in green) with the OFF state (before taking L-dopa, in red). The general trend is that after the intake of L-dopa there is an increased connectivity with all four seeds, both as for significance level and as for the extent of connected areas. We'll see that this trend is confirmed in the group analysis.

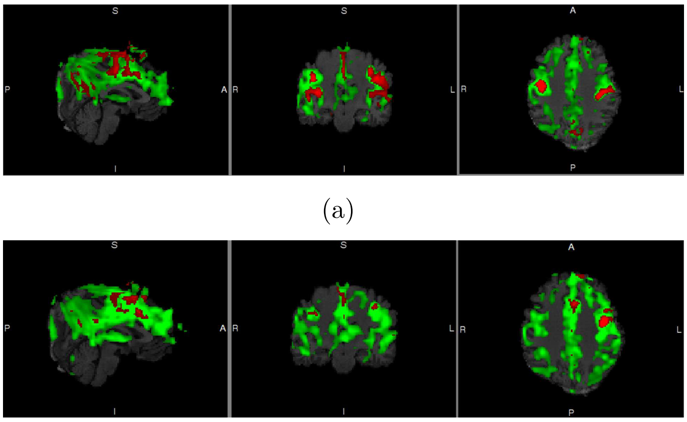

(a)

(b)

Figure 5.24: Functional connectivity (red - OFF state, green - ON state), examples for a single subject: (a) seed in right precentral gyrus, (b) seed in left precentral gyrus.

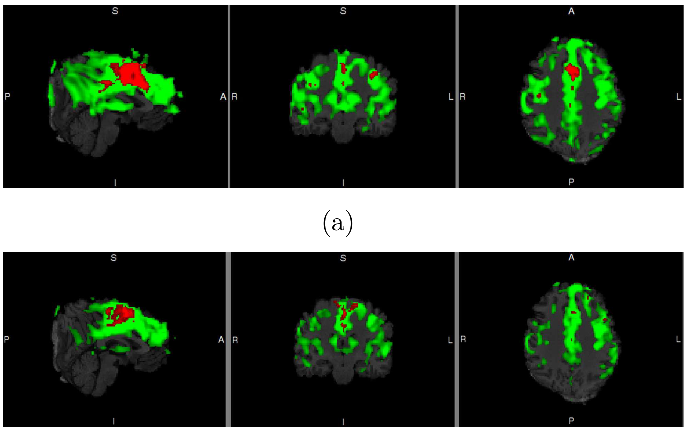

(a)

(b)

Figure 5.25: Functional connectivity (red - OFF state, green - ON state), examples for a single subject: (a) seed in right SMA, (b) seed in left SMA.

Figures from 5.26 to 5.37 show group analysis results. In the background there is the MNI template, only brain structures are shown (no scalp). The connectivity areas that showed a significant (z-statistic, from a 2 samples paired t-test, cluster GRF correction, see 4.5.4 for more details) difference between ON state and OFF

state, averaging all 6 patients, are displayed in color. In other words, areas that are more significantly connected with that specific seed in the ON state rather than in the OFF state are shown. Figures 5.26 5.27 5.28 refer to connectivity with right precentral gyrus, Figures 5.29 5.30 5.31 with left precentral gyrus, Figures 5.32 5.33 5.34 with right SMA and Figures 5.35 5.36 5.37 with left SMA.
Images show orthographic views of areas in which we found significant clusters of voxels. We did not find any significant clusters of deactivation, thus in the following only activations are discussed. The main areas involved are essentially the cingulate (both anterior and posterior divisions), the precuneus, the cortex motor area, the sensorimotor area, the SMA, the parietal lobe and the thalamus, to different extents when using different seeds to compute connectivity with. To have a more quantitative measure of these areas than images, we masked the z-statistic maps with some of the brain structures defined in the Harvard cortical and subcortical structural probabilistic atlas: cingulate gyrus anterior division, cingulate gyrus posterior division, middle frontal gyrus, postcentral gyrus, precentral gyrus, precuneus cortex, superior frontal gyrus, superior parietal lobe, supplementary motor cortex, lateral occipital cortex superior division, left and right thalamus (see Figure 5.38 and 5.39). Once z-statistic maps were masked with each one of these areas, we considered the number of voxels activated within that area, the maximum intensity, the coordinates of the voxel that show maximum intensity and the coordinates of the Centre of Gravity (COG), intended as a weighted average of the coordinates by the intensities of each voxel (it is equivalent to the concept of centre of gravity for an object with distributed mass, where intensity substitutes for mass in this case). In table 5.1 the connectivity with right precentral gyrus is reported, table 5.2 for the connectivity with left precentral gyrus, table 5.3 for the connectivity with right SMA and table 5.4 for the connectivity with left SMA.

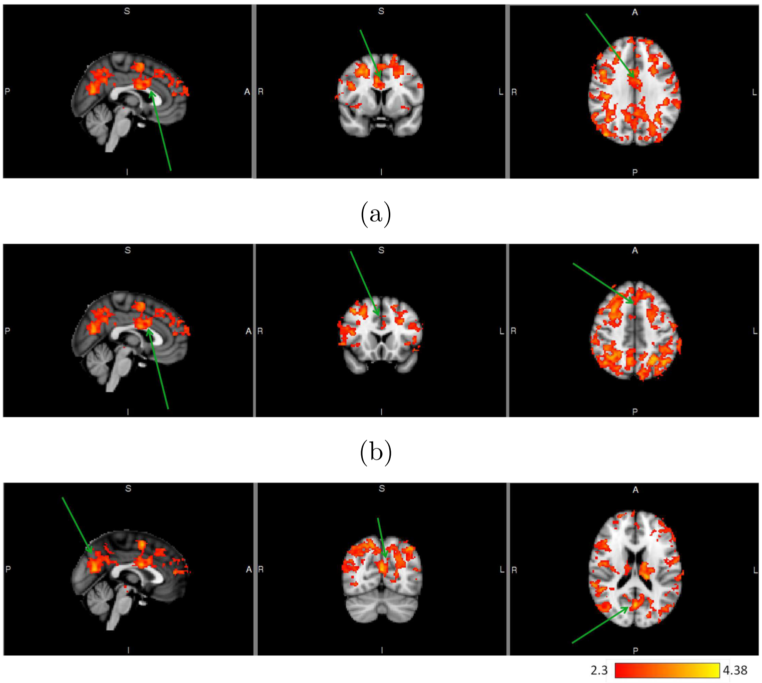

(a)

(b)

(c)

Figure 5.26: Functional connectivity: group analysis of ON state versus OFF state, with seed in right precentral gyrus; (a) cingulate, (b) cingulate, (c) precuneus.

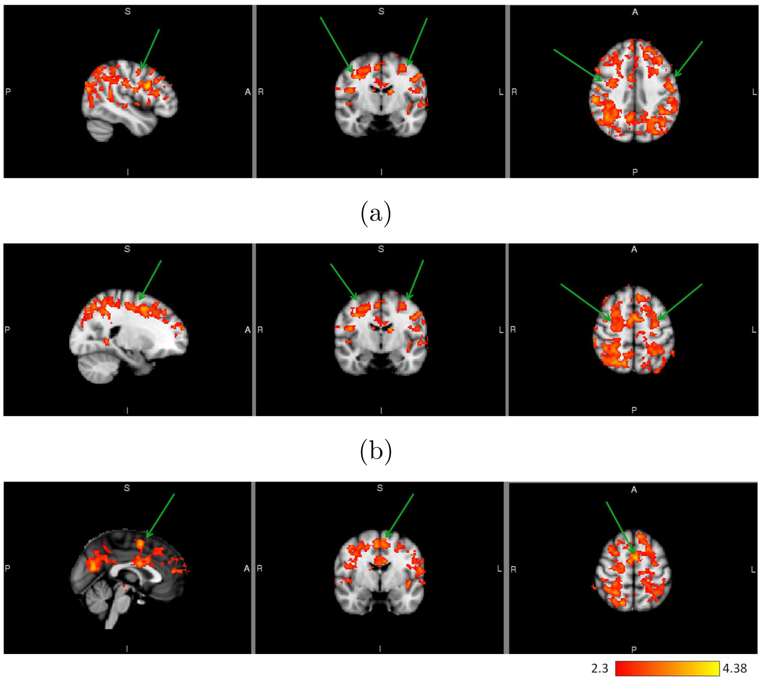

(a)

(b)

(c)

Figure 5.27: Functional connectivity: group analysis of ON state versus OFF state, with seed in right precentral gyrus; (a) motor area, (b) sensorimotor area, (c) SMA.

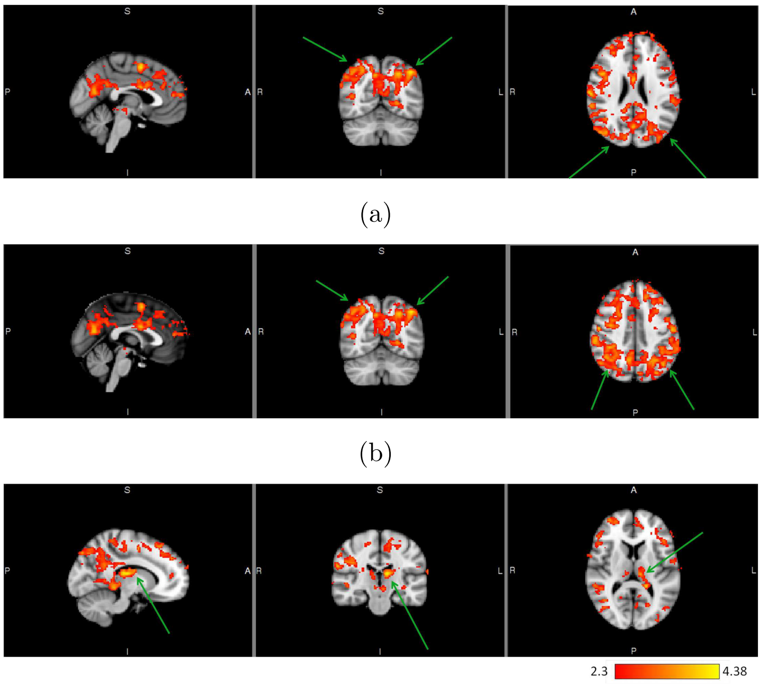

(a)

(b)

(c)

Figure 5.28: Functional connectivity: group analysis of ON state versus OFF state, with seed in right precentral gyrus; (a) parietal lobe, (b) parietal lobe, (c) thalamus.

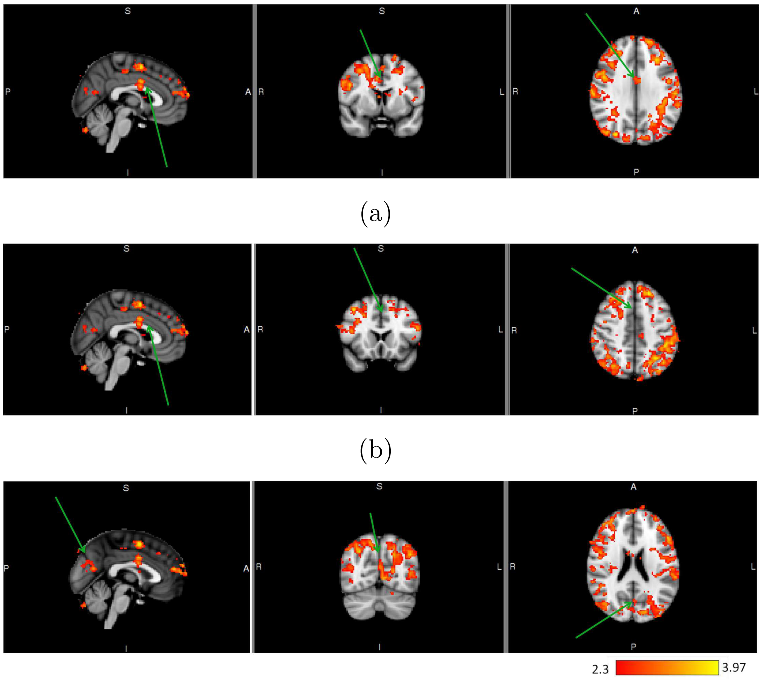

(a)

(b)

(c)

Figure 5.29: Functional connectivity: group analysis of ON state versus OFF state, with seed in left precentral gyrus;(a) cingulate, (b) cingulate, (c) precuneus.

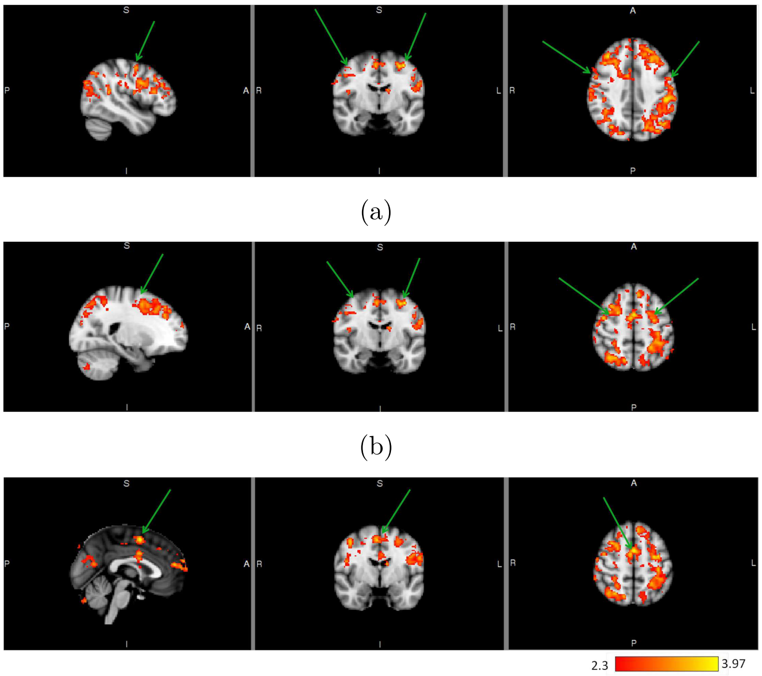

(a)

(b)

(c)

Figure 5.30: Functional connectivity: group analysis of ON state versus OFF state, with seed in left precentral gyrus; (a) motor area, (b) sensorimotor area, (c) SMA.

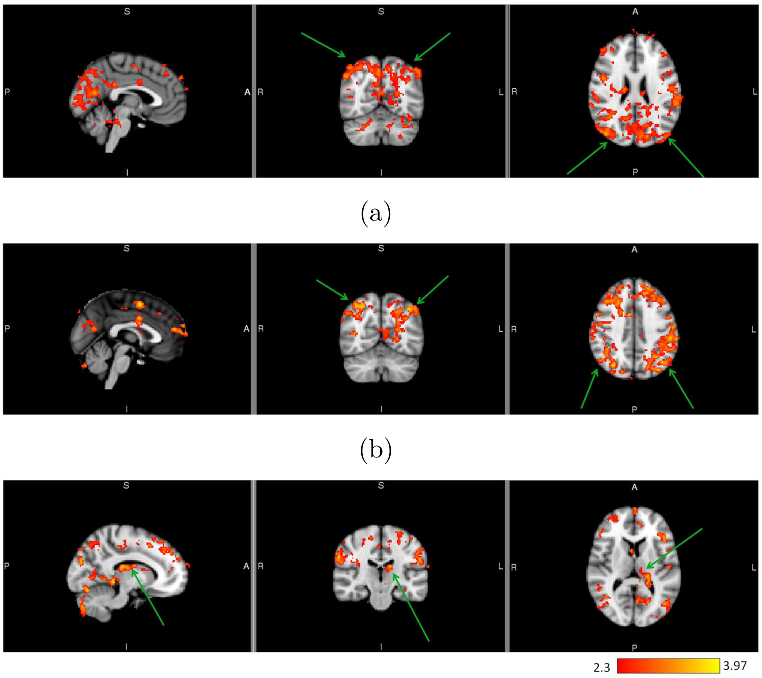

(a)

(b)

(c)

Figure 5.31: Functional connectivity: group analysis of ON state versus OFF state, with seed in left precentral gyrus; (a) parietal lobe, (b) parietal lobe, (c) thalamus.

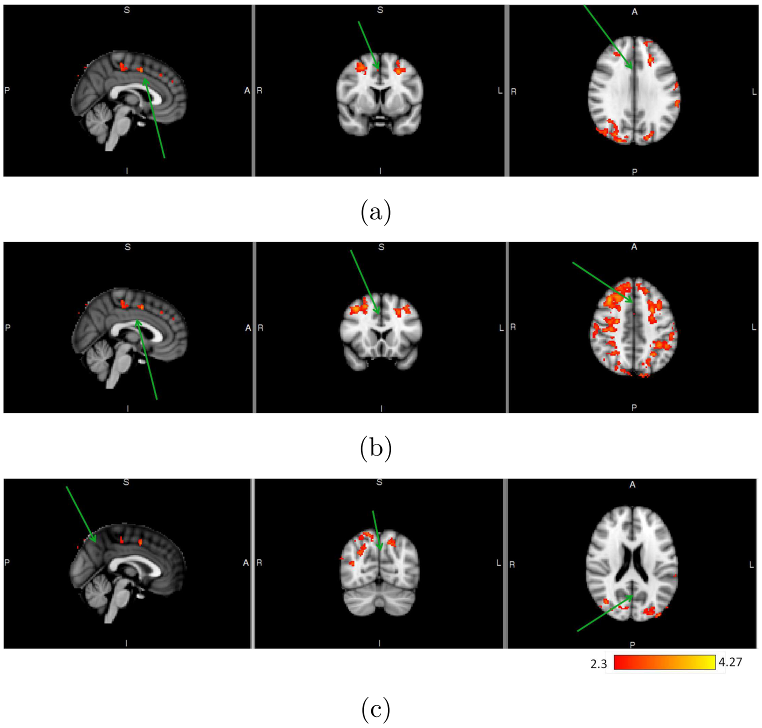

(a)

(b)

(c)

Figure 5.32: Functional connectivity: group analysis of ON state versus OFF state, with seed in right SMA; (a) cingulate, (b) cingulate, (c) precuneus.

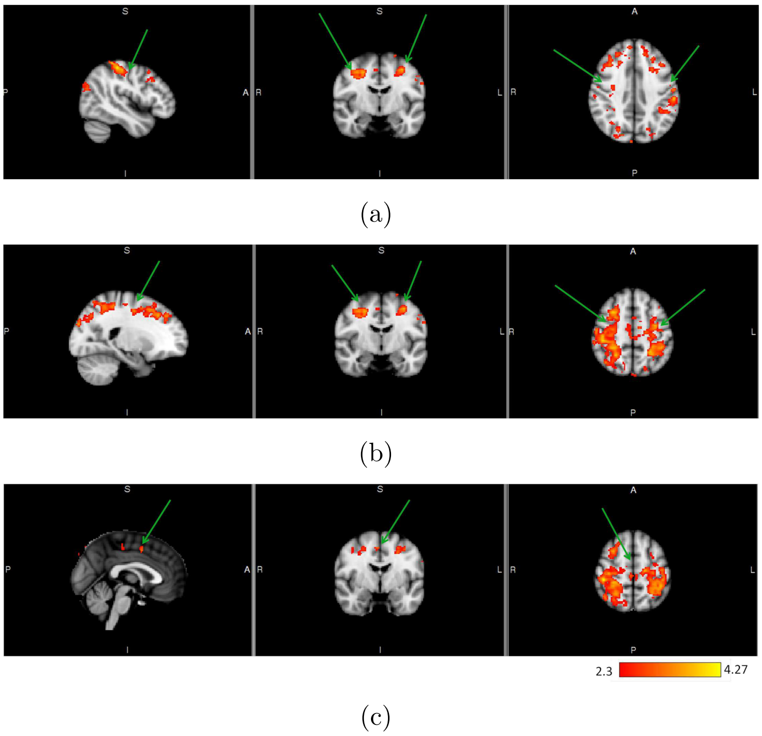

(a)

(b)

(c)

Figure 5.33: Functional connectivity: group analysis of ON state versus OFF state, with seed in right SMA; (a) motor area, (b) sensorimotor area, (c) SMA.

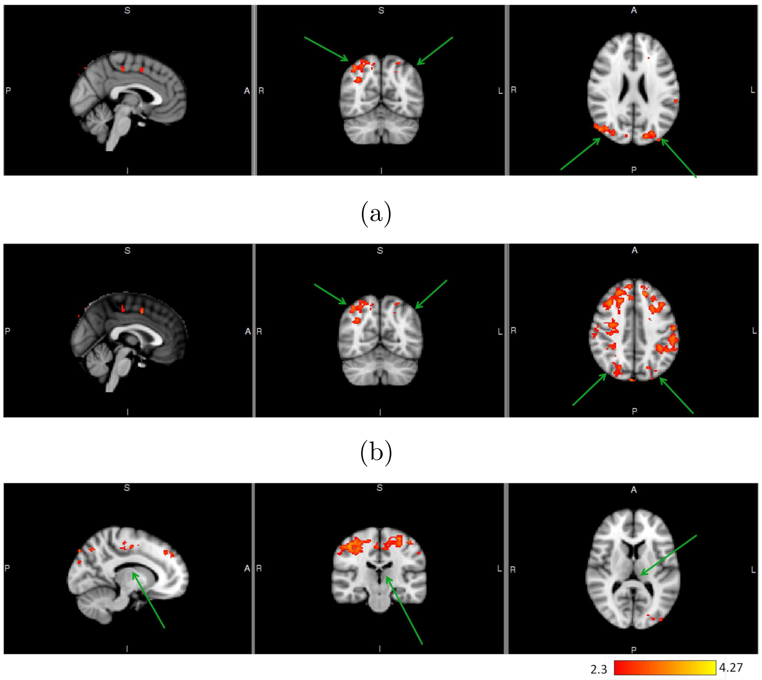

(a)

(b)

(c)

Figure 5.34: Functional connectivity: group analysis of ON state versus OFF state, with seed in right SMA; (a) parietal lobe, (b) parietal lobe, (c) thalamus.

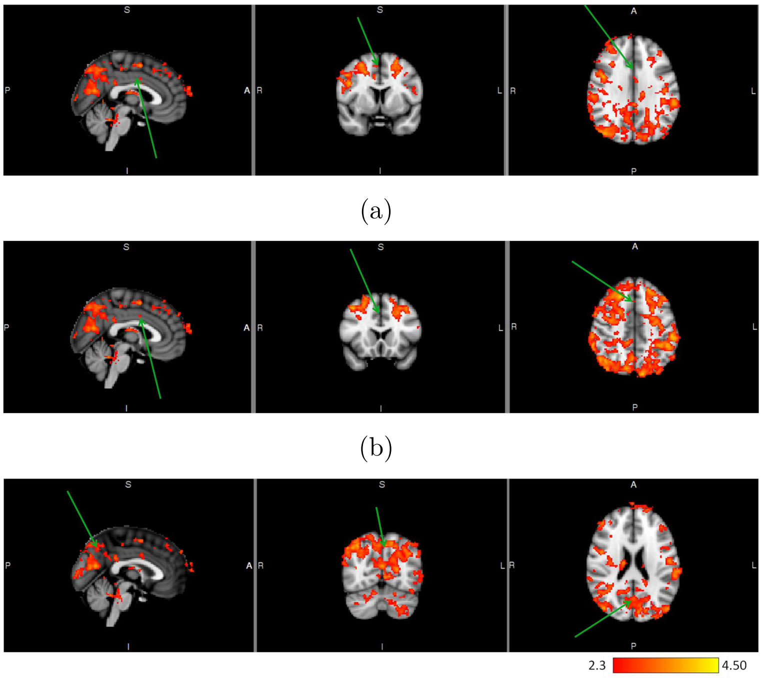

(a)

(b)

(c)

Figure 5.35: Functional connectivity: group analysis of ON state versus OFF state, with seed in left SMA; (a) cingulate, (b) cingulate, (c) precuneus.

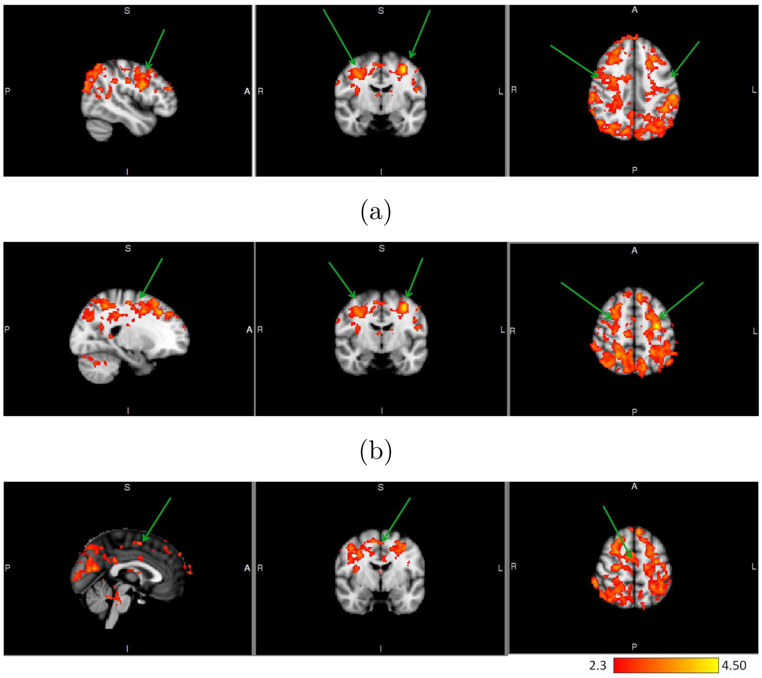

(a)

(b)

(c)

Figure 5.36: Functional connectivity: group analysis of ON state versus OFF state, with seed in left SMA; (a) motor area, (b) sensorimotor area, (c) SMA.

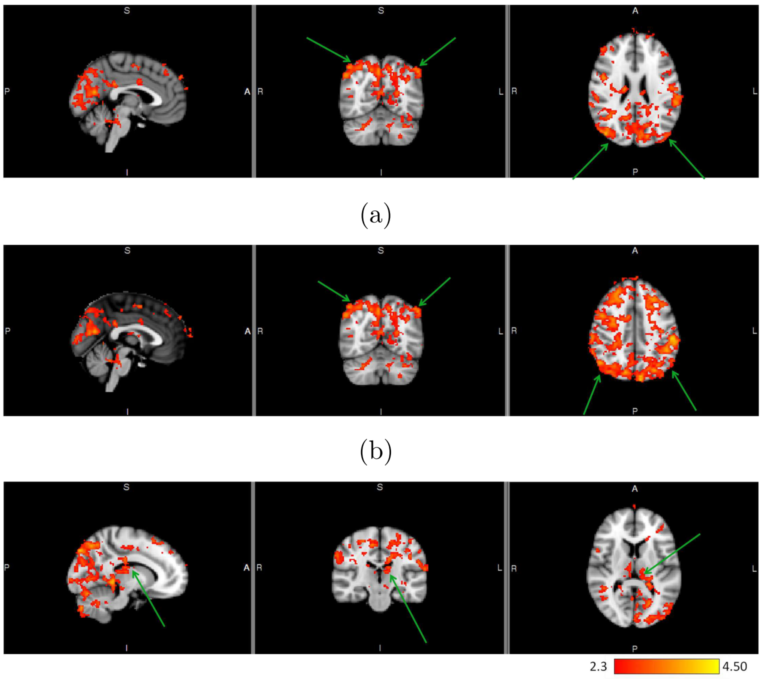

(a)

(b)

(c)

Figure 5.37: Functional connectivity: group analysis of ON state versus OFF state, with seed in left SMA; (a) parietal lobe, (b) parietal lobe, (c) thalamus.

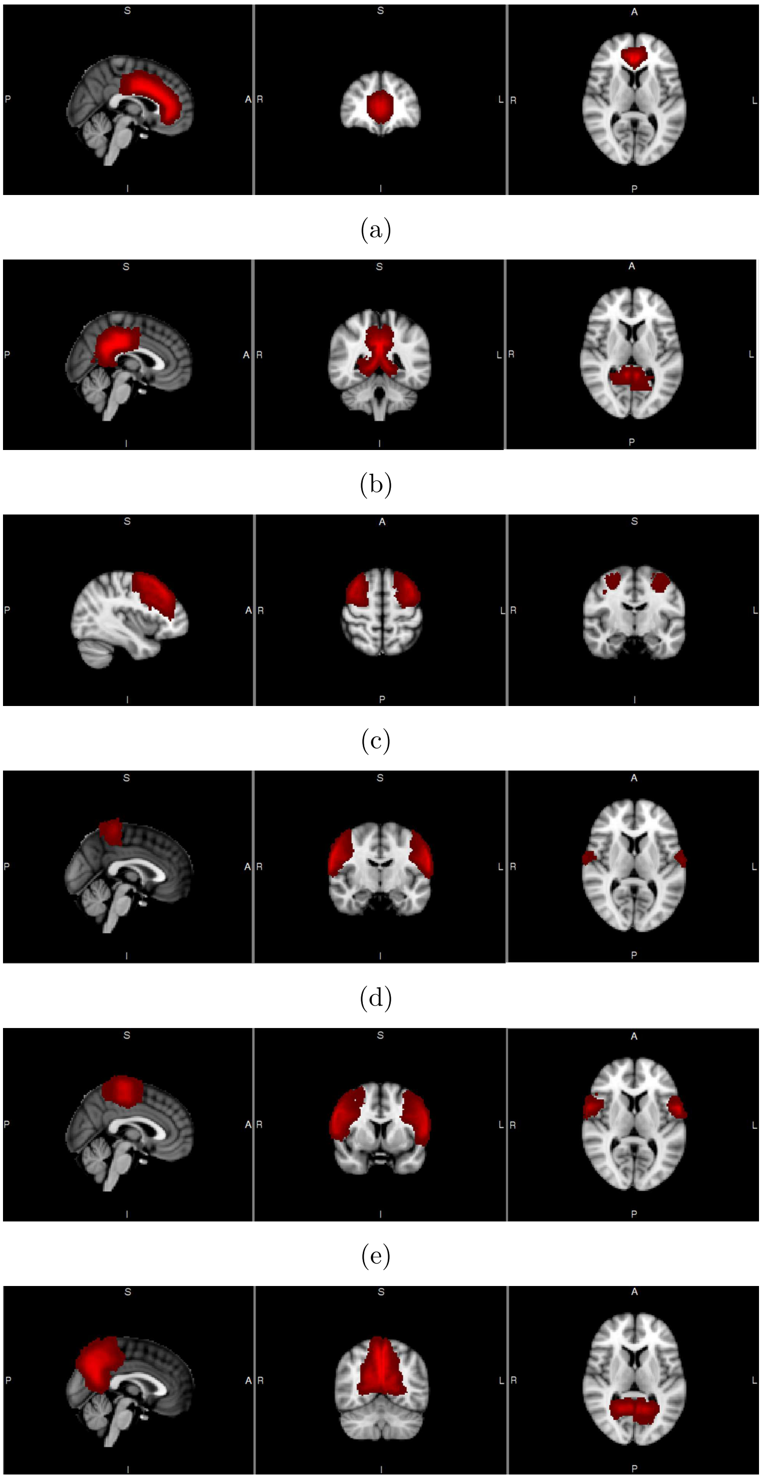

(a)

(b)

(c)

(d)

(e)

(f)

Figure 5.38: Brain areas from the Harvard cortical and subcortical structural atlas, (a) cingulate gyrus (anterior division), (b) cingulate gyrus (posterior division), (c) middle frontal gyrus, (d) postcentral gyrus, (e) precentral gyrus, (f) precuneus cortex.

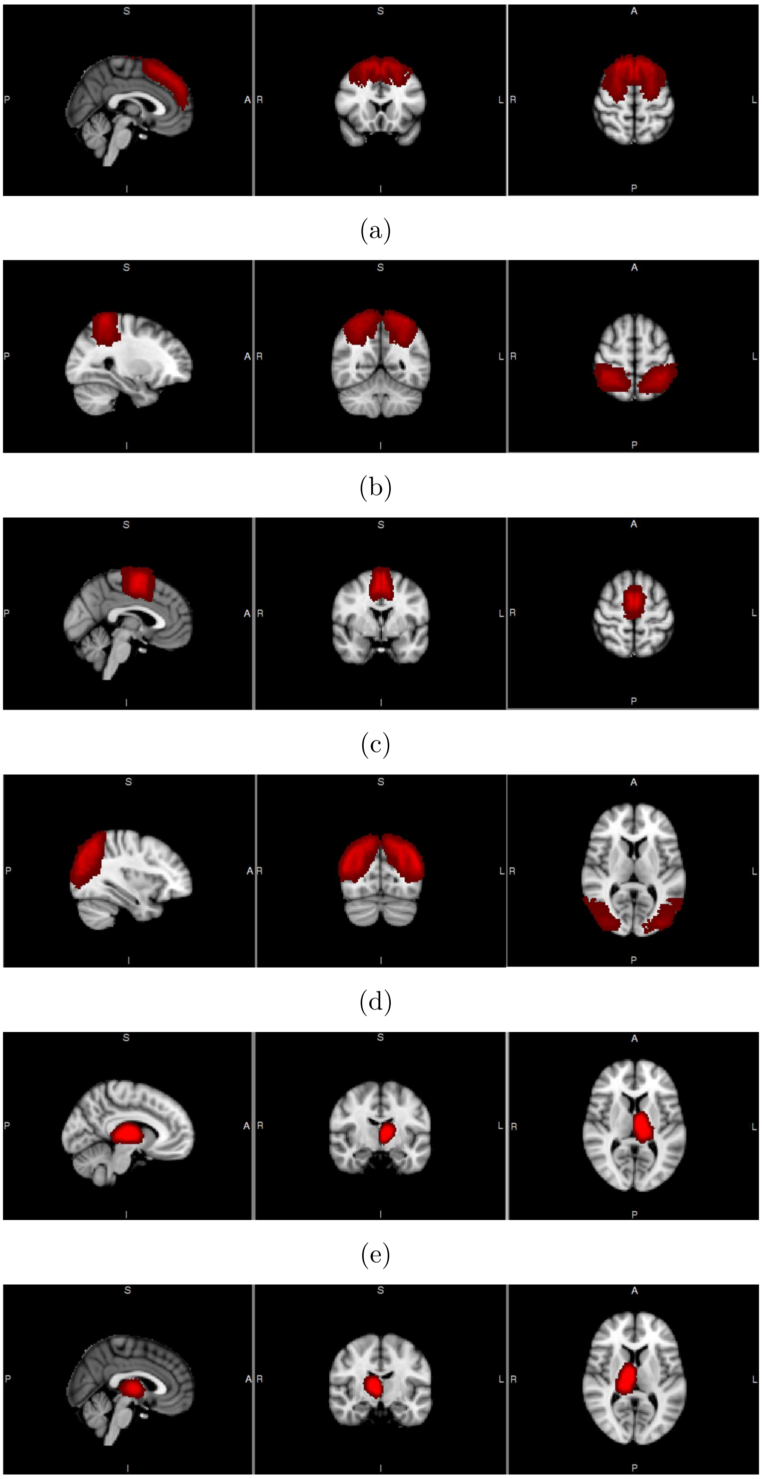

(a)

(b)

(c)

(d)

(e)

(f)

Figure 5.39: Brain areas from the Harvard cortical and subcortical structural atlas, (a) superior frontal gyrus, (b) superior parietal lobe, (c) supplementary motor cortex, (d) lateral occipital cortex (superior division), (e) left thalamus, (f) right thalamus.

Brain areas	Voxels	Max intensity	Coordinates (Max)			Coordinates (COG)		
			x	y	z	x	y	z
Cingulate gyrus (anterior)	1376	4.072	46	63	63	44.640	67.075	53.438
Cingulate gyrus (posterior)	2106	3.761	33	39	37	46.045	40.428	49.150
Middle frontal gyrus	5194	4.161	22	68	49	41.499	71.551	55.647
Postcentral gyrus	4041	3.993	14	53	48	45.032	48.786	57.118
Precentral gyrus	4814	4.161	22	68	49	41.279	60.692	55.883
Precuneus cortex	4205	3.964	45	29	45	46.240	32.276	52.701
Superior frontal gyrus	4577	4.096	46	64	63	43.762	72.809	58.770
Superior parietal lobe	4277	3.931	58	34	58	43.427	38.103	60.171
Supplementary motor cortex	820	4.096	46	64	63	44.898	62.114	61.920
Lateral occipital cortex (superior)	7234	4.191	67	32	60	44.761	29.376	54.911
Left thalamus	629	4.378	53	50	44	51.442	50.934	41.247
Right thalamus	204	3.386	41	55	43	39.395	53.417	42.016

Table 5.1: List of main brain areas showing a significant connectivity with the right precentral gyrus when comparing the ON state versus the OFF state (z-statistic map, from a 2 samples paired t-test, $p < 0.05$, cluster correction). Coordinates are given in voxels, referred to the MNI space; COG: Centre of Gravity.

Brain areas	Voxels	Max intensity	Coordinates (Max)			Coordinates (COG)		
			x	y	z	x	y	z
Cingulate gyrus (anterior)	709	3.887	45	64	63	44.454	65.944	54.838
Cingulate gyrus (posterior)	602	3.745	50	43	33	48.710	42.351	44.247
Middle frontal gyrus	4858	3.972	55	81	58	41.608	73.100	55.227
Postcentral gyrus	3613	3.925	70	49	54	52.765	50.361	55.851
Precentral gyrus	3712	3.837	44	64	64	44.053	61.452	56.079
Precuneus cortex	1864	3.585	52	21	48	48.042	29.321	51.011
Superior frontal gyrus	3776	3.972	55	81	58	43.760	74.084	58.603
Superior parietal lobe	2988	3.892	70	48	55	51.783	38.536	59.596
Supplementary motor cortex	643	3.887	45	64	63	44.362	61.078	62.109
Lateral occipital cortex (superior)	5757	3.847	30	23	51	46.869	28.571	54.150
Left thalamus	541	3.854	52	50	44	52.456	49.673	40.591
Right thalamus	2	2.314	42	64	42	42.000	63.500	42.500

Table 5.2: List of main brain areas showing a significant connectivity with the left precentral gyrus when comparing the ON state versus the OFF state (z-statistic map, from a 2 samples paired t-test, $p < 0.05$, cluster correction). Coordinates are given in voxels, referred to the MNI space; COG: Centre of Gravity.

Main areas connected with the right precentral gyrus in the ON state (and not in the OFF state) are the cingulate gyrus (both anterior and posterior), involved in the DMN (default mode network), the parietal and occipital areas, involved in attentional and visuo-spatial activities, the dorsal lateral prefrontal cortex (bilateral) and the superior frontal gyrus, related to performance monitoring and executive functions, the precuneus, part of the DMN, motor and sensorimotor areas, such as the precentral gyrus and the postcentral gyrus, the SMA, involved in motor initiation, and the thalamus (deep gray matter, part of motor system) on both sides, but more on the left. Considering the seed in the left precentral gyrus, in general fewer significant voxels are observed, compared to the previous case (seed in the right precentral gyrus). A difference is that in this case there is essentially nothing in the right thalamus, while the involvement of left thalamus is confirmed.

Brain areas	Voxels	Max intensity	Coordinates (Max)			Coordinates (COG)		
			x	y	z	x	y	z
Cingulate gyrus (anterior)	185	3.331	44	64	60	44.687	57.729	60.412
Cingulate gyrus (posterior)	187	3.124	48	51	60	44.770	52.726	60.872
Middle frontal gyrus	2438	4.026	30	68	65	41.197	70.060	58.703
Postcentral gyrus	3435	4.267	23	48	63	43.231	47.083	61.778
Precentral gyrus	2972	3.981	32	58	60	41.132	54.869	61.881
Precuneus cortex	690	3.538	54	21	50	42.694	30.691	58.548
Superior frontal gyrus	2468	4.026	30	68	65	41.533	70.428	59.518
Superior parietal lobe	2906	4.267	23	48	63	44.097	40.738	62.499
Supplementary motor cortex	263	3.331	44	64	60	44.706	55.957	61.435
Lateral occipital cortex (superior)	2679	3.913	59	38	63	41.773	27.945	55.600
Left thalamus	0	0.000	0	0	0	0.000	0.000	0.000
Right thalamus	0	0.000	0	0	0	0.000	0.000	0.000

Table 5.3: List of main brain areas showing a significant connectivity with the right SMA when comparing the ON state versus the OFF state (z-statistic map, from a 2 samples paired t-test, $p < 0.05$, cluster correction). Coordinates are given in voxels, referred to the MNI space; COG: Centre of Gravity.

Brain areas	Voxels	Max intensity	Coordinates (Max)			Coordinates (COG)		
			x	y	z	x	y	z
Cingulate gyrus (anterior)	447	3.445	44	63	64	43.437	61.024	57.818
Cingulate gyrus (posterior)	1960	3.872	51	43	34	44.677	40.550	48.340
Middle frontal gyrus	5130	4.503	61	58	61	41.385	70.741	57.600
Postcentral gyrus	4445	4.170	73	49	56	50.297	48.105	57.807
Precentral gyrus	4567	4.503	61	58	61	41.492	58.648	58.595
Precuneus cortex	5711	4.188	50	20	57	45.163	30.641	52.971
Superior frontal gyrus	4320	4.127	34	77	58	43.647	71.289	60.229
Superior parietal lobe	4168	4.118	73	48	57	48.425	38.493	61.063
Supplementary motor cortex	648	3.598	40	64	70	42.606	59.275	61.666
Lateral occipital cortex (superior)	9018	4.188	50	20	57	45.756	27.520	54.779
Left thalamus	456	3.871	50	44	35	51.978	48.856	40.080
Right thalamus	253	3.702	43	56	43	40.574	53.926	42.666

Table 5.4: List of main brain areas showing a significant connectivity with the left SMA when comparing the ON state versus the OFF state (z-statistic map, from a 2 samples paired t-test, $p < 0.05$, cluster correction). Coordinates are given in voxels, referred to the MNI space; COG: Centre of Gravity.

Anyhow, it is when the seed is placed in the right SMA that there is a smaller number of voxels showing significant differences between ON and OFF. There are no changes in the connectivity with thalamus, and also changes of lesser extent in the cingulate. If the seed is in the left SMA, on the other hand, significant variations of connectivity are more extensive, for example in the precuneus. Moreover, changes in thalamus functional connectivity are also present, both on left and right sides, but with more voxels on the left side.

We observe that as for the deep brain regions mainly involved in PD pathology (basal ganglia, such as caudate, putamen and pallidum, and thalamus), the thalamus is the only one where we found a variation in its connectivity with the sensorimotor network. There is also an asymmetry between right and left: it is in general in the left thalamus that we found major differences. We might speculate that this asymmetry may be related to the lateralization of disease onset. A similar, but opposed, asymmetry was also noticed by Esposito et al, [116], as they found that L-dopa significantly increased the participation of the right thalamus to the sensorimotor network. In their study, they considered early-stage PD patients, without separating them on the basis of the more affected side and with a slight predominance of left as symptom-dominant side. We also studied early-stage PD patients, with a slight predominance of right as symptom-dominant side (even if on small numbers). Esposito et. al performed a region of interest-based analysis of the sensorimotor network functional connectivity in the basal ganglia (anatomically subdivided into caudate, putamen and pallidum) and thalamus, and significant L-dopa-induced variations were found only in the thalamus, while for other regions they limited themselves to a descriptively analysis of an increased FC in all regions apart from the pallidum. A further analysis on our data might therefore be useful, focusing on region of interests placed in the basal ganglia and the thalamus itself. As mentioned above, differences between left and right sides may be related to the asymmetric onset of the disease, indeed in the early stage PD patients have one side of their body more affected. Remember that body sides are controlled by opposite cerebral hemispheres, therefore if a patient has his left body side more affected, then it is his right brain side actually that is more affected by PD impairments. Two of the PD patients considered so far are more affected in their left body side, while four in their right one. The small number of subjects doesn't allow us to consider two separated group on the basis of the more affected side. A possible way may be to flip the data in the left-right direction for the two subject more affected in the left side, so that to have a homogeneous group, but this step of the analysis needs more considerations and validations before being applied.

It seems that the brain areas that are more involved (i.e. connected with the seeds in primary and supplementary motor cortex) during the ON state rather than the OFF state may be ascribable to three brain networks: the sensorimotor , the dorsal-attention and the default mode.

The sensorimotor network deals with the integration of sensitive and motor stimuli, and has been shown to have characteristic activation in pre- and post-central gyri extending from the superior bank of the Sylvian fissure to the medial wall of the interhemispheric fissure and included the SMA, [36].

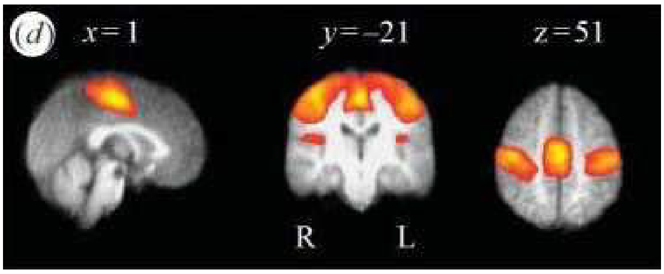

Figure 5.40: Orthographic views of the main areas involved in the sensorimotor network, [36]

The dorsal attention system, observed for the first time during resting state by Fox et al, [34] is involved in voluntary orientation and attention (for example it shows activity increases after presentation of cues indicating where, when, or to what subjects should direct their attention). Its main areas are the Intraparietal sulcus (IPS) and the Frontal Eye Field, junction of the precentral and superior frontal sulcus (FEF).

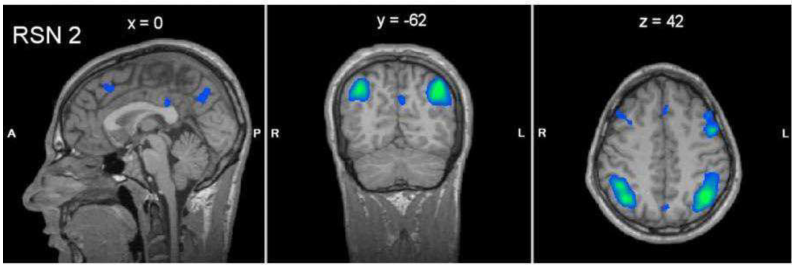

Figure 5.41: Orthographic views of the main areas involved in the dorsal attention network, [117]

The default mode network is described as the collection of brain structures that are particularly active during rest and deactivated when specific goal-directed behaviour is needed, [28]. Core regions associated with the brain's default network are the ventral medial prefrontal cortex, the posterior cingulate/retosplenial cortex, the inferior parietal lobule, the lateral temporal cortex, the dorsal medial prefrontal cortex, the hippocampal formation, [30]. Even if it is thought to be most active during the resting state, it may also persist during passive sensory processing states and one prevailing view is that the default mode involves retrieval and manipulation of past events, both personal and general, in an effort to solve problems and develop future plans. [118]

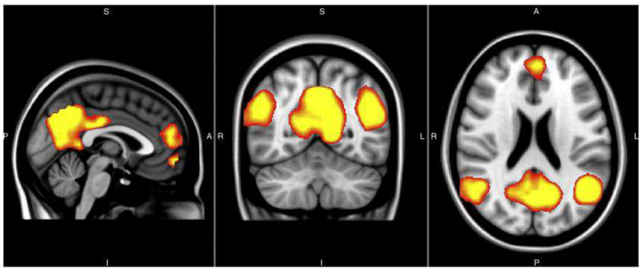

Figure 5.42: Orthographic views of the main areas involved in the default mode network, [37]

A possible interpretation of the fact that the DMN is more connected with primary and supplementary motor areas after the intake of L-dopa may be that the patients were more relaxed, and more ready to prepare and perform movements. In a recent study by Tessitore et al., [119] the default mode network in cognitively unimpaired PD was investigated. They found that PD patients, compared to controls, showed a decreased functional connectivity within the DMN (right medial temporal lobe and bilateral inferior parietal cortex). Anyhow, no significant correlation with L-dopa therapy was observed. On the other hand, Krajcovicova et al, [120] found that there were no differences in DMN integrity between PD on dopaminergic medication and healthy controls, suggesting therefore that dopaminergic therapy may have specific effects on default mode integrity, helping to relatively normalize activation within DMN in PD patients. Moreover, they also observed, when using the daily levodopa equivalent dose as a covariate, an increased functional connectivity of the DMN in the posterior cingulate cortex, that plays also a role in visuo-spatial orientation. This may be consistent with the fact the posterior division of the cingulate appears to be more connected with M1 and supplementary motor area after L-dopa intake, as an improvement towards motor preparation and execution.

Freezing, a typical PD symptom, is a sort of motor block due to a visible obstacle. Therefore it is also a condition related to visual perception. Usually it is not present at the early stage of the disease (indeed none of our patients presented this problems), and later it is typically more present when the patients are without medication (OFF state). From our results the hypothesis may arise: that freezing may be related to a dysfunction of the visuo-spatial network (related to the attentional areas, involving mainly the posterior parietal cortex and middle/inferior frontal gyrus), that is present even before the problem manifests itself. In a study by Tessitore et al., [121] attentional circuit in PD patients with and without freezing were analysed, founding a reduced activity in patients with freezing. This result supports our hypothesis.

A notable aspect of our results is that many structures of attentive and executive systems are also more connected with primary and supplementary motor areas after the intake of L-dopa, suggesting that dopaminergic medication may help PD patients with their executive dysfunction, giving them notable improvements in the cognitive, attentional and executive steps that are essential in the phase of preparation of a movement. Therefore medication with L-dopa also seems to have positive effects during rest, and not only during the performance of movements.

One of the first fMRI study of PD, [122], investigated activations and connectivity during the performance of tasks (a paced overlearned motor sequence task, with and without an additional attention task): motor and attentional structures were found to be primarily involved. Specifically, only in control subjects, and not in PD patients, an attentional modulation of connectivity was observed: the attention to action leads to further activations of prefrontal, parietal, para-cingulate cortex and SMA.

A later study by van Eimeren et al., [123], investigated dysfunctions of the default mode in PD patients. Their results show PD deficits in executive tasks, that include planning and set shifting: they observed less deactivation of posterior cingulate cortex and precuneus. This suggests a malfunctioning of the DMN during executive task in PD patients. It may be coherent with our finding that after the intake of L-dopa these areas are more connected with the sensorimotor system: subjects are more ready to execute and prepare and then perform movements

Studying PD patients not treated with dopaminergics or with any other type of drug therapy, Wu et al, [99], showed how the dopaminergic system exerts influences on widespread brain networks, including motor and cognitive networks. They showed that SNc (Substantia Nigra pars Compacta) has not only reciprocal influences with other BG nuclei, cortical motor areas, and brainstem, but also with the DMN, DLPFC, temporal cortex, and cerebellum. These connections are disordered in PD patients. A function of the dopaminergic system in the baseline condition seems to be to facilitate the motor preparation networks in order to prepare for the coming movements and to inhibit the motor execution networks to restrict the unnecessary movements. The dopaminergic system facilitates both motor preparation and execution networks to maintain motor execution. The SNc had decreased connectivity with the striatum, globus pallidus, subthalamic nucleus, thalamus, SMA, dorsolateral prefrontal cortex, insula, default mode network, temporal lobe, cerebellum,and pons in patients compared to controls. Levodopa administration partially normalized the pattern of connectivity.

Hacker et al., [124], investigate the functional connectivity of the striatum in patients with advanced PD by means of resting state fMRI. They reported markedly lower striatal correlations with thalamus, midbrain, pons and cerebellum, and differences between PD patients and controls were also observed in striatal correlations with the cerebral cortex principally in sensorimotor and visual region. These same regions also exhibited reduced cortico-cortical functional connectivity. The topography of the affected regions plausibly corresponds to the clinical manifestations of Parkinson's disease, which is primarily a movement disorder with associated executive deficits and visual disturbances.

Changes in functional connectivity of cortical somato-sensory and motor regions were also found by Helmich et al., [125]. Also Sharman et al, [100], reported deficits in sensorimotor connections. They found a decreased functional connectivity between SN and striatum, and between SN and thalamus, but increased FC in the associative and limbic connections and in the cortico-basal ganglia thalamo-cortical circuits, that may be hypothesised to be compensatory effects.

The role of attentional control network was investigated in PD by Shine et al, [126], and they found confirmations to the hypothesis that visual misperceptions and hallucinations, typical symptoms of PD, may arise from disrupted processing across attentional networks. The patients with stronger misperceptions were less able to activate frontal and parietal hubs of the dorsal attention network.

Esposito et. al. [116], studying functional connectivity changes within the sensorimotor resting state network in drug-naive patients with Parkinson's disease after acute levodopa administration, showed that at the anatomical level, levodopa enhanced the sensorimotor network functional connectivity in the supplementary motor area (where drug-naive patients exhibited reduced signal fluctuations) and that at the spectral frequency level, levodopa stimulated these fluctuations in a selective frequency band of the sensorimotor network. They did not observe any compensatory effects in other regions of sensorimotor network, assuming that maybe the compensatory effects may arise only during motor performance and not while at rest.

Wu and his group have been studying brain connectivity in Parkinson's disease patients in the recent years. In 2009 they carried out a functional MRI study [98] that with a network model based on graph theory measured functional connectivity of brain motor network during the resting state. They found that PD patients had decreased functional connectivity in the SMA, left dorsal lateral prefrontal cortex and left putamen, and had increased functional connectivity in the left cerebellum, left primary motor cortex, and left parietal cortex before taking L-dopa, compared to normal subjects. Administration of levodopa relatively normalized the pattern of functional connectivity in PD patients and the functional connectivity in most of regions in the motor network correlated with the Unified Parkinson's Disease Rating Scale motor score in the patients. In a follow-up study [89] they investigated functional connectivity of brain networks in the resting state in PD choosing the rostral SMA (pre-SMA, important in motor preparation) and bilateral primary motor cortex (M1, critical in motor execution) as "seed" regions and found that, in the resting state, the pattern of connectivity with these regions was changed. Connectivity of the pre-SMA in patients with PD compared to normal subjects was increased with right M1 and decreased with the left putamen, right insula, right premotor cortex, and left inferior parietal lobule, while they only found stronger connectivity in the M1 with its own local region in patients with PD compared to controls.

Litvak et al [127] used techniques other than fMRI, such as MEG and subthalamic local field potential recordings, to investigate resting connectivity in PD patients, the main findings being relative to the attentional and execution functions. Litvak et al observed two major spatio-temporal patterns of coupling between the cerebral cortex and subthalamic nuclei: one in the α frequency band and one in the β frequency band. The former showed a coherence between subthalamic area and bilateral temporo-parietal cortex and brainstem, and is therefore likely to have an attentional role. The latter involved the subthalamic area and ipsilateral anterior parietal and frontal cortices, and is likely to be involved in setting executive functions. Dopaminergic medication increased this β coherence between subthalamic regions and the prefrontal cortex.

Compared to what is reported in literature, we found limited variations in functional connectivity with SMA and no variations in connectivity between sensorimotor areas and deep brain regions involved in PD, except for the thalamus. Possible hypothesis to explain these aspects may be methodological differences and differences in patients studied: different techniques and methods (some focusing on the general pattern of brain connectivity, others on connectivity with specific brain areas) were used to analyse fMRI data in different studies and our group of patients was very homogeneous (all in a preliminary stage of the disease).

Chapter 6

Conclusions and future developments

Summing up the main findings of our fMRI data analysis, we can say that the pre-processing step of correcting physiological-related noise worked satisfactorily, providing significant improvements of TSNR, with greater extent in the areas that according to the literature are more likely to be affected by this kind of disturbance.

As for functional connectivity in PD patients, brain cortical areas that are more connected with primary and supplementary motor cortex during the ON state rather than the OFF state may be ascribable to three brain networks: the sensorimotor, involved in the integration of sensitive and motor stimuli, the dorsal-attention, that deals with voluntary orientation and attention, and the default mode, that is particularly active during rest and deactivated when goal-specific behaviour is necessary. This may suggest that L-dopa also has positive effects during rest (and not only during motor performance), in particular activating attentive and executive brain areas, in relation to the sensorimotor circuit. After the intake of L-dopa patients seem to be more relaxed, and more ready to prepare and perform movements. We might also speculate that freezing may be related to a dysfunction of the visuo-spatial network (related to the attentional areas) that is present even before that the problem manifests itself.

The thalamus is the only deep brain region in which we found a variation in connectivity with the sensorimotor network, with a lateral asymmetry: it is in general in the left thalamus that we found major differences. It is tempting to speculate that this asymmetry may be related to PD asymmetrical onset.

As far as our analysis is concerned, developments and possible improvements have been suggested by the results of the analysis itself. First, we may consider the possibility of flipping brain imaging data in the left-right direction in order to uniform our data according to the most affected brain side. Then, we may perform similar analysis focusing on deep brain regions, such as basal ganglia and thalamus, as regions of interest.

Further steps of the study will be the comparison and the combination of these fMRI results with the results of EEG data analysis. As the use of EEG-fMRI with PD patients is a novel approach, a standard and well defined method to combine them does not yet exist. It will be determined in collaboration with the research groups of Prof. P.Tinuper (IRCSS) and of Prof. E.Magosso (Biomedical Engineering).

When working with EEG, information about functional interaction between neural systems, i.e.connectivity, are typically provided by the investigation of coherence, that can be understood as a measure of synchronization between two signals. Coherence is defined as a correlation coefficient that estimates the phase consistency between pairs of signals with a specific frequency band. It is typically computed between two signals recorded simultaneously at different locations on the scalp. Two areas are said connected when the signals of corresponding electrodes show loose coherence, i.e. synchrony.

The EEG channels that should correspond to motor area are C3 and C4. In particular, referring to the seeds used in fMRI analysis, they may correspond to the precentral gyrus (more superficially) and SMA (deeper and more medial).

Some of the possible approaches are briefly outlined below. A first simple step may be comparing C3 and C4 coherence, before and after L-dopa intake, discussing eventual findings in relation to fMRI results. Moreover, fMRI results may somehow guide EEG analysis, leading it to focus mainly on channels that are located within areas compatible with the brain network individuated by fMRI. Using the data from the 64 channel cap we can solve the inverse problem, in order to obtain information about neural sources within the brain. In this case, the inverse problem may be performed by using patients' structural images registered to MNI rather than standard brains, and its findings may be compared and combined with fMRI results.

Appendices

Appendix A

Independent component analysis and fMRI data

The independent component analysis (ICA) of a random vector consists of searching for a linear transformation that minimizes the statistical dependence between its components. The concept of ICA may actually be seen as an extension of the principal component analysis (PCA), imposing independence up to the second order and, consequently, defines directions that are orthogonal.

The fMRI measured signal may be produced by different time-varying phenomena (such as brain metabolism, physiological noise, movements..), this can be conceptualized as multiple concurrent "component processes" each having a separate time course and spatial extent and each producing simultaneous changes in the fMRI signals of many voxels, [11]. These separate processes may be represented by one or more spatially-independent components, each associated with a single time course of enhancement and/or suppression and a component map.

It is assumed that the component maps represent possibly overlapping, multifocal brain areas of statistically dependent fMRI signal influence. Furthermore, we presume that the component map distributions are spatially independent: if $p_k(C_k)$ is the probability distribution of the voxel values C_k in the k^{th} component map, then the joint probability distribution of all n components factorizes:

$$p(C_1, C_2, ..., C_n) = \prod_{k=1}^{n} p_k(C_k) \tag{A.1}$$

where each of the component maps C_k is a vector $(C_{ki}, i = 1, 2, ...M)$, and M is the number of voxels.

It is also assumed that the observed fMRI signals are the linear sum of the contributions of the individual component processes at each voxel, [50].

A matrix equation relating the component maps and their time courses to the measured fMRI signals can be written: supposing that map voxel values for each of the components are known and placed in separate rows of matrix C_{ki} then a mixing matrix, M_{jk}, can specify the time-varying contributions of each component map to the measured fMRI signals

$$X_{ji} = \sum_{k=1}^{N} M_{jk} C_{ki} \tag{A.2}$$

Decomposing observed fMRI signals into statistically independent component maps without prior knowledge of their spatial extents or time courses of activation is a "blind separation" problem. The algorithm proposed by Bell and Sejnowski in 1995 is an iterative unsupervised neural network learning algorithm and can perform blind separation of input data into the linear sum of time-varying modulations of maximally independent component maps. It iteratively determines the unknown unmixing matrix $\mathbf{W}$, a possibly linearly scaled and permuted version of the inverse of the mixing matrix, $\mathbf{M}$, from which the component maps and time courses can be computed.

The matrix of component maps is computed through the product $\mathbf{C} = \mathbf{XW}$ in matrix notation, where $\mathbf{X}$ is the fMRI signal data matrix, $\mathbf{W}$ is the unmixing matrix, and $\mathbf{C}$ is the matrix of component map voxel values. Reconstruction of the data from the independent components is accomplished by $\mathbf{X}' = \mathbf{W}^{-1}\mathbf{C}$. Note that $\mathbf{W}$ is a square matrix of full rank, so its inverse $\mathbf{W}^{-1}$ is well-defined. The first column of $\mathbf{W}^{-1}$ gives the time course of modulation of the first component map, the second column gives the time course of the second component map, and so on. Each ICA component map is described by a distribution of values, one for each voxel. These values represent the relative amount a given voxel is modulated by the activation of that component.

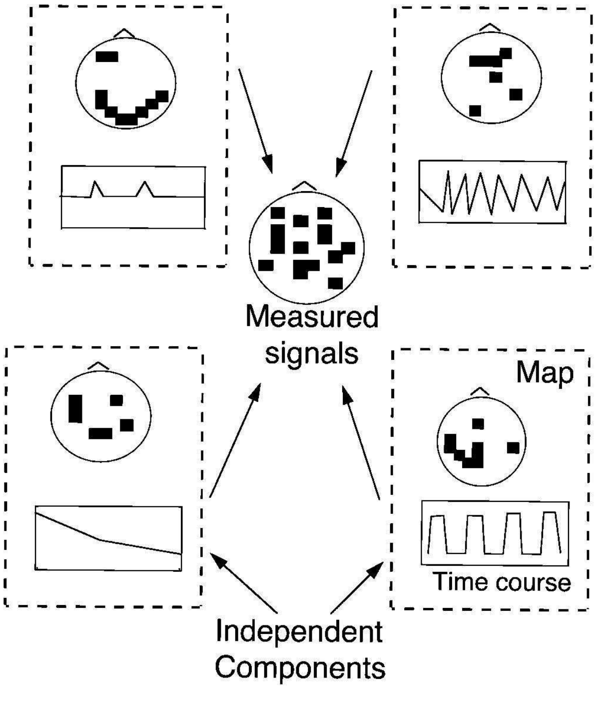

Figure A.1: Schematic of fMRI data decomposed into independent components, [11].

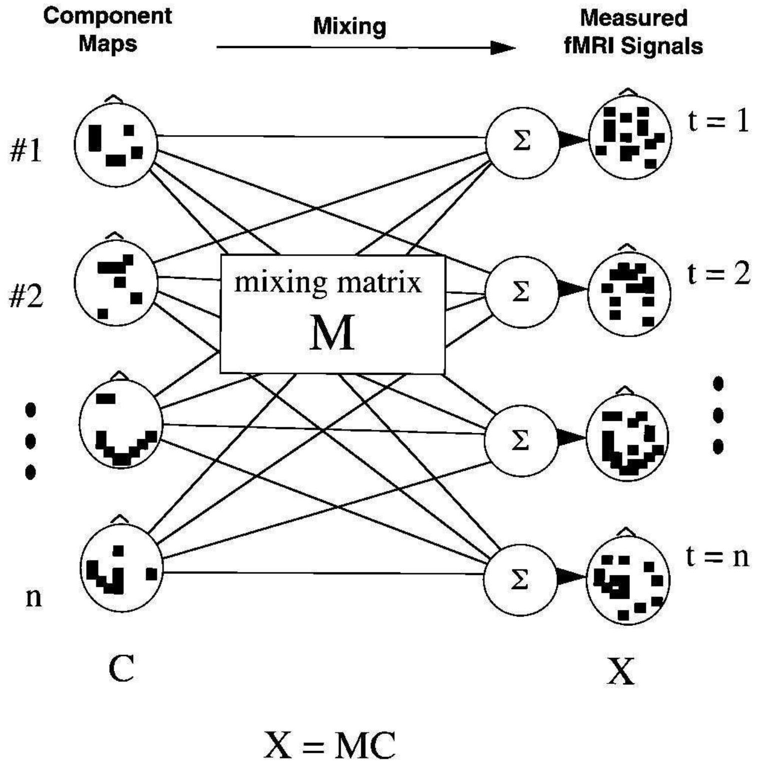

Figure A.2: fMRI data as a mixture of independent components, [11].

Appendix B

List of abbreviations and main variables

List of abbreviations

AAS	Average Artefact Subtraction
AFNI	Analysis of Functional NeuroImages
APPLECOR	Affine Parameterization of Physiological Large-scale Error Correction
ATP	Adenosine Tri-Phosphate
BCG	BalistoCardioGram
BG	Basal Ganglia
BOLD	Blood Oxygen Level Dependant
CBF	Cerebral Blood Flow
CBV	Cerebral Bloow Volume
$CMRO_2$	Cerebral Metabolic Rate of Oxygen utilization
COMT	Catechol-O-methyl transferase
CORSICA	CORrection of Structured noise using spatial Independent Component Analysis
CSF	Cerebro-Spinal Fluid
CT	Computed Tomography
Dartel	Diffeomorphic Anatomical Registration Through Exponentiated Lie Algebra
DMN	Default Mode Network
DICOM	Digital Imaging and Comunication in Medicine
DN	Dendate Nucleus
DOF	Degree Of Freedom
DTI	Diffusion Tensor Imaging
ECG	Electrocardiogram
EEG	Electroencefalogram

EMF	Electromotive Forces
EPSP	Excitatory Post-Synaptic Potential
EPI	Echo Planar Imaging
ERP	Event Related Potential
EV	Explanatory Variable
FC	Functional Connectivity
FDR	False Discovery Rate
FOV	Field Of View
FMRIB	Functional Magnetic Resonance Imaging of the Brain
FSL	FMRIB Software Library
FWHM	Full Width ad Half Maximum
GLM	General Linear Model
GRF	Gaussian Random Field
HARDI	High Angular Resolution Diffusion Imaging
Hb	Haemoglobing
HRF	Haemodynamic Response Function
ICA	Independent Component Analysis
IPSP	Inhibitor Post Synaptic Potential
fMRI	functional Magnetic Resonance Imaging
L-dopa	Levodopa
M1	Primary motor cortex
MAO	Monoamine Oxidase
MCA	Middle Cerebral Artery
MEG	MagneticEncefaloGram
MNI	Montreal Neurological Institute
NIFTI	Neuroimaging Informatics Technology Initiative
NV	Number of Voxels
PA	Pulse Artefact
PD	Parkinson’s Disease
PESTICA	Physiologal Estimation by Temporal ICA
PHYCAA	PHYsiological correction using Canonical Autocorrelation Analysis
RETROICOR	RETROspective Image-based CORrection
RF	Radio Frequency
RVHRcor	Respiration Volume and Heart Rate correction
PE	Parameter Estimate
PET	Positron Emission Tomography
PMC	Pre Motor Cortex
ROI	Region of Interest
RVT	Respiratory Volume per Time
SMA	Supplementary Motor Area
SN	Substantia Nigra
SNc	Substantia Nigra pars Compacta
SNR	Signal to Noise Ratio

SPECT	Single Photon Emission Computed Tomography
SPM	Statistical Parametric Mapping
SSE	Sum of Squares Error
STN	Sub-thalamica nucleus
TE	Echo Time
TMS	Transcranial Magnetic Stimulation
TR	Repetition Time
TSNR	Temporal Signal to Noise Ratio
UPDRS	Unified Parkinson's Disease Rating Scale
VBM	Voxel Based Morphometry

Main variables

B_0 : it is the static and homogeneous magnetic field used to polarize spins, creating magnetization. Its direction defines the longitudinal axis.

B_1 : it's the pulsed magnetic field (RF energy) used to perturb the magnetization: the spins respond to this pulse in such a way as to cause the net magnetization vector to rotate about the direction of the applied B_1 field. It is created by a coil passing an alternating current at the Larmor frequency.

T_1 : it's the time constant which describe how the longitudinal (i.e. with a direction parallel to the main magnetic field, B_0) magnetization return to its equilibrium value after a perturbation. It is also called spin-lattice relaxation time.

T_2 : it's the time constant which describes the return to equilibrium of the transverse magnetization (i.e. orthogonal to the direction of B_0). It is called the spin-spin relaxation time. The net magnetization starts to dephase because each of the spin packets making it up is experiencing a slightly different magnetic field and rotates at its own Larmor frequency.

T_2^* : two factors contribute to the decay of transverse magnetization: molecular interactions (pure T_2 molecular effect) and variations in B_0 (inhomogeneous T_2 effect). The combination of these two factors is what actually results in the decay of transverse magnetization and T_2^* is the combined time constant.

$k - space$: it's that image space (in the spatial frequency domain) represented by the time and phase raw data. The Fourier transform of k-space gives the magnetic resonance image. Its values are sampled during an MR measurement, in a premeditated scheme controlled by a pulse sequence, according to the frequency encoding and the phase encoding.

Bibliography

[1] P.Jezzard, P.M.Matthews, and S.M.Smith. *Functional MRI an introduction to methods.* Oxford University Press, 2001.

[2] R.B. Buxton. *Introduction to Functional Magnetic Resonance Imaging. Principles and Techniques.* Cambridge University Press, 2002.

[3] P. Callaghan. *Principles of nuclear magnetic resonance microscopy.* Oxford University Press, 1994.

[4] J.P. Hornak. *The basics of MRI.* Interactive Learning Software, 2011.

[5] J.J. Harris, C. Reynell, and D. Attwell. The physiology of developmental changes in BOLD functional imaging signals. *Developmental Cognitive Neuroscience*, 1(3):199 – 216, 2011.

[6] S.G.Kim and S. Ogawa. Biophysical and physiological origins of blood oxygenation level-dependent fMRI signals. *Journal of Cerebral Blood Flow and Metabolism*, 32(7):1188–1206, 2012.

[7] K.R. Thulborn, J.C. Waterton, P.M. Matthews, and G.K. Radda. Oxygenation dependence of the transverse relaxation time of water protons in whole blood at high field. *Biochimica and Biophysica Acta*, 714:265 – 270, 1982.

[8] S. Ogawa, T.M. Lee, A.R. Kay, and D.W. Tank. Brain magnetic resonance imaging with contrast dependent on blood oxygenation. *Proceedings of the National Academy of Science*, 87:9868 – 9872, 1990.

[9] S. Ogawa, R.S. Menon, D.W. Tank, S.G. Kim, H. Merkle, J.M. Ellermann, and K.Ugurbil. Functional brain mapping by blood onygenation level-dependent contrast magnetic resonance imaging. A comparison of signal characteristics with a biophysical model. *Biophysical Journal*, 64:803–812, 1993.

[10] K. J. Friston, A. Holmes, K. Worsley, J.B. Poline, C. Frith, and R. Frackowiak. Statistical parametric maps in functional imagin: a general linear approach. *Human brain mapping*, 2:189 – 210, 1995.

[11] M.J. McKeown, S. Makeig, G.G. Brown, T.P. Jung, S.S. Kindermann, A.J. Bell, and T.J. Sejnowski. Analysis of fMRI Data by Blind Separation. *Human Brain Mapping*, 6:160 – 188, 1998.

[12] K. R. Van Dijk, T. Hedden, A. Venkataraman, K. C. Evans, S. W. Lazar, and R. L. Buckner. Intrinsic Functional Connectivity As a Tool For Human Connectomics: Theory, Properties, and Optimization. *Journal of Neurophysiology*, 103:297 – 321, 2010.

[13] K. J. Friston. Functional and Effective Connectivity in Neuroimaging: A Synthesis. *Human Brain Mapping*, 2:56 – 78, 1994.

[14] K. J. Friston, C. D. Frith, P. F. Liddle, and R. S. Frackowiak. Functional connectivity: the principal-component analysis of large (PET) data sets. *Journal of cerebral blood flow metabolism*, 13:5–14, 1993.

[15] B. Biswal, F. Z. Yetkin, V. M. Haughton, and J. S. Hyde. Functional connectivity in the motor cortex of resting human brain using echo-planar mri. *Magnetic Resonance in Medicine*, 34:537–541, 1995.

[16] D. J. Felleman and D. C. Van Essen. Distributed hierarchical processing in the primate cerebral cortex. *Cerebral Cortex*, 1:1 – 47, 1991.

[17] E. G. Jones and T. P. Powell. An anatomical study of converging sensory pathways within the cerebral cortex of the monkey. *Brain*, 93:793 – 820, 1970.

[18] L. G. Ungerleider and J.V. Haxby. "What" and "where" in the human brain. *Current Opinion in Neurobiology*, 4:157 – 165, 1994.

[19] N. Geschwind. Disconnexion syndromes in animals and man. Part 1. *Brain*, 88:237 – 294, 1965.

[20] A. Burkhalter, K. L. Bernardo, and V. Charles. Development of local circuits in human visual cortex. *Journal of Neuroscience*, 13:1916 – 1931, 1993.

[21] B. Horwitz, R. Duara, and S.I. Rapoport. Intercorrelations of glucose metabolic rates between brain regions: application to healthy males in a state of reduced sensory inout. *Journal of Cerebral Blood Flow and Metabolism*, 4:484 – 499, 1984.

[22] P. M. Gochin, E. K. Miller, C. G. Gross, and G. L. Gerstein. Functional interactions among neurons in inferior temporal cortex of the awake macaque. *Experimental Brain Research*, 84:505 – 516, 1991.

[23] B. Biswal, A. G. Hudetz, t. Z. Yetkin, t. M. Haughton, and J. S. Hyde. Hypercapnia Reversibly Suppresses Low-Frequency Fluctuations in the Human Motor Cortex During Rest Using Echo-Planar MRI. *Journal of Cerebral Blood Flow and Metabolism*, 17:301 – 308, 1997.

[24] K. Arfanakis J.D. Carew P. A. Turski C. H. Moritz M. A. Quigley M. e. Meyerand D.Cordes, V. M. Haughton. Frequencies Contributing to Functional Connectivity in the Cerebral Cortex in ”Resting-state” Data. *American Journal of Neuroradiology*, 22:1326 – 1333, 2001.

[25] M. J. Lowe, B. J. Mock, and J. A. Sorenson. Functional Connectivity in Single and Multislice Echoplanar Imaging Using Resting-State Fluctuations. *NeuroImage*, 7:119 – 132, 1998.

[26] S. J. Peltier and D.C. Noll. T2* Dependence of Low Frequency Functional Connectivity. *NeuroImage*, 16(4):985 – 992, 2002.

[27] M. D. Fox and M. E. Raichle. Spontaneous fluctuations in brain activity observed with functional magnetic resonance imaging. *Nature Reviews Neuroscience*, 8:700–711, 2007.

[28] J. S. Damoiseaux, S. A. R. B. Rombouts, F. Barkhof, P. Scheltens, C. J. Stam, S. M. Smith, and C. F. Beckmann. Consistent resting-state networks across healthy subjects. *Proceedings of the National Academy of Sciences*, 103(37):13848 – 13853, 2006.

[29] M. De Luca, C. F. Beckmann, N. De Stefano, P. M. Matthews, and S. M. Smith. FMRI resting state networks define distinct modes of long-distance interactions in the human brain. *NeuroImage*, 29:1359 – 1367, 2006.

[30] R.L. Buckner, J.R. Andrews-Hanna, and D.L. Schaxter. The Brain’s Default Network Anatomy, Function, and Relevance to Disease. *Annals of the New York Academy of Sciences*, 1124:1 – 38, 2008.

[31] J.L Vincent, A.Z Snyder, M.D. Fox, B.J. Shannon, J.R. Andrews, M.E. Raichle, and R.L. Buckner. Coherent spontaneous activity identifies a hippocampal-parietal memory network. *Journal of Neurophysiology*, 96(6):3517 – 3531, 2006.

[32] M. Hampson, B. S. Peterson, P. Skudlarski, J. C. Gatenby, and J. C. Gore. Detection of Functional Connectivity Using Temporal Correlations in MR Images. *Human Brain Mapping*, 15:247 – 262, 2002.

[33] M. D. Fox, A. Z. Snyder, J. L. Vincent, M. Corbetta, D. C. Van Essen, and M. E. Raichle. The human brain is intrinsically organized into dynamic, anticorrelated functional networks. *Proceedings of the National Academy of Sciences*, 102(27):9673 – 9678, 2005.

[34] M. D. Fox, M. Corbetta, A. Z. Snyder, J. L. Vincent, and M. E. Raichle. Spontaneous neuronal activity distinguishes human dorsal and ventral attention systems. *Proceedings of the National Academy of Sciences*, 103(26):10046 – 10051, 2006.

[35] J. L. Vincent, I. Kahn, A. Z. Snyder, M. E. Raichle, and R. L. Buckner. Evidence for a Frontoparietal Control System Revealed by Intrinsic Functional Connectivity. *Journal of Neurophysiology*, 100:3328 – 3342, 2008.

[36] C.F. Beckmann, M. DeLuca, J. T. Devlin, and S. M. Smith. Investigations into resting-state connectivity using independent component analysis. *Philolophical Transactions of the Royal Society B: Biological Sciences*, 360:1001–1013, 2005.

[37] A. Hafkemeijer, J. Van Der Grond, and S.A.R.B. Rombouts. Imaging the default mode network in aging and dementia . *Biochimica et Biophysica Acta*, 1822:431 – 441, 2012.

[38] J. S. Damoiseaux and M. D. Greicius. Greater than the sum of its parts: A review of studies combining structural connectivity and resting-state functional connectivity. *Brain Structure and Function*, 213:525 – 533, 2009.

[39] D.A. Leopold, Y. Murayama, and N.K. Logothetis. Very slow activity fluctuations in monkey visual cortex: implications for functional brain imaging. *Cerebral Cortex*, 13:423 – 433, 2003.

[40] H.Laufs, K. Krakow, P.Sterzer, E. Eger, A. Beyerle, A. Salek-Haddadi, and A. Kleinschmidt. Electroencephalographic signatures of attentional and cognitive default modes in spontaneous brain activity fluctuations at rest. *Proceedings National Academy of Sciences*, 100(19):11053 – 11058, 2003.

[41] A. Shmuel, M. Augath, A. Oeltermann, and N.K. Logothetis. Spontaneous fluctuations in functional MRI signal reflect fluctuations in the underlying neuronal activity. *Neuroimage: 13th annual meeting of the organization for human brain mappping*, 36:s58, 2007.

[42] S. Vanhatalo, J.M. Palva, M.D. Holmes, J.W. Miller, J. Voipio, and K. Kaila. Infraslow oscillations modulate excitability and interictal epileptic activity in the human cortex during sleep. *Proceedings of the National Academy of Sciences*, 101:5053 – 5057, 2004.

[43] D. Deitcher and. Distinct requirements for evoked and spontaneous release of neurotransmitter are revealed by mutations in the Drosphila gene neuronal-synaptobrevin. *Journal of neuosciences*, 18:2028 – 2039, 1998.

[44] J.M. Johnston, S.N. Vaishnavi, M.D. Smyth, D.Y. Zhang, B.J. He, J.M. Zempel, J.S. Shimony, A.Z. Snyder, and M.E. Raichle. Loss of resting interhemispheric functional connectivity after complete section of the corpus callosum. *Journal of neurosciences*, 28:6453 – 6458, 2008.

[45] J.L. Vincent, G.H. Patel, M.D. Fox, A.Z. Snyder, J.T. Baker, D.C. Van Essen, J.M. Zempel, L.H. Snyder, M. Corbetta, and M.E. Raichle. Intrinsic

functional architecture in the anesthetized monkey brain. *Nature*, 447:83 –86, 2007.

[46] C.J. Honey, O.Sporns, L. Cammoun, X. Gigandet, J.P. Thiran, R.Meuli, and P.Hagmann. Predicting human resting-state functional connectivity from structural connectivity. *Proceedings of the National Academy of Sciences*, 106:2035 – 2040, 2009.

[47] R.L. Buckner, J. Sepulcre, T. Talukdar, F.M. Krienen, H.Liu, T.Hedden, J.R. Andrews-Hanna, R.A. Sperling, and K.A. Johnson. Cortical hubs revealed by intrinsic functional connectivity: mapping, assessment of stability, and relation to Alzheimer's disease. *Journal of Neurosciences*, 29:1860 –1873, 2009.

[48] D.Cordes, V. M. Haughton, J.D. Carew, K. Arfanakis, and K. Maravilla. Hierarchical clustering to measure connectivity in fMRI resting-state data. *Magnetic Resonance Imaging*, 20:305 – 317, 2002.

[49] S. Achard, R. Salvador, B. Whitcher, J. Suckling, and E. Bullmore. A resilient, low-frequency, small-world human brain functional network with highly connected association cortical hubs. *Journal of Neuorsciences*, 26:63 – 72, 2006.

[50] M.J. McKeown and T.J. Sejnowski. Independent Component Analysis of fMRI Data: Examining the Assumptions. *Human Brain Mapping*, 6:368 – 372, 1998.

[51] S. M. Smith, P. T. Fox, K. L. Miller, D. C. Glahn, P. M. Fox, C. E. Mackay, N. Filippini, K. E. Watkins, R. Toro, A. R. Laird, and C. F. Beckmann. Correspondence of the brain's functional architecture during activation and rest. *Proceedings of the National Academy of Sciences*, 106(31):13040 – 13045, 2009.

[52] M. S. Dagli, J. E. Ingeholm, and J. V. Haxb. Localization of Cardiac-Induced Signal Change in fMRI. *NeuroImage*, 9:407 – 415, 1999.

[53] C. Chang, J. P. Cunningham, and G. H. Glover. Influence of heart rate on the BOLD signal: The cardiac response function. *NeuroImage*, 44:857 – 869, 2009.

[54] K. Shmueli, P. van Gelderen, J. A. de Zwart, S. G. Horovitz, M. Fukunaga, J. M. Jansma, and J. H. Duyn. Low-frequency fluctuations in the cardiac rate as a source of variance in the resting-state fMRI BOLD signal. *NeuroImage*, 38:306 – 320, 2007.

[55] A. G. Hudetz, B. B. Biswal, H. Shen, K. K. Lauer, and J. P. Kampine. Spontaneous fluctuations in cerebral oxygen supply. *Advances in Experimental Medicine and Biology*, 454:551 – 559, 1998.

[56] D. Raj, A.W. Anderson, and J.C. Gore. Respiratory effects in human functional magnetic resonance imaging due to bulk susceptibility changes. *Physics in Medicine and Biology*, 46:3331–3340, 2001.

[57] D. Raj, D. P. Paley, A. W. Anderson, R. P. Kennan, and J. C. Gore. A model for susceptibility artefacts from respiration in functional echo-planar magnetic resonance imaging . *Physics in Medicine and Biology*, 45:3809–3820, 2000.

[58] R. M. Birn, J. B. Diamond, M. A. Smith, and P. A. Bandettini. Separating respiratory-variation-related fluctuations from neuronal-activity-related fluctuations in fMRI. *NeuroImage*, 31:1536 – 1548, 2006.

[59] R. G. Wise, K. Ide, M. J. Poulin, and I. Tracey. Resting fluctuations in arterial carbon dioxide induce significant low frequency variations in BOLD signal. *NeuroImage*, 21:1652 – 1664, 2004.

[60] M. Modarreszadeh and E. N. Bruce. Ventilatory variability induced by spontaneous variations of PaCO2. *Journal of Applied Physiology*, 76:2765 – 2775, 1994.

[61] G. Kruger and G.H. Glover. Physiological Noise in Oxygenation-Sensitive Magnetic Resonance Imaging. *Magnetic Resonance in Medicine*, 46:631 – 637, 2001.

[62] W.A. Edelstein, G.H. Glover, C.J. Hardy, and R.W. Redington. The intrinsic signal-to-noise ratio in NMR imaging. *Magnetic Resonance in Medicine*, 3:604 – 618, 1986.

[63] K.-H. Chuang and J.-H. Chen. IMPACT: Image-based physiological artifacts estimation and correction technique for functional MRI. *Magnetic Resonance in Medicine*, 46:344 – 353, 2001.

[64] B. Biswal, E. A. DeYoe, and J. S. Hyde. Reduction of physiological fluctuations in fMRI using digital filters. *Magnetic Resonance in Medicine*, 35:107–113, 1996.

[65] X. Hu and S. G. Kim. Reduction of signal fluctuation in functional MRI using navigator echoes. *Magnetic Resonance in Medicine*, 31:495 – 503, 1994.

[66] G. H. Glover and S. Lai. Self-navigated spiral fMRI: Interleaved versus single-shot. *Magnetic Resonance in Medicine*, 39:361 – 368, 1998.

[67] B. Wowk, M. C. McIntyre, and J. K. Saunders. K-space detection and correction of physiological artifacts in fMRI. *NeuroImage*, 11:1997, 1997.

[68] X. Hu, T. H. Le, T. Parrish, and P. Erhard. Retrospective estimation and correction of physiological fluctuation in functional MRI. *Magnetic Resonance in Medicine*, 34:201 – 212, 1995.

[69] G. H. Glover, T.-Q. Li, and D. Ress. Image-based method for retrospective correction of physiological motion effects in fMRI: RETROICOR. *Magnetic Resonance in Medicine*, 44:162 – 167, 2000.

[70] O. Josephs, A. M. Howseman, K. J. Friston, and R. Turner. Physiological noise modelling for multi-slice epi fmri using spm. In *Proceedings of the International Society for Magnetic Resonance in Medicine*, page 1682, Vancouver, B.C., Canada, 1997.

[71] R. M. Birn, K. Murphy, and P. A. Bandettini. The effect of respiration variations on independent component analysis results of resting state functional connectivity. *Human Brain Mapping*, 29:740 – 750, 2008.

[72] E. B. Beall and M. J. Lowe. Isolating physiologic noise sources with independently determined spatial measures. *NeuroImage*, 37:1286 – 1300, 2007.

[73] E. B. Beall and M. J. Lowe. The non-separability of physiologic noise in functional connectivity MRI with spatial ICA at 3T. *Journal of Neuroscience Methods*, 191(2):263 – 276, 2010.

[74] H. J. Jo, Z.S. Saad, W. K. Simmons, L. A. Milbury, and R. W. Cox. Mapping sources of correlation in resting state FMRI, with artifacts detection and removal. *Neuroimage*, 52:571 – 582, 2010.

[75] A. Weissenbacher, C. Kasess, F. Gerstl, R. Lanzenberger, E. Moser, and C. Windischberger. Correlations and anticorrelations in resting-state functional connectivity MRI: A quantitative comparison of preprocessing strategies. *NeuroImage*, 47:1408 – 1416, 2009.

[76] Z. S. Saad, S. J. Gotts, K. Murphy, G. Chen, H. J. Jo, A. Martin, and R. W. Cox. Trouble at Rest: How Correlation Patterns and Group Differences Become Distorted After Global Signal Regression. *Brain Connectivity*, 2(1), 2012.

[77] N. W. Churchill, G. Yourganov, R. Spring, P. M. Rasmussen, W. Lee, J. E. Ween, and S. C. Strother. PHYCAA: Data-driven measurement and removal of physiological noise in BOLD fMRI. *NeuroImage*, 59:1299 – 1314, 2012.

[78] M. Marx, K. B. Pauly, and C. Chang. A novel approach for global noise reduction in resting-state fMRI: APPLECOR. *NeuroImage*, 64:19 – 31, 2013.

[79] E. Niedermeyer and F. Lopes da Silva. *Electroencephalography: Basic Principles, Clinical Applications, and Related Fields.* Urban and Schwarzenberg, 1982.

[80] A. Brovelli. Basi fisiologiche dei segnali biologici complessi. Università degli Studi di Trieste, 2012.

[81] L. Lemieux, A. Salek-Haddadi, O. Josephs, P. Allen, N. Toms, C. Scottand, K. Krakow, R. Turner, and D.R. Fish. Event-Related fMRI with Simultaneous and Continuous EEG: Description of the Method and Initial Case Report . *NeuroImage*, 14:780 – 787, 2001.

[82] Brain products manual of instruction and articles. Brain Products GmbH, 2012.

[83] L. Lemieux, P.J. Allen, F. Franconi, M.R. Symms, and D.R. Fish. Recording of EEG during fMRI Experiments: Patient Safety. *Magnetic Resonance in Medicine*, 38:943 – 952, 1997.

[84] P.J. Allen, G. Polizzi, K. Krakow, D.R. Fish, and L. Lemieux. Identification of EEG events in the MR scanner: the problem of pulse artifact and mtehod for its subtraction. *Neuroimage*, 8:229 – 239, 1997.

[85] P.J. Allen, O. Josephs, and R. Turner. A method for removing imaging artifact from continuous EEG recorded during functional MRI. *Neuroimage*, 12:230 – 239, 2000.

[86] M. Ullsperger and S. Debener. *Simultaneous EEG and fMRI: Recording, Analysis and Application.* Oxford University Press, 2010.

[87] K. Mullinger, S. Debener, R. Coxon, and R. Bowtell. Effects of simultaneous EEG recording on MRI data quality at 1.5, 3 and 7 tesla. *International Journal of Psychophysiology*, 67:178 – 188, 2008.

[88] H. Simon and D. Zieve. Parkinson's disease | university of maryland medical center, 2012. url:http://umm.edu/health/medical/reports/articles/parkinsons-disease.

[89] T. Wu, X. Long, L. Wang, M. Hallett, Y. Zang, K. Li, and P. Chan. Functional Connectivity of Cortical Motor Areas in the Resting State in Parkinson's Disease. *Human Brain Mapping*, 32:1443 – 1457, 2011.

[90] S. Baudrexel, T. Witte, C. Seifried, F. von Wegner, F. Beissner, J.C. Klein, H. Steinmetz, R. Deichmann, J. Roeper, and R. Hilker. Resting state fMRI reveals increased subthalamic nucleus–motor cortex connectivity in Parkinson's disease. *NeuroImage*, 55:1728 – 1738, 2011.

[91] C. Buhmann, V. Glauche, H.J. Sturenburg, M. Oechsner, C. Weiller, and C. Buchel. Pharmacologically modulated fMRI-Cortical responiveness to levodopa in drug-naive hemiparkinsonian patients. *Brain*, 126:451–461, 2003.

[92] B. Haslinger, P. Erhard, N. Kampfe, H. Boecker, E. Rummeny, M. Schwaiger, B. Conrad, and A.O. Ceballos-Baumann. Event-related functional magnetic resonance imaging in Parkinson's disease before and after levodopa. *Brain*, 124:558 – 570, 2001.

[93] M. Jahanshahi, I.H. Jenkins, R.G. Brown, C.D. Marsden, R.E. Passingham, and D.J. Brooks. Self-initiated versus externally triggered movements. I. An investigation using measurement of regional cerebral blood flow with PET and movement-related potentials in normal and Parkinson's disease subjects. *Brain*, 118:913 – 933, 1995.

[94] E.D. Playford, I.H. Jenkins, R.E. Passingham, J. Nutt, R.S. Frackowiak, and D.J. Brooks. Impaired mesial frontal and putamen activation in Parkinson's disease: A positron emission tomography study. *Annals of Neurology*, 32:151 – 161, 1992.

[95] O. Rascol, U. Sabatini, N. Fabre, C. Brefel, I. Loubinoux, P. Celsis, J.M. Senard, J.L. Montastruc, and F. Chollet. The ipsilateral cerebellar hemisphere is overactive during hand movements in akinetic parkinsonian patients. *Brain*, 120:103 – 110, 1997.

[96] U. Sabatini, K. Boulanouar, N. Fabre, F. Martin, C. Carel, C. Colonnese, L. Bozzao, I. Berry, J.L. Montastruc, F. Chollet, and O. Rascol. Cortical motor reorganization in akinetic patients with Parkinson's disease: A functional MRI study. *Brain*, 123:394 – 403, 2000.

[97] T. Wu and M. Hallett. A functional MRI study of automatic movements in patients with Parkinson's disease. *Brain*, 128:2250 – 2259, 2005.

[98] T. Wu, L. Wang, Y. Chena, C. Zhaob, K. Li, and P. Chana. Changes of functional connectivity of the motor network in the resting state in Parkinson's disease. *NeuroImage*, 460:6 –10, 2009.

[99] T. Wua, J. Wang, C. Wang, M. Hallett, Y. Zangb, X. Wua, and P. Chana. Basal ganglia circuits changes in Parkinson's disease patients. *Neuroscience Letters*, 524:55 – 59, 2012.

[100] M. Sharman, R. Valabregue, V. Perlbarg, L. Marrakchi-Kacem, M. Vidailhet, H. Benali, A. Brice, and S. Lehéricy. Parkinson's Disease Patients Show Reduced Cortical-Subcortical Sensorimotor Connectivity. *Movement Disorders*, 28(4):447 – 454.

[101] R.W. Cox. AFNI: software for analysis and visualization of functional magnetic resonance neuroimages. *Computers and Biomedical Research*, 29(3):162 – 173, 1996.

[102] FSL course, 2012. fsl.fmrib.ox.ac.uk/fslcourse/physics+apps/spinal_pnm.pdf.

[103] T. B. Jones, P. A. Bandettini, and R. M. Birn. Integration of motion correction and physiological noise regression in fMRI. *NeuroImage*, 42:582 – 590, 2008.

[104] K. Murphy, J. Bodurka, and P.A. Bandettini. How long to scan? The relationship between fMRI temporal signal to noise ratio and necessary scan duration. *NeuroImage*, 34:565 – 574, 2007.

[105] M. Jenkinson and S.M. Smith. A global optimisation method for robust affine registration of brain images. *Medical Image Analysis*, 5(2):143 – 156, 2001.

[106] M. Jenkinson, P. Bannister, J.M. Brady, and S.M. Smith. Improved Optimisation for the Robust and Accurate Linear Registration and Motion Correction of Brain Images. *NeuroImage*, 17(2):825 – 841, 2002.

[107] J. Ashburner. A fast diffeomorphic image registration algorithm. *Neuroimage*, 38(1):95 – 113, 2007.

[108] C.M. Huang, S.H. Leec, I.T. Hsiao, W.C Kuan, Y.Y. Wai, H.J. Ko, Y.L. Wana, Y.Y. Hsu, and H.L. Liu. Study-specific EPI template improves group analysis in functional MRI of young and older adults. *Journal of Neuroscience Methods*, 189:257 – 266, 2010.

[109] I.H. Jenkins, M.Jahanshahi, M. Jueptner, R.E. Passingham, and D.J. Brooks. Self-initiated versus externally triggered movements. II. The effect of movement predictability on regional cerebral blood flow. *Brain*, 123:1216 – 1228, 2000.

[110] S.T. Grafton, R.S. Turner, M.Desmurget, R. Bakay, M. Delong, J. Vitek, and M. Crutcher. Normalizing motor-related brain activity: Subthalamic nucleus stimulation in Parkinson disease. *Neurology*, 66:1192 – 1199, 2006.

[111] M. Jenkinson, C.F. Beckmann, T.E. Behrens, M.W. Woolrich, and S.M. Smith. FSL. *NeuroImage*, 62:782 – 790, 2012.

[112] M.W. Woolrich, S. Jbabdi, B. Patenaude, M. Chappell, S. Makni, T. Behrens, C. Beckmann, M. Jenkinson, and S.M. Smith. Bayesian analysis of neuroimaging data in FSL. *NeuroImage*, 45:S173 – 186, 2009.

[113] S.M. Smith, M. Jenkinson, M.W. Woolrich, C.F. Beckmann, T.E.J. Behrens, H. Johansen-Berg, P.R. Bannister, M. De Luca, I. Drobnjak, D.E. Flitney, R. Niazy, J. Saunders, J. Vickers, Y. Zhang, N. De Stefano, J.M. Brady, and P.M. Matthews. Advances in functional and structural MR image analysis and implementation as FSL. *NeuroImage*, 23(S1):208 – 219, 2004.

[114] FMRIB. Fsl, fmrib software library v5.0, 2012.

[115] T. E. Lund, K. H. Madsen, K. Sidaros, W.-L. Luo, and T. E. Nichols. Non-white noise in fMRI: Does modelling have an impact? *NeuroImage*, 29:54 – 66, 2006.

[116] F. Esposito, A. Tessitore, A. Giordano, R. De Micco, A. Paccone, R. Conforti, G. Pignataro, L. Annunziato, and G. Tedeschi. Rhythm-specific modulation of the sensorimotor network in drug-naive patients with Parkinson's disease by levodopa. *Brain*, 136:710 – 725, 2013.

[117] D. Mantini, M.G. Perrucci, C. Del Gratta, G.L. Romani, and M. Corbetta. Electrophysiological signatures of resting state networks in the human brain. *Proceedings of the National Academy of Science*, 104(32):13170–13175, 2007.

[118] M. D. Greicius, B. Krasnow, A. L. Reiss, and V. Menon. Functional connectivity in the resting brain: A network analysis of the default mode hypothesis. *Proceedings of the National Academy of Sciences*, 100(1):253 – 258, 2003.

[119] A. Tessitore, F. Esposito, C. Vitale, G. Santangelo, M. Amboni, A. Russo, D. Corbo, G. Cirillo, P. Barone, and G. Tedeschi. Default-mode network connectivity in cognitively unimpaired patients with Parkinson disease. *Neurology*, 79(23):2226 – 2232, 2013.

[120] L. Krajcovicova, M. Mikl, R. Marecek, and Irena Rektorova. The default mode network integrity in patients with Parkinson's disease is levodopa equivalent dose-dependent. *Journal of Neural Transmission*, 119:443 – 454, 2012.

[121] A. Tessitore, M. Amboni, F. Esposito, A. Russo, M. Picillo, L. Marcuccio, M. T. Pellecchia, C. Vitale, M. Cirillo, and G. Tedeschi P. Barone. Resting-state brain connectivity in patients with Parkinson's disease and freezing of gait . *Parkinsonism and Related Disorders*, 18:781 – 787, 2012.

[122] J. Rowe, K.E. Stephan, K.Friston, R. Frackowiak, A. Lees, and R. Passingham. Attention to action in Parkinson's disease. Imapired effective connectivity among frontal cortical regions. *Brain*, 125:276 – 289, 2002.

[123] T. van Eimeren, O. Monchi, B. Ballanger, and A. P. Strafella. Dysfunction of the Default Mode Network in Parkinson Disease . *Archives of Neurology*, 66(7):877 – 883, 2009.

[124] C.D. Hacker, J.S. Perlmutter, S.R. Criswell, B.M. Ances, and A.Z. Snyder. Resting state functional connectivity of the striatum in Parkinson's disease. *Brain*, 135:3699 – 3711, 2012.

[125] R. C. Helmich, M. J. R. Janssen, W. J. G. Oyen, B. R. Bloem, and I. Toni. Pallidal Dysfunction Drives a Cerebellothalamic Circuit into Parkinson Tremor . *Annals of Neurology*, 69:269 – 281, 2011.

[126] J. M. Shine, G. M. Halliday, M. Gilat, E. Matar, S.J. Bolitho, M. Carlos, S. L. Naismith, and S.J.G. Lewis. The Role of Dysfunctional Attentional Control Networks in Visual Misperceptions in Parkinson's Disease . *Human Brain Mapping*, 00:00, 2013. Epub ahead of print.

[127] V. Litvak, , A. Jha, A. Eusebio, R. Oostenveld, T. Foltynie, P. Limousin, L. Zrinzo, M. I. Hariz, K. Friston, and P. Brown. Resting oscillatory cortico-subthalamic connectivity in patients with Parkinson's disease . *Brain*, 134:359 – 374, 2011.

Acknowledgements

Thanks to my supervisor, Dott.ssa Claudia Testa, for engaging me in neuroimaging with enthusiasm and for following me with attention and great willingness;
thanks to Prof. Raffaele Lodi and Prof.ssa Caterina Tonon, for accepting me to work in the U.O. RM funzionale, DIBINEM, and for helping me with the revision;
thanks to Prof.ssa Paola Fantazzini, for the advices for this thesis;
thanks to all the other people working in the U.O. RM Funzionale: David Neil Manners, Emil Malucelli, Ludovica Gramegna, Alessandro Agostini, Claudio Bianchini and Stefano Zanigni, as they all made in their own way a contribution to this work;
thanks to Giovanni Rizzo and Francesca Pittau, for the information about Parkinson's disease and the precious collaboration in interpreting the results;
thanks to Lorenzo Ferri, for the information about EEG analysis and for providing me the ECG data I needed.

Thanks to my main supporters, and unique sponsor of these 5 years at university;
thanks to my favourite newly-weds;
thanks to the good friend that Master's degree gave me;
thanks to dear old physicist friends;
thanks to the friend of down-town picnic dinners, strolls and long thusan chats;
thanks to the friend of frenzies and phone calls (when we manage to arrange, and although we live five minutes away from each other);
thanks to the friend that worries about not being able to help me as much as I helped him because, according to him, I solve everything on my own;
thanks to the last person that entered my private life, thanks for your instinctive rationality, for your silences and your gazes, and for having always been able to charge an uncharged coil.